HYPERSONIC BOUNDARY LAYER FLOW AROUND A SHARP CORNER

Thesis by

Andreas Puhl

In Partial Fulfillment of the Requirements

For the Degree of

Aeronautical Engineer

California Institute of Technology

Pasadena, California

June, 1965

ACKNOWLEDGMENTS

The author feels a deep sense of gratitude to Professor Toshi Kubota who suggested and supervised the present experiment and, through his broad understanding, contributed significantly to the completion of this research. For scientific guidance, personal encouragement and many stimulating discussions arousing and cultivating the author's interest, sincere thanks are especially due to Professor Lester Lees. The author also wishes to express his gratitude to: Mrs. Truus van Harreveld for her invaluable contribution in reducing the data most carefully and conscientiously, Mrs. Virginia Conner for her able and efficient typing and preparing of the manuscript, the staff of the GALCIT hypersonic wind tunnels under Mr. P. Baloga and especially Messrs. S. Roman, J. Van Dijk, G. Van Halewyn and H. Mazurowski for their assistance in conducting the wind tunnel tests, and the staff of the Aeronautics Machine Shop under G. Carlson, especially Messrs. H. McDonald and C. Baetz for their skill in constructing the test equipment.

This investigation was carried out under the sponsorship and with the financial support of the U. S. Army Research Office and the Advanced Research Projects Agency, Contract No. DA-31-124-ARO(D)-33. This research contract is a part of Project DEFENDER sponsored by the Advanced Research Projects Agency.

ABSTRACT

An experimental investigation was conducted in the GALCIT Mach 8 hypersonic wind tunnel, in order to study the behavior of an axisymmetric hypersonic laminar boundary layer flow undergoing a rapid expansion at the juncture of a cone-cylinder body of revolution at zero angle of yaw. Major emphasis was placed on the acquisition of detailed data near the corner where extreme changes in the flow properties were expected. All tests were carried out for two different reservoir pressures but equal total temperature. The basic measurements consist of the model surface pressure and the pitot pressure covering the entire flow field of interest. These informations with certain assumptions were sufficient to construct the flow field.

The surface pressure distribution is in total disagreement with the potential theory from three boundary layer thicknesses upstream of the corner to about fifteen boundary layer thicknesses downstream. The expansion is not concentrated near the corner but extended over the above-mentioned region which is about one and a half cylinder radii long. The pressure immediately downstream of the corner is about seven-tenths of the pressure on the cone, in constrast to the two-tenths as predicted by the potential theory.

TABLE OF CONTENTS

LIST OF FIGURES

LIST OF FIGURES (Cont'd)

LIST OF SYMBOLS

a	sound speed, $\sqrt{\gamma RT}$ (ft./sec.)
a^*	critical sound speed (ft./sec.)
C_p, C_v	specific heat at constant pressure and constant volume, respectively
C	Chapman-Rubesin factor, $\frac{\mu_w/\mu_\infty}{T_w/T_\infty}$
F_1, F_2	functions of K
K	hypersonic similarity parameter, $M_\infty \theta$
k	coefficient of thermal conductivity of gas
L	total wetted length of cone
M	Mach number, V/a
p	pressure
p_t^1	pitot pressure
Pr	Prandtl number of gas, $C_p\mu/k$
R	Gas constant per unit mass
R	radius of cylinder (in.)
Re	Reynolds number per unit length (in.$^{-1}$)
s	distance along cylinder from corner downstream (in.)
$-\bar{s}$	distance along cone from corner upstream (in.)
T	temperature ($^\circ$F relative or $^\circ$R absolute)
V	velocity (ft./sec.)
x	wetted distance along body from apex (in.)
$\bar{y}$	coordinate normal to body surface
γ	ratio of specific heats, C_p/C_v
δ	boundary layer thickness (in.), as defined in Part IV. 4
δ^*	boundary layer displacement thickness (in.)

LIST OF SYMBOLS (Cont'd)

θ	cone semi-vertex angle
μ	ordinary coefficient of viscosity
ν	kinematic viscosity
ρ	mass density
$\bar{\chi}$	hypersonic boundary layer interaction parameter, $\sqrt{C/Re_x}\ M^3$

Subscripts

c	inviscid quantity at cone surface
e	quantity at the boundary layer edge
s	quantity at the surface
t	quantity at reservoir conditions
x	referred to wetted length from apex
$\bar{y}$)	quantity at surface with probe position $\bar{y}$
δ	quantity at the boundary layer edge, as defined in Part IV. 4
1	quantity ahead of normal shock of probe
∞	quantity in the undisturbed flow

I. INTRODUCTION

For smooth bodies in slightly viscous flows the theory of boundary layer is well established. The basic assumption in the theory is that the streamwise variations in the flow are small compared to the transverse gradients in the boundary layer. This assumption breaks down near a sharp leading edge, the trailing edge of a thin plate and a sharp corner. Many practical shapes have a sharp corner such as the junction of a cone-cylinder, the ridge on a double-wedge airfoil, and the corner at the bluff base of a finite cone or wedge.

It has been observed at subsonic and low supersonic speeds that the presence of a sharp corner is felt a few boundary layer thicknesses upstream in the layer and often the flow separates and reattaches downstream of the corner. Not many extensive investigations have been carried out on this problem either experimentally or theoretically because of the difficulties involved and partly because of a limited extent of the corner influence in those speed ranges. At hypersonic speeds, however, the boundary layers are much thicker compared to those at low speeds. Also the effects of the boundary layer on the external flow are more pronounced, and often these must be taken into account in determining the flow in the boundary layer itself. Thus the corner problem can no longer be ignored, and the present investigation is aimed toward obtaining experimental data on the interaction of hypersonic laminar boundary layer with an expansion caused by a surface slope discontinuity.

---

* Numbers in parentheses denote references at the end of the text.

Only a limited number of experiments has been carried out on this problem in the past. Murthy and Hammit[1] investigated experimentally the interaction of a turbulent boundary layer with Prandtl-Meyer expansion at M = 1.88. They found that the pressure downstream of the corner was initially appreciably higher than the simple wave theory predicted but gradually approached the Prandtl-Meyer value about five boundary layer thicknesses downstream. They carried out a characteristic calculation for a rotational flow, neglecting the subsonic portion of the initial profile in the boundary layer, which agreed qualitatively with the pressure measurements. Sternberg [2] at BRL and later Zakkay, Tani, Toba and Kuo[3, 4] at PIBAL studied the flow around a sharp convex corner using a cone-cylinder at supersonic speeds. They were interested mainly in the surface temperatures and heat transfers, and only a very limited amount of fluid dynamical data was obtained. Apparently in these experiments the boundary layers were so thin that the surface pressures downstream of the corner were in fairly close agreement with the potential theory predictions.

Zakkay[5] proposed a flow model attributed to Antonio Ferri, in which the flow over the corner within a distance on the order of the boundary-layer thickness is divided into three parts; an inviscid supersonic layer, an inviscid sublayer and a viscous sublayer adjacent to the wall. The flow in the supersonic layer may be analyzed by the characteristic method, and the inviscid sublayer is treated as a one-dimensional flow with the assumption that the pressure is

constant across the layer. The viscous sublayer is analyzed by usual boundary layer techniques, which is carried out in Ref. 3 using a series expansion technique suggested by Goldstein[6] and Görtler.* Zakkay et al did not carry out the inviscid analyses. In a recent paper by Weinbaum[7] the inviscid rotational supersonic flow was analyzed, and it was pointed out that the boundary layer in a region of large wall curvature can cause large departure from the Prandtl-Meyer theory at hypersonic Mach numbers.

In order to fill the void of experimental data, the present investigation was undertaken to measure the surface pressure distributions and the pitot pressure distributions in the boundary layer on a cone-cylinder at Mach number 8. From these measurements the flow field near the corner was constructed to provide a basis for further theoretical research on this subject and to augment the understanding of the phenomena which have eluded theoretical description.

* See, for example, Schlichting: Boundary Layer Theory, pp. 158-159.

II. EXPERIMENTAL APPARATUS AND PROCEDURES

II. 1. Wind Tunnel

The experiment was conducted in the GALCIT $7\frac{1}{4}'' \times 7\frac{1}{4}''$ Hypersonic Wind Tunnel, Leg No. 2, at a nominal Mach number of 8. The tunnel is of a continuously operating closed-circuit type, with air as the working medium. It is installed with a symmetrical, flexible-plate nozzle which was contoured to yield uniform flow conditions in the test section. In order to avoid liquefaction, the air was heated to 900°F by means of a nichrome-wire heater enclosed in the supply section upstream of the nozzle.

The reservoir pressure was measured with a Tate-Energy nitrogen-balanced gage and could be controlled within ±0.05 psi. The reservoir temperature was measured by means of a thermocouple located between heater and nozzle and recorded with an accuracy of 0.3%.

The free-stream impact pressure was recorded with an uncertainty of ±0.03 psi, so that an accuracy of the Mach number of ±0.01 resulted.

All tests were carried out under steady-state conditions. Since the tunnel was of the closed-circuit continuously operating type, sufficient time was available to establish thermal and dynamical equilibrium. No heating or cooling of the model was considered, so that the data presented in this report are for the adiabatic or no-heat transfer case.

The model was kept at zero angle of incidence. Tests were conducted under the following two flow conditions:

A., $M_\infty = 7.87$

$p_{t\infty} = 264.3$ p. s. i. a.

$T_{t\infty} = 900°F.$

$Re_{L\infty} = .49 \times 10^6$

B., $M_\infty = 7.81$

$p_{t\infty} = 132.3$ p. s. i. a.

$T_{t\infty} = 900°F.$

$Re_{L\infty} = .257 \times 10^{-6}$

The test section flow was considered uniform over a length of the longitudinal body dimension.

II. 2. Model

The model is a 10° semi-angle circular cone with a cylindrical afterbody, providing a 10° turning angle around the shoulder. The dimensions of the stainless steel model used in the present tests are given in Figure 3. The frontal area of the cone-cylinder configuration was limited to a size that would allow the tunnel flow to start.

An optical comparator examination of the cone showed that the desired angle of 10° was within the tolerances shown. The diameter of the apex was measured and found to be sufficiently small ($Re_{\infty d}$ = 100 and 50, respectively) not to invalidate the theoretical assumption of a pointed body.

On the model 17 pressure orifices with a diameter of 0.01 in. were located as shown in Figure 3. For the purpose of aligning the model to the free stream flow, four additional orifices with a diameter of 0.02 in. were installed at 90° intervals around the circumference. The positions of the surface pressure orifices with respect to the corner were checked both microscopically and mechanically and found to be accurate within ±0.001 in. To eliminate mutual interference and also for ease of construction, the orifices in the shoulder region had to be distributed in a spiral form around the body.

II.3. Pressure Measurements

In order to assure accurate positioning of the probe with respect to the model, after the proper reservoir temperature and reservoir pressure of the tunnel was reached, sufficient time was allowed (ca. 10 minutes) to permit the instruments in the test section to come to thermal equilibrium.

The four static pressure orifices drilled symmetrically at a radial cross section of the cone ($x/L = 0.68$) are provided for the alignment purpose. To account for small flow angle changes mainly due to a slight dependence of the test section flow on the tunnel stagnation conditions, the model supports were adjusted until the pressures at the diametrical locations were equalized.

The model surface pressures were measured by means of a bank of Silicone-oil U-tube manometers, with the reference pressure maintained at 5 to 10 microns-Hg. The surface pressures were recorded in almost every run, and several times the accuracy of the

pressure readings was checked by using a Silicone-oil micromanometer.

The pitot pressure measurements were obtained by using a flattened pitot probe. The outer dimensions of its forward face were 0.04 by 0.004 inches, thus having an aspect ratio of 10. The frontal height corresponded to about 4% of the average boundary layer thickness. The probe orifice dimensions were 0.0286 by 0.002 inches, which limited the traverse speed to 1/6 inch per hour in the boundary layer. To provide stiffness the probe was reinforced with a thin plate with a sharp leading edge and attached to a holder of $\frac{1}{4}$ in. outer diameter. (The drive mechanism of the pitot probe is presented in Figure 2.)

By means of a drive mechanism mounted at the top of the tunnel, the pitot probe was traversed through the flow field perpendicular to the surface of the body. Downstream of the shoulder the attitude of the total head probe with respect to the local streamline direction has been maintained at an estimated mean value of the local streamline tangents, to minimize the error caused by the misalignment of the probe and the flow. The probe position was accurate to ±0.002 in.

The pitot pressure was converted into an electric signal by means of a pressure transducer, amplified and plotted against the probe position on an XY-recorder. Figure 4 shows schematically the recording set-up. The pressure transducer was a Statham PA 208 TC-5-350, which measures absolute pressure up to 5 psi.

The direct current used to excite the pressure transducer was provided by a Video Instruments, Model SR 200 E, D. C. power supply, and its output was adjusted to 5 volts ± 1 millivolt, measured by means of a digital voltmeter, Kintel 501B. The excitation voltage was measured before, during and after every run, and it was found that after the power supply had reached constant operational temperature the voltage was maintained constant during the run.

The static calibration of the transducer against a liquid U-tube manometer yielded a calibration factor of 323. 2 microvolts per volt per cm Hg at room temperature data given by factory: 328. 9 microvolts [open circuit] per volt per cm Hg. Previous tests on the linearity, resolution, and repeatability of the same transducer indicated a satisfactory behaviour over the whole pressure range involved in this experiment. The deviation of the output did not exceed ±0. 15% of the maximum pitot pressure measured for the highest supply pressure used in this experiment. Thereafter the significance of the data was limited by the accuracy of the data plotter.

A Sandborn 1500-860S DC amplifier was used to amplify the transducer signals by the factor of 100 and 50 for reservoir pressures of 118 and 250 p.s.i.g., respectively. A Moseley Model 2 S Autograf XY-Recorder was used to record the amplified pressure signal as a function of normal distance from body surface.

II. 4. Flow Visualization

In order to supplement the pressure measurements, Schlieren photographs were made for two free-stream Reynolds numbers.

Because of the axi-symmetric character of the flow, the Schlieren effect in the field between the shock and the body was understandably weak. As a result of the increased density variation at higher supply pressures the photographs taken at $p_{t\infty}$ = 250 p.s.i.g. and $T_{t\infty}$ = 900°F gave best resolution of the shock wave, the boundary layer edge and the expansion fan. A Schlieren photograph taken under this condition is shown in Figure 21.

III. DATA REDUCTION

III. 1. Pitot Pressure

Near the wall in the boundary layer the pressure measured by the probe is not equal to the total pressure of the streamline aligned with the probe centerline. The difference comes from three principal causes. The first is that the boundary layer flow is distorted by the disturbance of the probe. This is minimized by the use of a small probe, though, to the author's knowledge, no quantitative data are available for this. The second cause is the fact that, when a probe is placed in a shear flow, the stagnation streamline is not aligned with the probe axis because of the unsymmetry, and the effective center of the total pressure is displaced toward the region of higher velocity. The correction given by Young and Maas [8] for an incompressible subsonic fluid is

$$\frac{\delta}{d} = 0.131 + 0.082 \frac{d_1}{d}$$

where δ is the displacement, d_1 and d the internal and external diameters of the probe. This correction was obtained with a circular probe in the wake of an airfoil. On the other hand, the experiments of Davies [9] in laminar boundary layers at supersonic speeds showed the displacement in the opposite sense when the probe diameter is one-half of the boundary layer thickness or larger. However, in the author's opinion, this was probably due to the distortion of the flow caused by the presence of a large probe. In supersonic flow, Johanneson and Mair [10] showed the displacement effect practically vanished in a wake for $M = 1.96$ for probes with the external diameter

twice as large as the wake half-width. The third cause is the low Reynolds number effect.[11, 12, 13] When the probe Reynolds number based on the local flow properties is lower than 200 or so, the total pressure measured by the probe is larger than the total pressure computed by the inviscid flow relation, since the effects of viscosity are no longer negligible.

In the present experiments the displacement effect is expected to be small (the order of .001 inch), judging from the data of references (8) and (10). An attempt was made in the present experiments to correct for the effects of the flow distortion and the viscosity by comparing the velocity profile computed from the pitot pressure data and the theoretical profile on the cone surface away from the shoulder. The comparison was carried out for the two Reynolds numbers of the experiment, and the total pressure correction curve was devised as a function of the distance from the surface normalized by the boundary layer thickness and the Reynolds number, which was used at all other stations. The correction was found to be negligible in the supersonic portion of the boundary layer.

III. 2. Boundary Layer Edge

The boundary layer edge may be determined from the pitot pressure profiles taken on the conical part of the model, since the pitot pressure is nearly constant outside the boundary layer. Similarly, the edge could be defined from the pitot pressure curves for downstream of the shoulder. But around the shoulder the pitot pressure profiles do not show the distinguishable boundary layer edge

since the pitot probe traverses a strong inviscid expansion region after it has emerged from the viscous layer. (The three families of total head traces are shown in Figure 16.) A different method of finding the boundary layer edge is therefore necessary, and the following procedure was used to define the boundary layer edge consistently along the whole range of interest. Assuming constant static pressure across the boundary layer, the local total pressure was computed (Fig. 7). In regions where the boundary layer edge could be defined from the pitot pressure profiles, the total pressure at the edge of the viscous layer was found to be constant within the experimental accuracy. Hence, in the region around the shoulder the boundary layer edge was defined as the point at which the computed total pressure was equal to the total pressure at the edge as determined above. The results were shown in Figures 17 through 19.

III. 3. Velocity and Mach Number Profiles

On the assumption of constant static pressure and total temperature across the boundary layer, the Mach number and the velocity were computed from pitot pressure measurements and the surface pressure readings.

The assumption of constant static pressure cannot be valid in the immediate neighborhood of the corner because of not negligible streamline curvature and accompanying pressure gradients perpendicular to the streamlines of the order of $\rho V^2/r$, where r is the radius of curvature. The pressure gradients may be determined by an iterative procedure. However, this has not been carried out in

the present work, in view of the inaccuracy in experimentally determined streamline shapes.

The first station downstream of the shoulder for which the above assumption has been made was about one-half boundary layer thicknesses away from the corner. Judging from the calculation of the static pressure in the inviscid flow as described in Part III. 4. the transverse pressure gradients may not be negligible near the boundary layer edge, but it is expected that the pressure gradients decay rapidly in the boundary layer because of the fast decrease of velocity and density in the boundary layer. It is thus concluded that the velocity and Mach number profiles of the first two to three stations just downstream of the corner are in error only near the boundary layer edge. At further downstream stations with decreasing streamline curvature, Prandtl's assumption of constant pressure across the boundary layer is believed to be very reasonable.

The velocity profiles were calculated with the assumption of constant stagnation temperature in the entire flow field. Since great difficulties are anticipated in carrying out hot wire measurements under the present test conditions, no experimental determination of the temperature distribution in the boundary layer was attempted.

III. 4. Inviscid Flow

The total head surveys for each station were extended beyond the boundary layer edge across the inviscid region through the shock wave into the free stream.

In portions of the inviscid region, where the flow is unaffected by the expansion fan originating from the shoulder, the pitot pressure

profiles show a gradual decrease in p_t with distance from the model. This total pressure gradient in the transversal direction is attributed to the increasing Mach number in this region associated with the non-uniform nature of the potential flow over a cone.

The static pressure in the inviscid region of the expansion fan was computed using the pitot pressure profiles and an estimated total pressure, which was assumed constant throughout.

The latter approximation requires closer scrutiny with regard to the changes in total pressure caused by a slight curvature of the shock resulting from the boundary layer interaction. But, judging by the straightness of the shock in the region where measurements were carried out, no significant entropy gradients across the inviscid region near the shoulder are expected. The total pressure was obtained from the pitot pressure at the boundary layer edge far downstream and upstream of the corner and from the corresponding surface pressures (assuming constant static pressure across the viscous layer).

IV. RESULTS

IV. 1. Surface Pressure

Near the cone cylinder juncture the spacing of the orifice distribution in axial direction was kept sufficiently small in order to resolve the pressure distribution as accurately as possible. Because of very high gradients at the corner the measured pressures were subject to the error due to the finite diameter of the orifices. The diameter was 0. 01 in., over which distance a pressure may change as much as 0. 2 of p_∞ at the station with the maximum pressure gradient. The scatter at this station was largest but did not exceed 3. 5%. The degree of resolution for the rest of the stations was considered satisfactory. Since it was practically impossible to read the pressure at the corner itself, the fairing of the pressure curve over the region ± 0. 02 inches from the corner is somewhat ambiguous. No pressure measurements were conducted near the vertex of the cone since the present work was mainly concerned with the investigation of the flow in the region of the cone cylinder juncture.

The experimentally found distributions of static pressure along the model surface are shown in Figures 5α through 5γ. For comparison the pressure distributions for inviscid flow and the weak interaction are included.

The inviscid-flow pressure for the conical part of the model was obtained by interpolation of the Kopal tables as presented in Reference 14. Since the axially-symmetric flow around the shoulder of the present body of revolution is locally a two-dimensional Prandtl-Meyer expansion, the conditions just downstream of the cone-cylinder

juncture could be obtained from charts for two-dimensional flow. The surface pressure further downstream of the shoulder could be obtained by the method of characteristics in axially-symmetric flow as given in Procedure IA of Reference 15 (Isenberg) and were smoothly faired to the pressure gradient which was calculated for the conditions just downstream of the cone-cylinder juncture using an approximate procedure outlined in Reference 16 (Hakkinen).

The boundary-layer induced pressure on the cone was computed on the basis of Lees' weak interaction theory, applicable for laminar hypersonic flow on an infinite cone, excluding the strong interaction region near the tip. With the introduction of the hypersonic viscous interaction parameter

$$\bar{\chi} = \sqrt{\frac{C}{Re_x}}\, M^3$$

where

$$C = \frac{\mu_w/\mu_\infty}{T_w/T_\infty} ,$$

the induced pressure is given by the following algebraic relation

$$\frac{p}{p_c} = 1 + F_{1(K)}\, d_\infty\, \bar{\chi}_c + F_{2(K)}\, d_\infty^2\, \chi_c^2$$

The functions $F_{1(K)}$ and $F_{2(K)}$ were taken from Ref. 18. In the present case the hypersonic similarity parameter was K = 1.37. The Chapman-Rubesin factor, C, was calculated using Sutherland's formula and the temperature for an insulated body. For the present case, $C_\infty = 0.75$.

The surface pressures were plotted in two ways: first, the measured pressure over free-stream static pressure as a function of the distances upstream and downstream of the shoulder where the distances were non-dimensionalized using the radius R of the cylinder

and, second, the same pressure ratio versus $(s/L)\sqrt{Re_{L\infty}}$ downstream and $(-\bar{s}/L)\sqrt{Re_{L\infty}}$ upstream of the shoulder, respectively. L is the total wetted length of the cone.

According to potential theory the static pressure along the cone remains constant until the flow expands around the corner resulting in a sudden pressure drop to some minimum value just behind the shoulder. Further downstream it approaches the free-stream static pressure asymptotically. A qualitative comparison of the measured pressure distribution with the inviscid one yields the following significant results:

a. The expansion at the cone-cylinder juncture does have an upstream effect resulting in significant pressure changes within the influence region of 3 to 4 times the local boundary layer thickness. The pressure disturbance propagates upstream in the subsonic part of the boundary layer.

b. The pressure distribution is not discontinuous at the corner from the potential theory and shows an obvious smoothing influence of the viscous layer to the flow around a sharp corner.

c. Downstream of the corner the surface pressure is much higher than the potential theory prediction. The pressure drop at the corner is only one-third of the pressure drop predicted by the Prandtl-Meyer expansion for the inviscid Mach number at the cone surface and the expansion angle at the corner. The pressure, then, approaches gradually the free stream value over a distance of some twenty boundary layer thicknesses.

The following tentative flow model is proposed to explain the above observations. The boundary layer flow undergoes a rapid expansion near the corner. In the main part of the layer the change is so rapid in the streamwise direction that the expansion is isentropic. The viscous effects, however, cannot be neglected everywhere, and near the surface we must assume a viscous sublayer where no slip condition is applied at the wall.

In the inviscid layer, wherein the viscous effects may be neglected, the transverse pressure gradient may not be neglected. Then, in the region near the corner, the major part of the pressure variation is obtained from the expansion of inviscid, non-uniform, rotational flow. The solution of this problem is not an easy task, because the flow is subsonic in some parts and supersonic in other. Some indication of the plausibility of this model is provided from the observation that the surface pressure in the region near the corner agrees fairly well with the characteristic solution for rotational flow in the supersonic region.* Further downstream the computed pressure falls below the measured pressure, indicating that the viscous effect must be taken into account not only in the viscous sublayer but also in the outer layer away from the corner.

Plotting the surface pressure distribution against the distance normalized by $\sqrt{R_e}$ (Fig. 5γ) shows that it scales with the boundary layer thickness.

* The numerical solution based on the characteristic method for rotational flow was kindly furnished by Dr. J. T. Lee at the TRW Space Technology Laboratory. The body contour used in the calculation was the experimentally determined streamline with slightly supersonic initial speed, and so was the initial velocity profile ahead of the corner.

IV. 2. Inviscid Flow Field

It is a well known fact that the supersonic flow past a conical body will have constant physical properties along straight lines eminating from the vertex of the cone. In hypersonic flow, however, not the entire field from the body surface to the shock can be treated as a conical flow, since the strong boundary layer displacement effect forms a new "effective" body shape giving rise to considerable changes of the inviscid region. Because of the strong interaction the shock near the tip is considerably curved and thus the flow ceases to be conical.

It is, nevertheless, believed that most of the streamlines crossing the main portion of the curved part of the shock are contained in the viscous layer by the time they reach the corner.

Figures 17's show the isobars in the inviscid flow region computed from the pitot pressures. The measured pitot pressure distributions were found to define quite distinctly the upstream boundary of the expansion fan. It is straight as far as can be determined experimentally and seen to intersect the boundary layer edge directly above the corner (Fig. 19). In the boundary layer ahead of the corner, if we take the beginning of the expansion at the point where the surface pressure starts decreasing (about two boundary-layer thicknesses ahead of the corner) and trace the Mach waves from this point in the supersonic portion, it also intersects the boundary layer edge directly above the corner, giving some support to the flow model proposed in the previous section.

In Figure 10 static pressure profiles are shown for different stations downstream of the corner. The pressure variation in the inviscid region is represented as a dashed line. The part which is continued into the viscous layer has obviously no validity due to the rapid total pressure change there. On the other hand, the constant pressure approximation in the viscous layer is not quite correct everywhere in the layer. Near the outer edge there will be an appreciable gradient, and the actual pressure distribution may look like the curve labelled "probable distribution." In fact, from the transverse momentum equation in the boundary layer we should expect an appreciable pressure gradient near the outer edge. From the momentum equation

$$\frac{\partial p}{\partial y} = -\rho u \frac{\partial v}{\partial x} - \rho v \frac{\partial v}{\partial y} + (\text{viscous terms})$$

Introducing the following dimensionless variables

$$\bar{x} = x/L, \quad \bar{y} = y/\delta$$

$$\bar{u} = u/u_e, \quad \bar{v} = v/(\delta\, u_e/L)$$

$$\bar{p} = p/p_e, \quad \bar{\rho} = \rho/\rho_e,$$

we obtain

$$\frac{\partial \bar{p}}{\partial \bar{y}} = \gamma M_e^2 \frac{\delta^2}{L^2} \left[-\bar{\rho}\,\bar{u} \frac{\partial \bar{v}}{\partial \bar{y}} + \frac{L}{\delta^2 Re} (\text{viscous terms}) \right].$$

Hence, unless $M_e \delta/L \to 0$, $\partial\bar{p}/\partial\bar{y}$ will not vanish. However, dynamically the pressure gradient is still negligible when $\delta/L \to 0$, since the proper normalization quantity is the dynamic pressure, not the static pressure, when the dynamic effect is considered. The above relation shows also that the pressure gradient decreases rapidly toward the surface because $\bar{v}$ approaches zero and the order of magnitude of $\bar{\rho}$ becomes $1/M_e^2$ away from the edge.

IV. 3. Velocity Profiles

In Figures 9a through 9j velocity profiles for several stations are shown both in corrected and uncorrected form. The technique to correct the original data is described in Part III. 1. The velocity was non-dimensionalized by dividing the value at the boundary layer edge defined in Part III. 2.

The fact that self-similar profiles could be expected upstream of the shoulder unaffected by the expansion prompted the normalized plot using the square-root of the free-stream Reynolds number based on the wetted distance of the particular location from the apex of the cone. Figures 9a and 9b, representing stations on the cone, of which the latter one lies just upstream of the expansion influence, show the similarity as predicted by theory.

Even though downstream of the corner $\sqrt{Re_{x\infty}}$ loses its significance as a similarity parameter, the same non-dimensionalization of the velocity profiles as indicated above has been employed for all stations consistently.

The profiles cease to be similar after the flow has undergone the expansion near the corner. The profiles show no resemblance to the ones in the undisturbed region on the cone.

The strong favorable pressure gradient downstream of the corner accelerates the flow near the wall more than the flow away from the wall; namely, the velocity profile becomes fuller. This behavior is consistently more apparent at the lower Reynolds number. No quantitative theoretical comparison can be made because of lack of solutions to the boundary layer equations appropriate to the present flow characteristics.

In Figures 14α and 14β normalized velocity profiles downstream of the corner are plotted versus $\bar{y}/\delta$. This plot displays clearly the trend of the profile variation with the distance from the shoulder. A strong acceleration of the flow in the inner region of the boundary layer persists up to about $s/R = 0.5$. About eight local boundary layer thicknesses downstream of the corner the pressure gradient decayed sufficiently, resulting in a decreased velocity gradient at the wall.

In Figures 15α and 15β three "far" downstream stations being about 1 to 2 boundary layer thicknesses apart from each other show very little change in their character. The profiles almost coincide and may thus be called quasi self-similar. The fact that the flow takes long distances in recovering to the initial Blasius-like profile after it has undergone an interaction with an expansion fan may be attributed to the slow process of diffusion, spreading into the part of the boundary layer of higher Mach number. This tendency of the flow seems to affirm the earlier mentioned flow model containing a strongly viscous sublayer with its origin at the corner.

Through the presentation of the velocity profiles in dimensional form (Figures 13α and 13β), it is intended to display the change of the profiles both near the surface and close to the boundary layer edge for subsequent locations downstream of the cone-cylinder juncture. Strong changes in the character of the curves are - as expected - more pronounced near the shoulder, and become less further downstream, away from the disturbance region. For the last three stations the surface pressure gradient is almost zero.

In Figures 12α and 12β velocity profiles upstream and downstream of the corner are presented in order to bring to light the severe difference in their character. Even for a "far" downstream station the velocity does not recover to the Blasius form. A more pronounced deviation at the same stations is to be expected for lower reservoir pressures since the "relaxation" distance after the expansion will certainly be proportional to some power of the boundary layer thickness.

Using one of the flow conditions of the present test, the Crocco solution of the compressible boundary layer equations for a flat plate was computed for the purpose of comparing with the experimental curves. In Fig. 12α it is shown that the theoretical result compares favorably with the similar profile measured on the cone.

IV. 4. Flow Field in Boundary Layer

An attempt was made to construct from the measurements the complete flow field of the boundary layer near the cone-cylinder juncture, in order to shed some light on theoretical analyses. Figures 19α and 19β show a resulting picture of the longitudinal section of the boundary layer flow field in the region of about one boundary layer thickness upstream and four boundary layer thicknesses downstream of the corner. In this representation, the $\bar{y}$-coordinate has not been stretched in order to avoid the distortion. The plot contains seven streamlines and an equal number of constant Mach lines. The boundary layer edge and the initial expansion wave have been included for the completeness of the picture.

The streamlines were chosen such that at the station $\frac{s}{R} = 0.1397$ they intersect the constant Mach lines. This arrangement has the advantage of indicating strikingly the smallest velocity changes the flow experiences during the corner expansion.

Most of the acceleration process occurs in a range of about one and a half boundary layer thicknesses downstream of the corner. There the streamlines tend to turn by a higher angle than the turning angle of the solid boundary. This behavior is more pronounced for streamlines near the wall. At this time it is not certain whether this is the correct picture of the flow or the error introduced by the inaccuracies in the measurements and data reduction procedures.

Following streamlines it is observed that the velocity keeps increasing to about four boundary layer thicknesses in the subsonic part and to about six boundary layer thicknesses downstream of the shoulder near the edge of the boundary layer. Further downstream no significant velocity change occurs in the outer region indicating a minor importance of the shear forces in this part. Below the $M = 2.5$ line, however, the particles on streamlines gradually decrease their velocity while traveling downstream. This decrease is more pronounced in the region near the wall. Such a behavior is consistent with the idea of viscous sublayer near the wall. Figures 20α and 20β exhibit the changes of total pressure along the streamlines near the corner. The total pressure was non-dimensionalized by the total pressures corresponding to the particular streamlines at the station $-\bar{s}/R = 1.85$. Since the boundary layer thickness plays an important role as a scaling parameter, the value of δ at the corner has

been used to normalize the longitudinal distance along streamlines.

Large changes in total pressure occur along streamlines close to the body surface when passing over the shoulder. The streamline in the subsonic portion suffers a total pressure loss of about 50% of the reference total pressure over a distance of five boundary layer thicknesses. Along the streamlines in the outer part of the boundary layer the total-pressure gradient near the shoulder is not larger than in any other region.

Figure 18 shows the flow field further downstream and demonstrates the rapid growth of the boundary layer in the region extending from the corner to three boundary layer thicknesses downstream.

It seems noteworthy that near the corner the subsonic layer amounts to 25% and 20% of the corresponding boundary layer thickness for the free-stream Reynolds numbers 0.1042×10^{6} in^{-1} and 0.05314×10^{-6} in^{-1}, respectively, indicating that the subsonic portion is by no means negligible at least for the insulated wall.

V. CONCLUSIONS

From the results obtained in the present study the following conclusions may be drawn regarding the hypersonic boundary layer around a sharp expansion corner:

1. The surface pressure distribution bears no resemblance to the inviscid pressure distribution predicted by simple wave theory. Its behavior can be partially explained by the mechanism of isentropic expansion of the rotational flow in the boundary layer.

2. The Prandtl-Meyer expansion fan in the external flow is not centered at the corner. At the boundary layer edge it is spread over several boundary layer thicknesses.

3. A rapid thickening of the viscous layer is observed about one boundary layer thickness downstream of the shoulder.

4. The velocity gradient near the body surface downstream of the corner becomes large, indicating a layer of increased shear near the surface. Recovery to Blasius profiles downstream of the shoulder requires a distance of many boundary layer thicknesses.

In the present investigation a few assumptions were made in the data reduction some of which are in contradiction with the experimental observations. In order to obtain more reliable results, the following refinements are recommended:

1. A systematic study be made on the disturbance caused by the pitot probe and the necessary corrections for the pitot pressure readings in the boundary layer near the solid wall.

2. The temperature distributions be measured in the boundary layer.

3. A variation of the static pressure be included in the data reduction especially near the corner. It is an almost impossible task to measure directly the pressure distribution in the layer, and perhaps an iterative technique can be used for estimating the static pressure gradients.

The present study suggests further investigations on the effects of (1) the variation of the corner expansion angle; (2) surface cooling; (3) rounding-off the corner, and extensions to the two-dimensional flows and the free-expansions such as backward facing steps and bluff bases.

REFERENCES

1. Murthy, K. R. A.: "Investigation of the Interaction of a Turbulent Boundary Layer with Prandtl-Meyer Expansion Fans at M = 1.88," Princeton Univ., Dept. of Aero. Engrg., Report 403, November 1957.

2. Sternberg, J.: "The Transition From a Turbulent to a Laminar Boundary Layer," Ballistic Research Laboratories, Aberdeen Proving Ground, Report No. 906, May 1954.

3. Zakkay, V. and T. Tani: "Theoretical and Experimental Investigation of the Laminar Heat Transfer Downstream of a Sharp Corner," Polytechnic Inst. of Brooklyn, Dept. of Aerospace Engrg. and Appl. Mech., PIBAL Rept. No. 708, October 1961.

4. Zakkay, V., Toba, K. and Kuo, T. J.: "Laminar, Transitional, and Turbulent Heat Transfer after a Sharp Convex Corner," AIAA Jour., Vol. 2, No. 8, pp. 1389-1395, Aug. 1964.

5. Zakkay, V.: "Heat Transfer at a Corner," Jour. of the Aero. Space Sci., Vol. 27, No. 2, pp. 157-158, Feb. 1960.

6. Goldstein, S.: "Concerning Some Solutions of the Boundary Layer Equations in Hydrodynamics," Proceedings of the Cambridge Philosophical Society, Vol. 25, Part I, pp. 1-30, 1930.

7. Weinbaum, S.: "The Rapid Expansion of a Supersonic Shear Flow," Avco-Everett Research Report 204, Jan. 1965.

8. Young, A. D. and Maas, J. N.: "The Behavior of a Pitot Tube in a Transverse Total Pressure Gradient," Aeronautical Research Council, London, Rep. and Mem. No. 1770, 1936.

9. Davies, F. V.: "Some Effects of Pitot Size on the Measurement of Boundary Layers in Supersonic Flow," Royal Aircraft Establishment, Farnborough, Tech. Note No. AERO. 2179, Aug. 1952.

10. Johannsen, N. H. and Mair, W. A.: "Experiments with Large Pitot Tube in a Narrow Supersonic Wake," Jour. of Aeronautical Sciences, Vol. 19, No. 11, pp. 785-787, Nov. 1952.

11. Sherman, F. S.: "New Experiments on Impact-Pressure Interpretation in Supersonic and Subsonic Rarefied Air Stream," NACA TN 2995, 1953.

12. Matthews, M. L.: "An Experimental Investigation of Viscous Effects on Static and Impact Pressure Probes in Hypersonic Flow. GALCIT Hypersonic Research Project Memo No. 44, June 1958.

13. Potter, J. L. and Bailey, B.: "Pressures in the Stagnation Regions of Blunt Bodies in the Viscous-Layer to Merged-Layer Regimes of Rarefied Flow," von Karman Gas dynamics Facility, ARO, Inc., Technical Documentary Report No. AEDC-TDR-63-168, Sept. 1963.

14. Sims, J. L.: "Tables for Supersonic Flow Around Right Circular Cones at Zero Angle of Attack," NASA SP-3004, 1964.

15. Isenberg, J. S.: "The Method of Characteristics in Compressible Flow," Part I. Steady Supersonic Flow. Air Material Command Technical Report No. F-TR-1173A-ND, December 1947.

16. Hakkinen, R. J.: "Further Results on Supersonic Flow Near Convex Corners," Douglas Report SM-35992, March 22, 1960.

17. Hakkinen, R. J.: "Supersonic Flow Two-Dimensional and Axially-Symmetric Convex Corners and Curvature Discontinuities," Douglas Report No. SM-27747, July 15, 1958.

18. Probstein, R. F.: "Interacting Hypersonic Laminar Boundary Layer Flow Over a Cone," Technical Report AF 2798/1, Div. of Engrg., Brown Univ., Providence, R. I., March 1955.

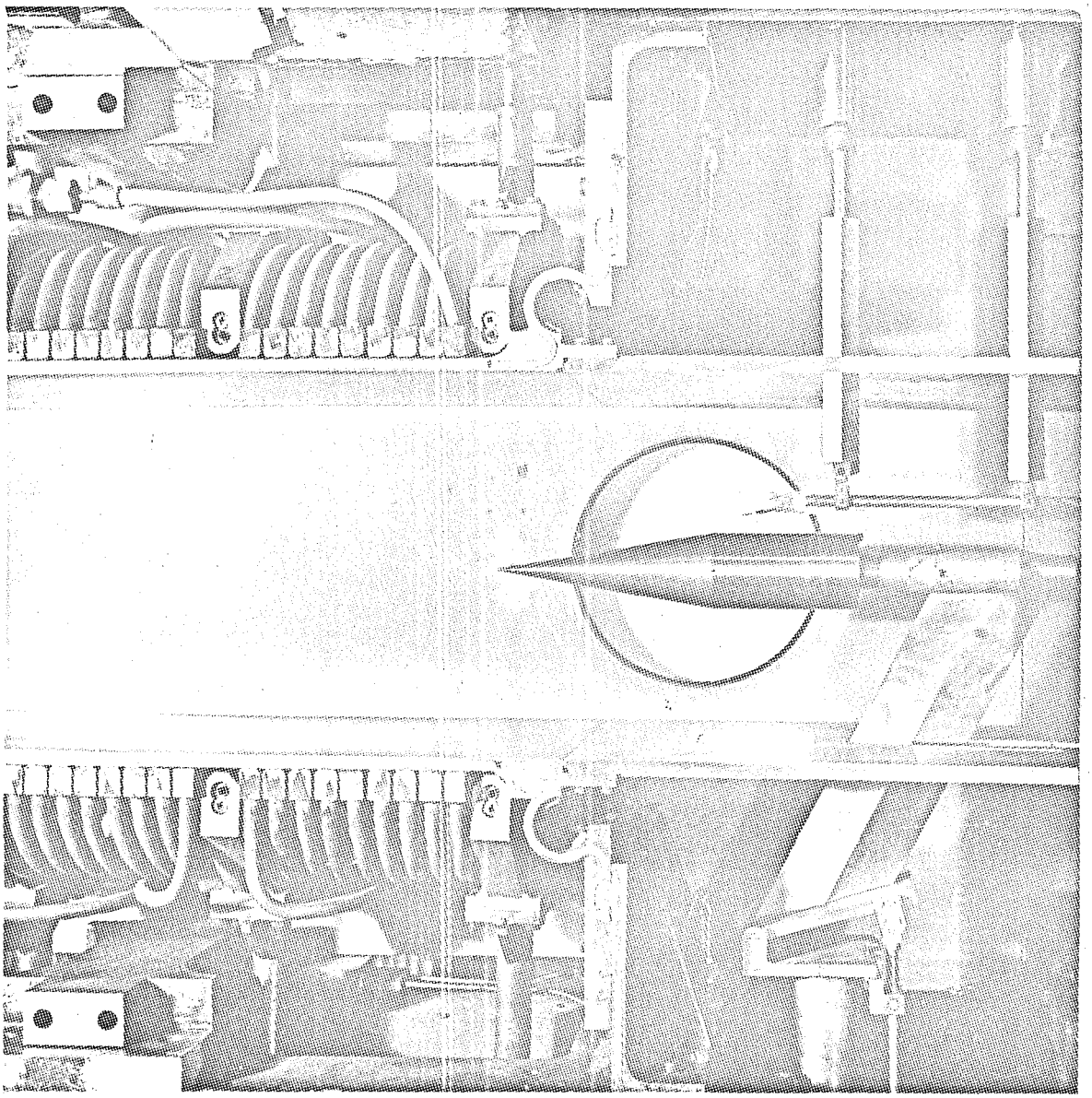

Figure I. Model Installation in Leg2-GALCIT Hypersonic Wind Tunnel

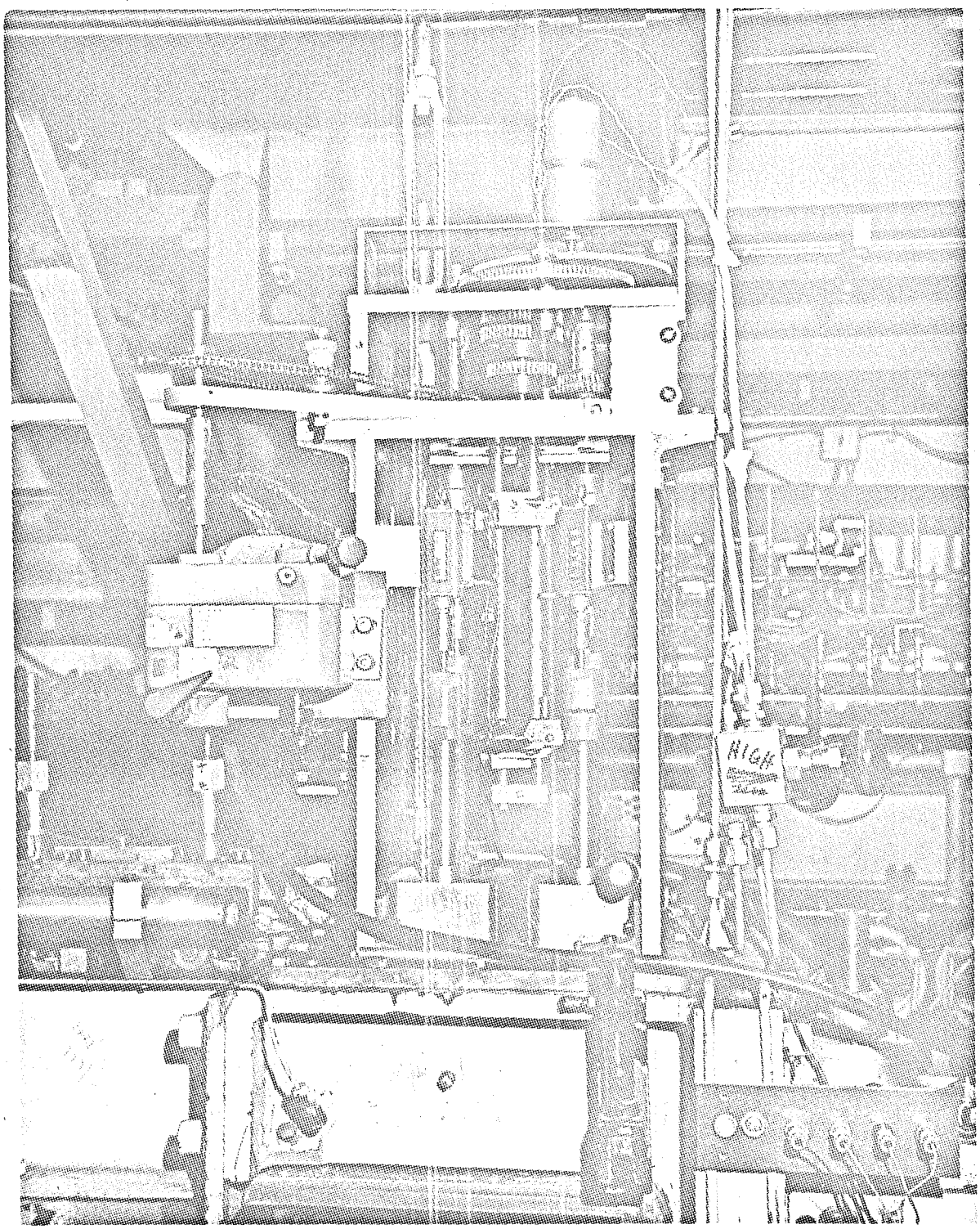

Figure 2. Drive Mechanism for Pitot Probe

	DISTANCE FROM SHOULDER (in.)	β (degrees)
①	+0.02	30
②	+1.40	50
③	−0.32	70
④	−0.02	90
⑤	+0.16	110
⑥	−0.16	130
⑦	+0.04	150
⑧	+1.20	170
⑨	−0.04	190
⑩	+1.00	210
⑪	+0.32	230
⑫	−0.08	250
⑬	+0.80	270
⑭	+0.65	290
⑮	+0.08	310
⑯	+0.50	330
⑰	+2.48	180
㉑	−1.50	0
㉒	−1.50	180
㉓	−1.50	270
㉔	−1.50	90

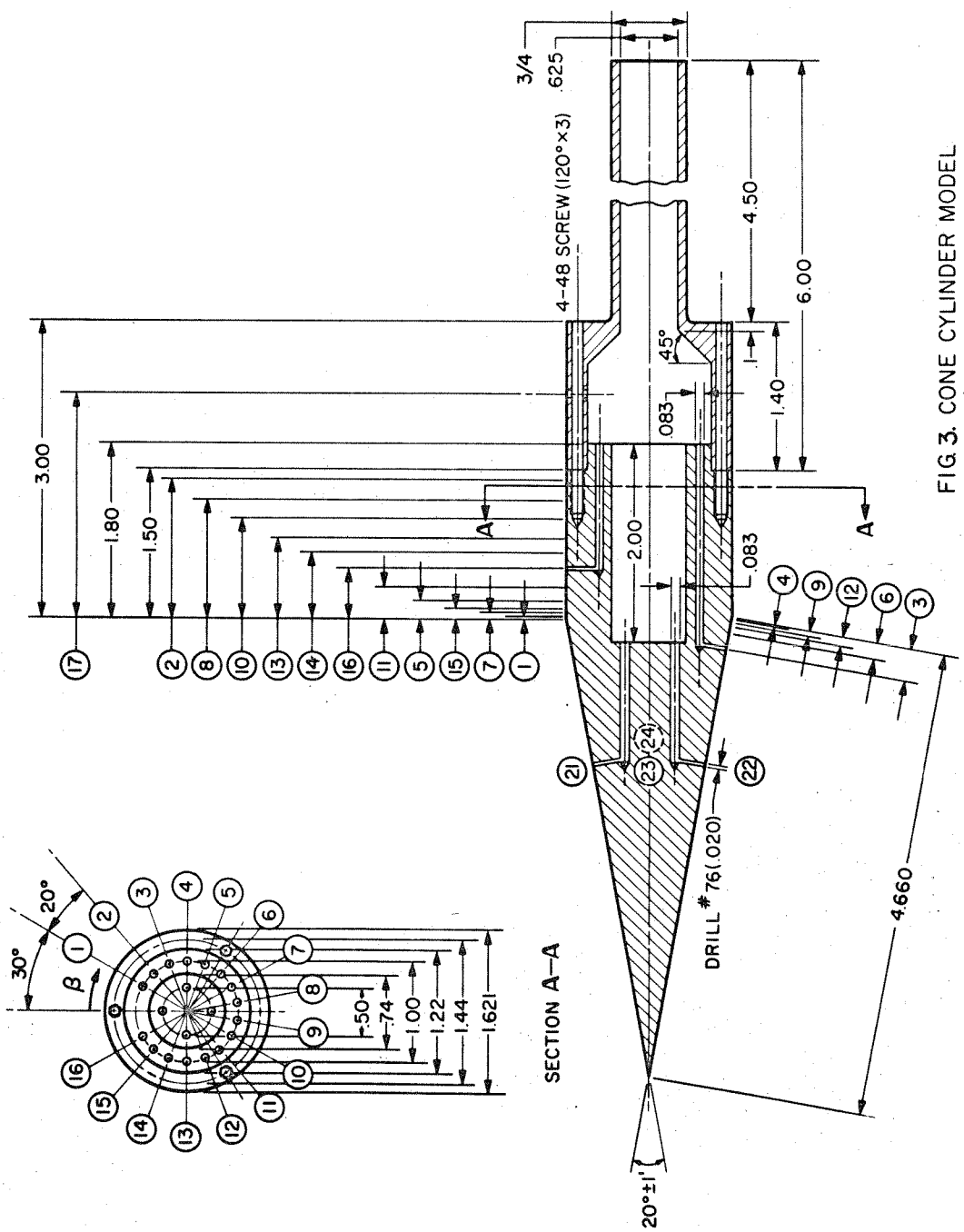

FIG. 3. CONE CYLINDER MODEL

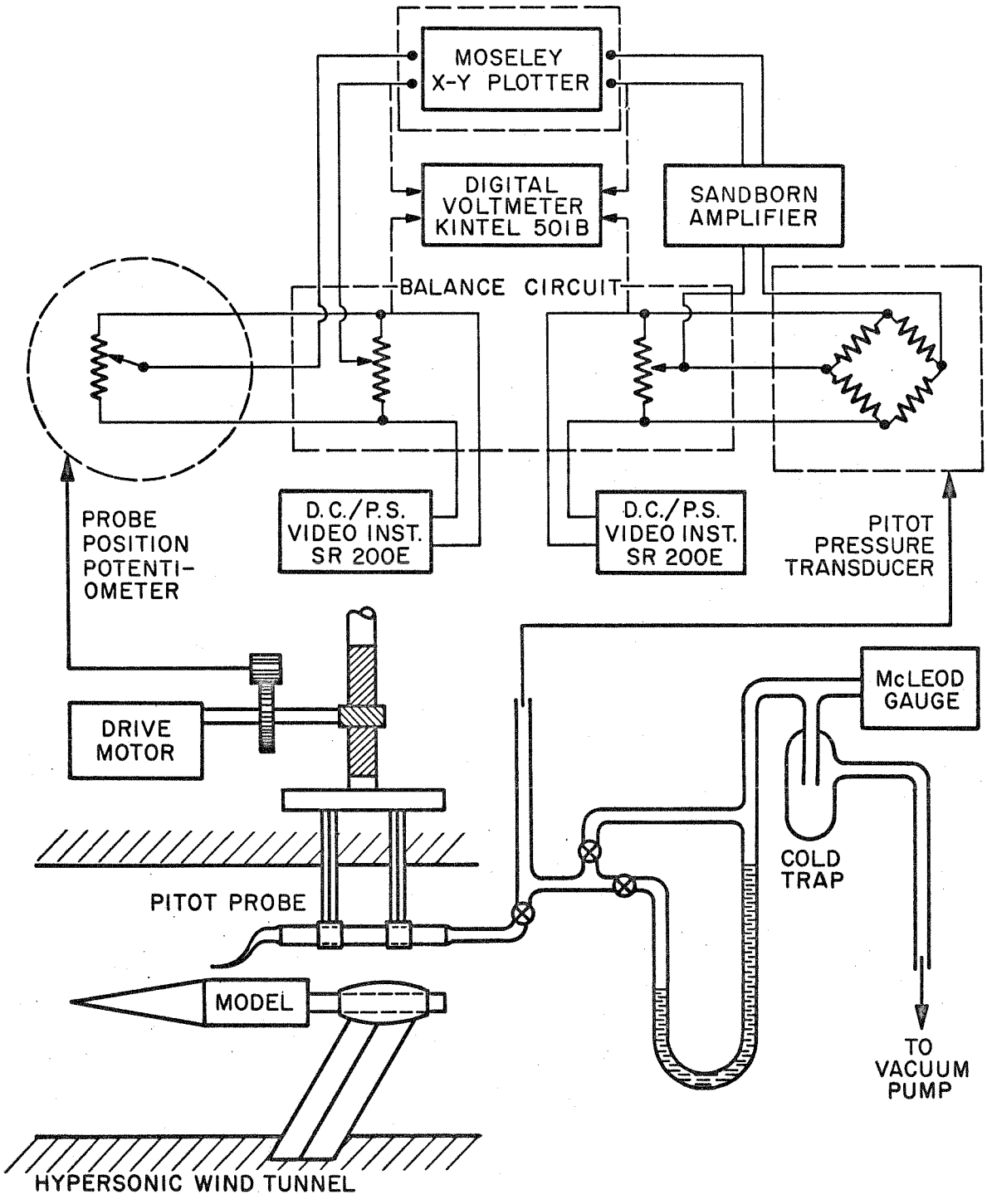

FIG. 4. SCHEMATIC DIAGRAM OF THE TEST SETUP

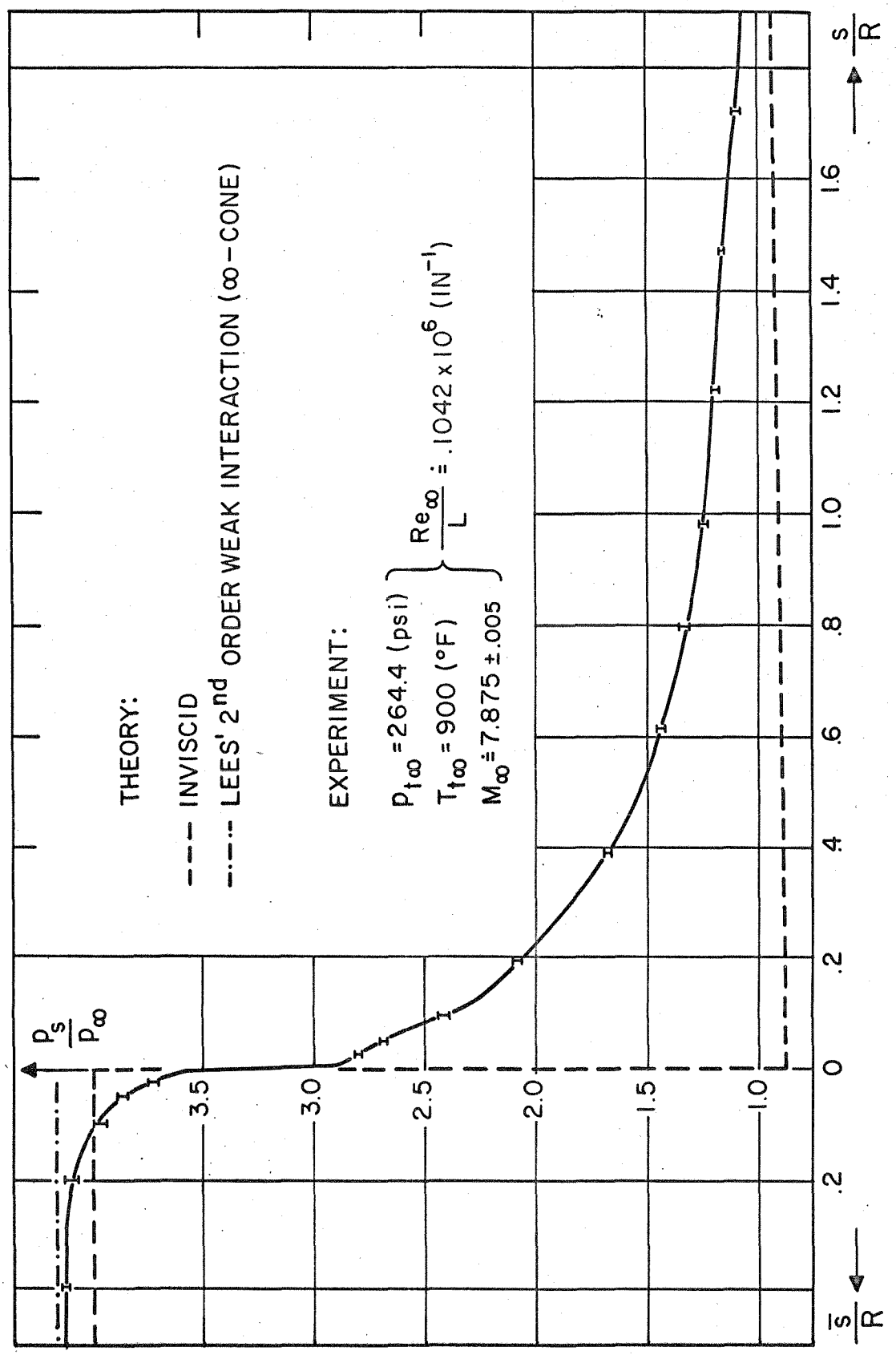

FIG. 5a. SURFACE PRESSURE DISTRIBUTION

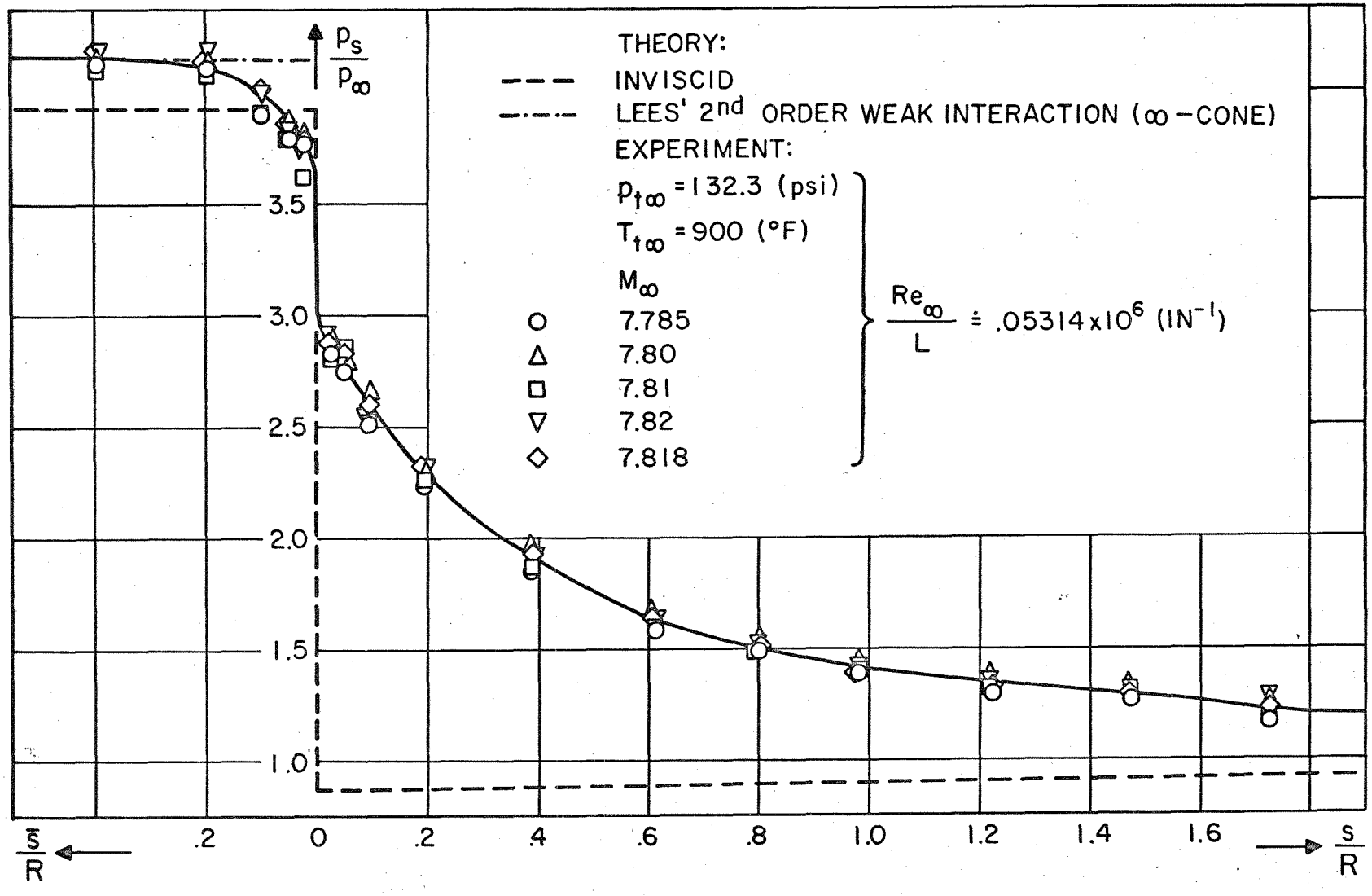

FIG. 5β. SURFACE PRESSURE DISTRIBUTION

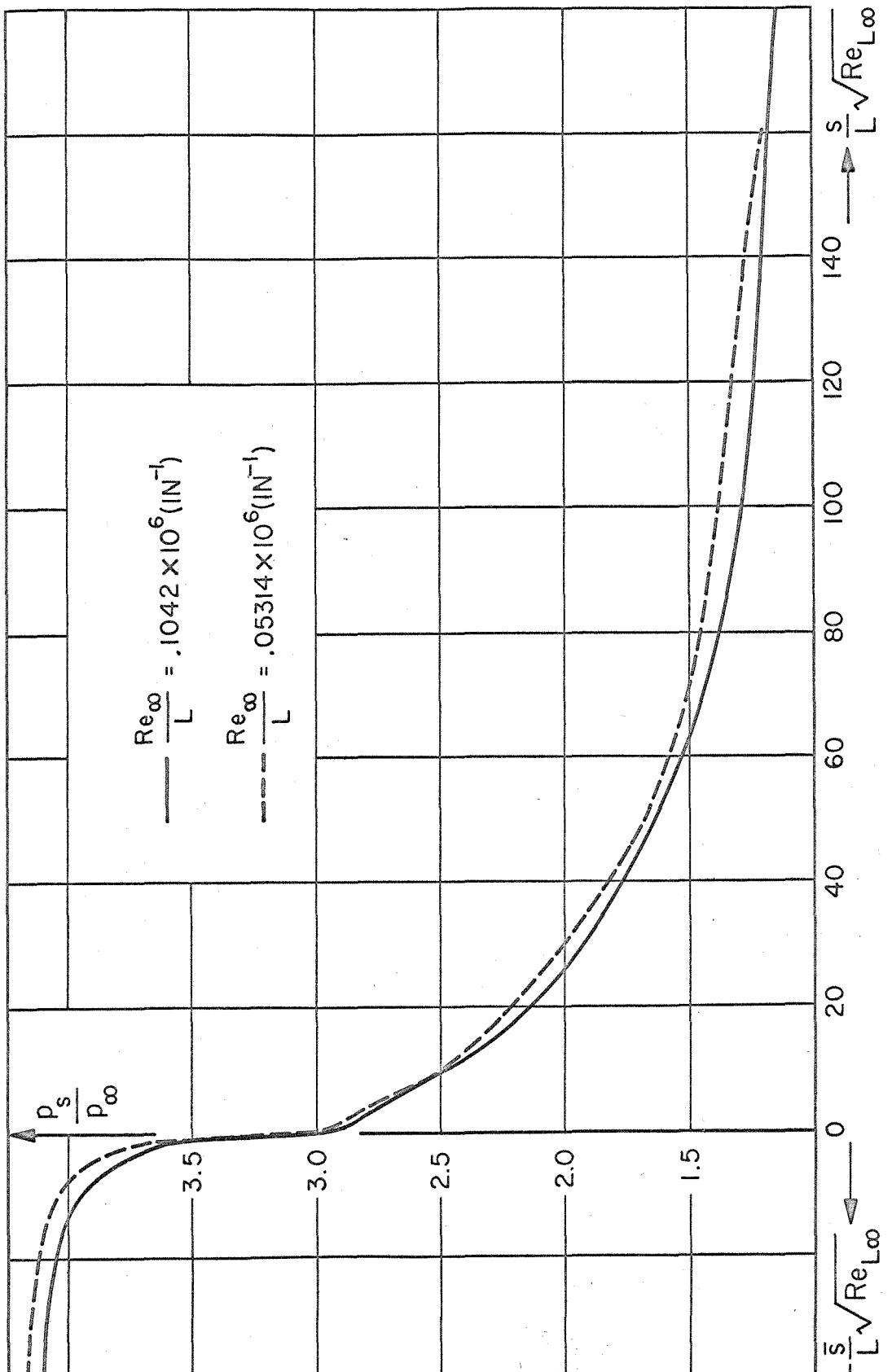

FIG. 5γ SURFACE PRESSURE DISTRIBUTION

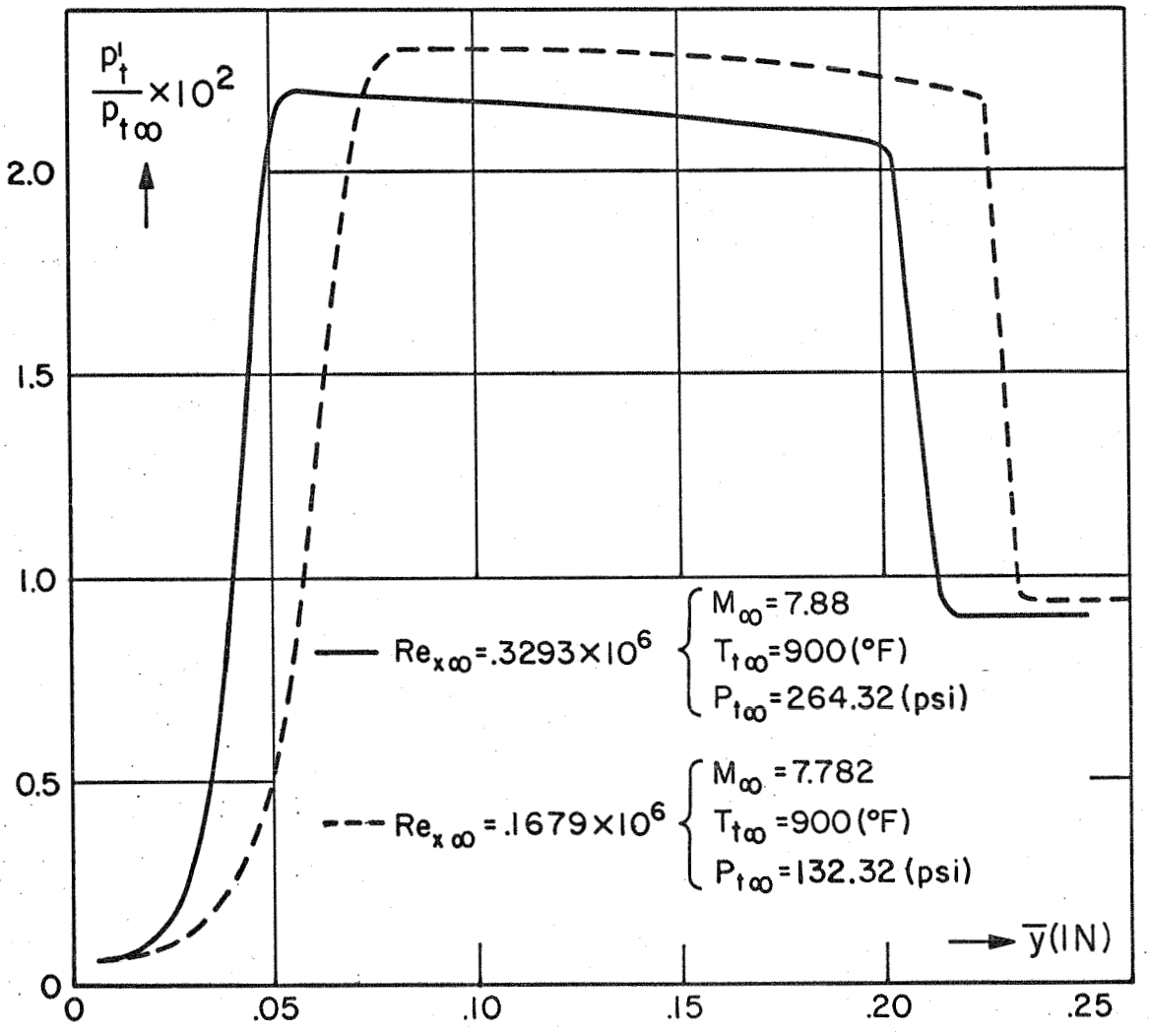

FIG. 6a. IMPACT PRESSURE PROFILES AT - $\overline{s}$ = 1.5 IN.

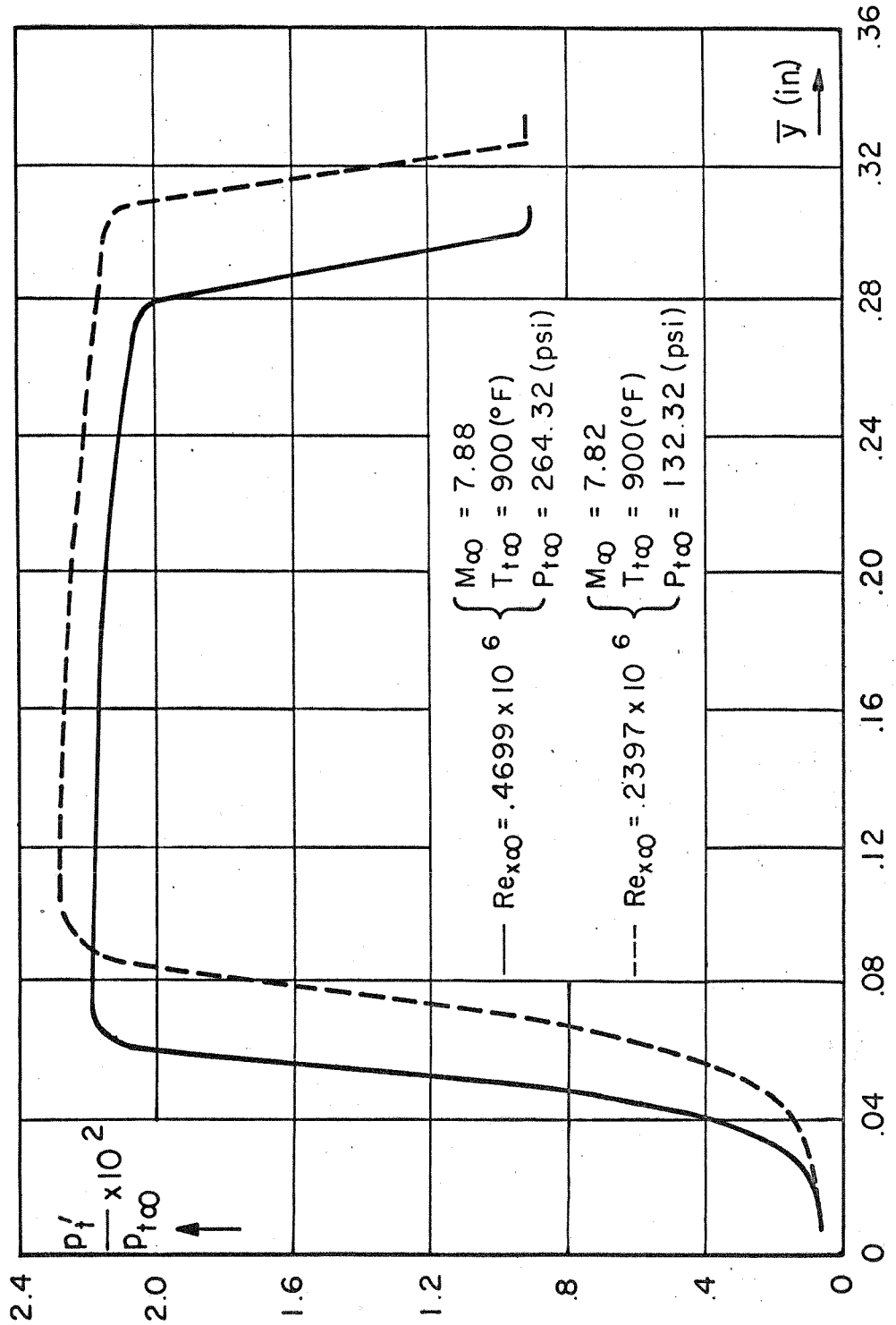

FIG. 6b. IMPACT PRESSURE PROFILES AT - $\bar{s}$ = .15 IN.

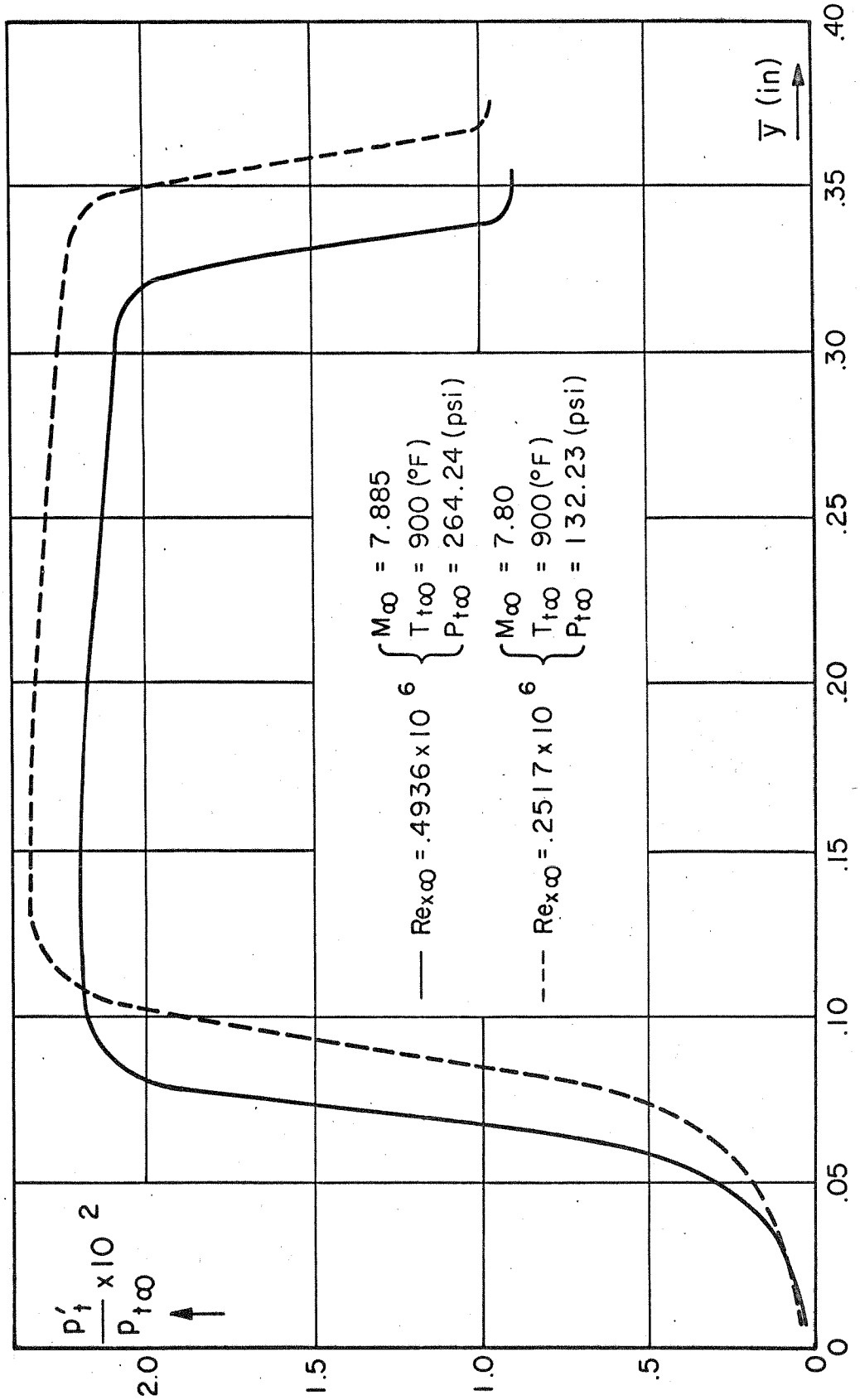

FIG. 6c. IMPACT PRESSURE PROFILES AT s = .0766 IN.

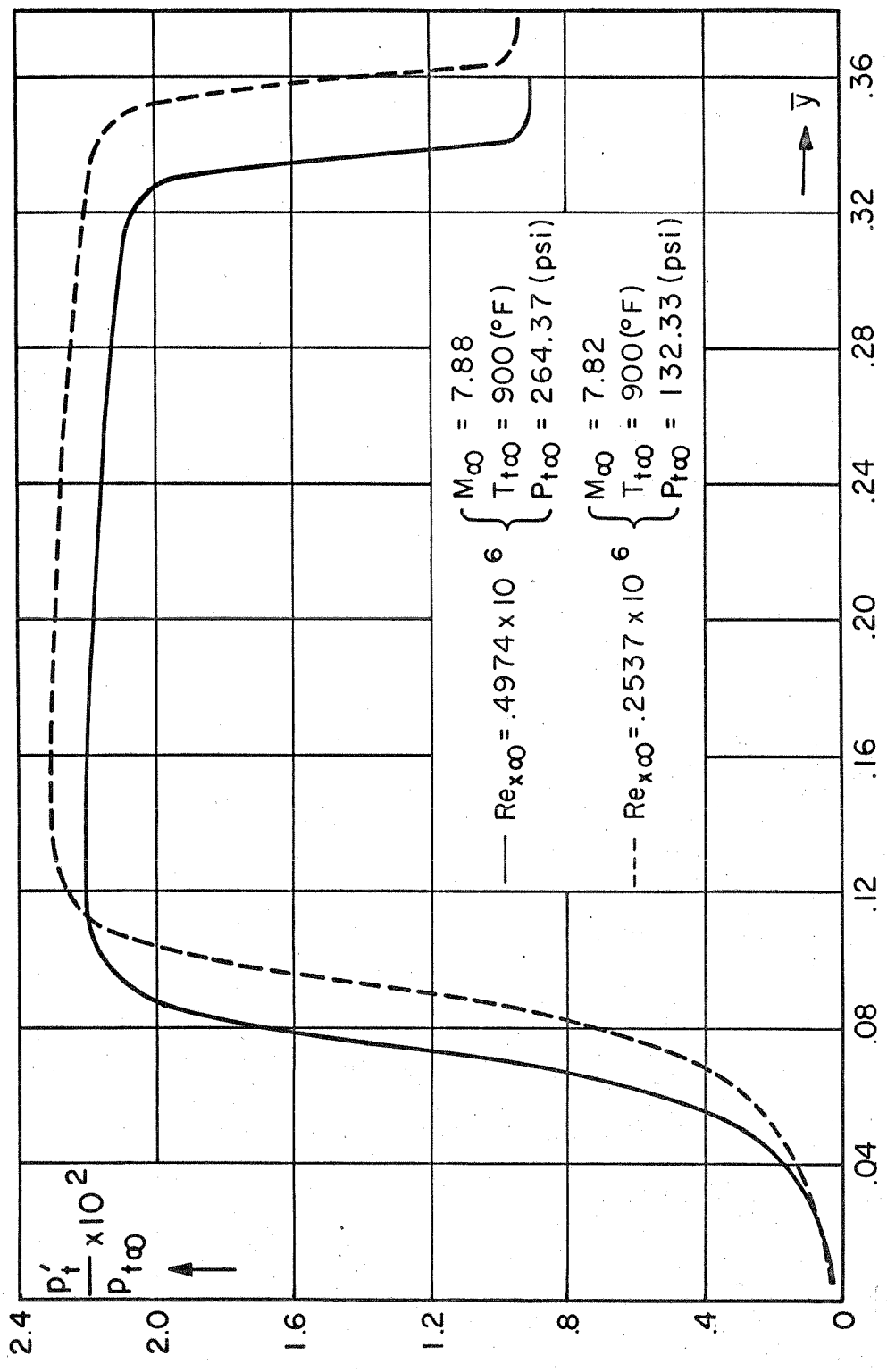

FIG. 6d. IMPACT PRESSURE PROFILES AT s = .1132 IN.

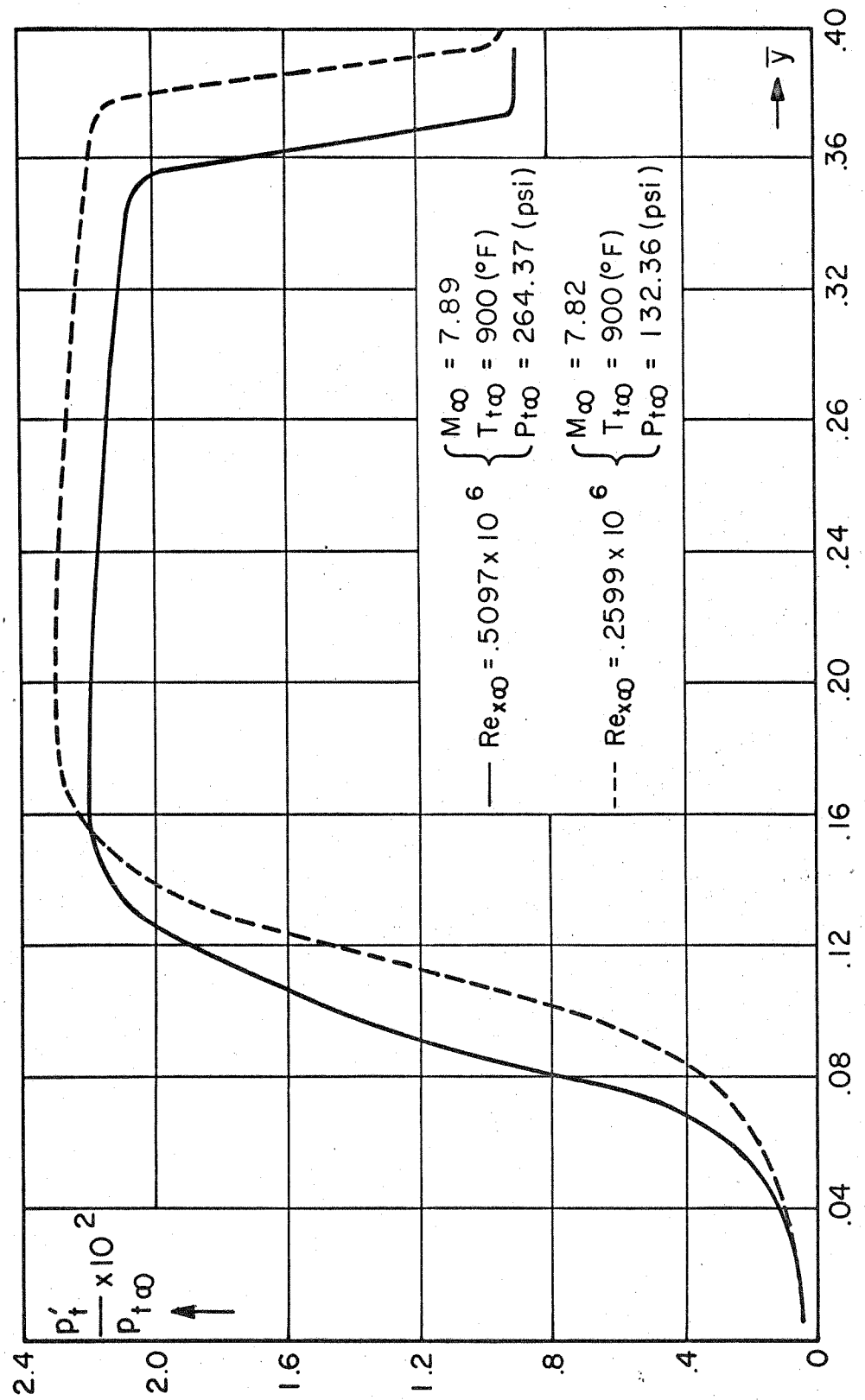

FIG. 6e. IMPACT PRESSURE PROFILES AT s = .2317 IN.

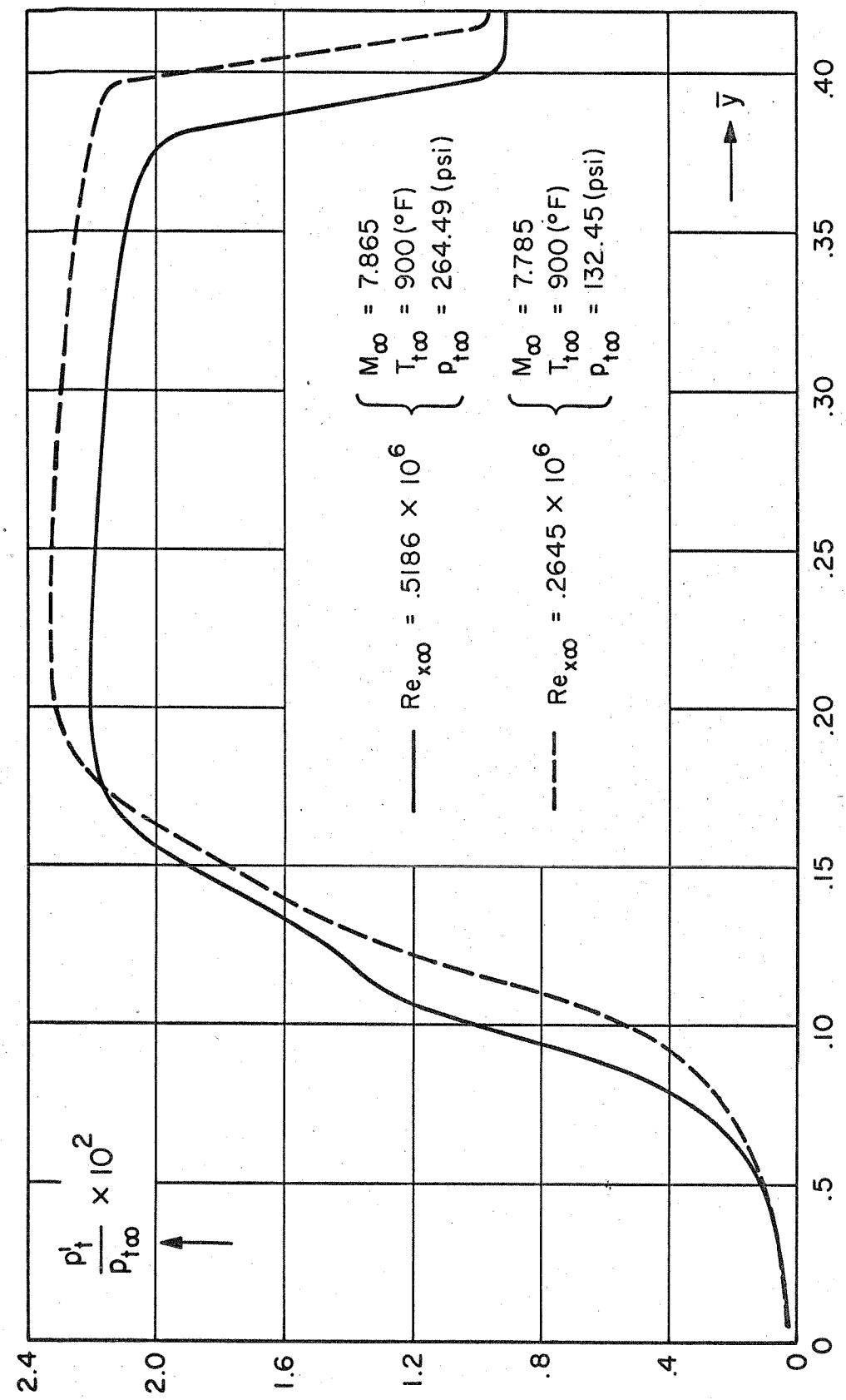

FIG. 6f. IMPACT PRESSURE PROFILES AT s = .317 IN.

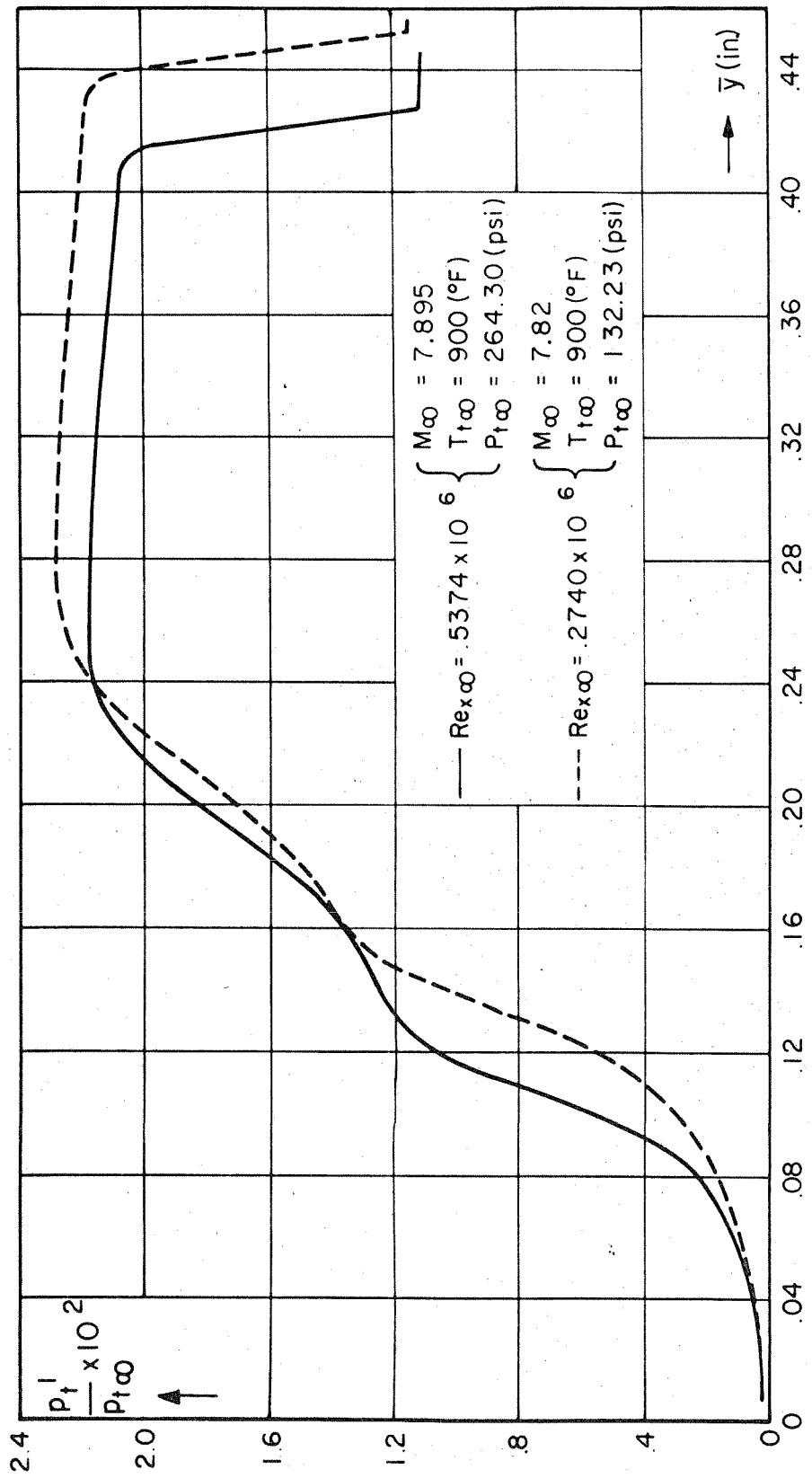

FIG. 6g. IMPACT PRESSURE PROFILES AT s = .497 IN.

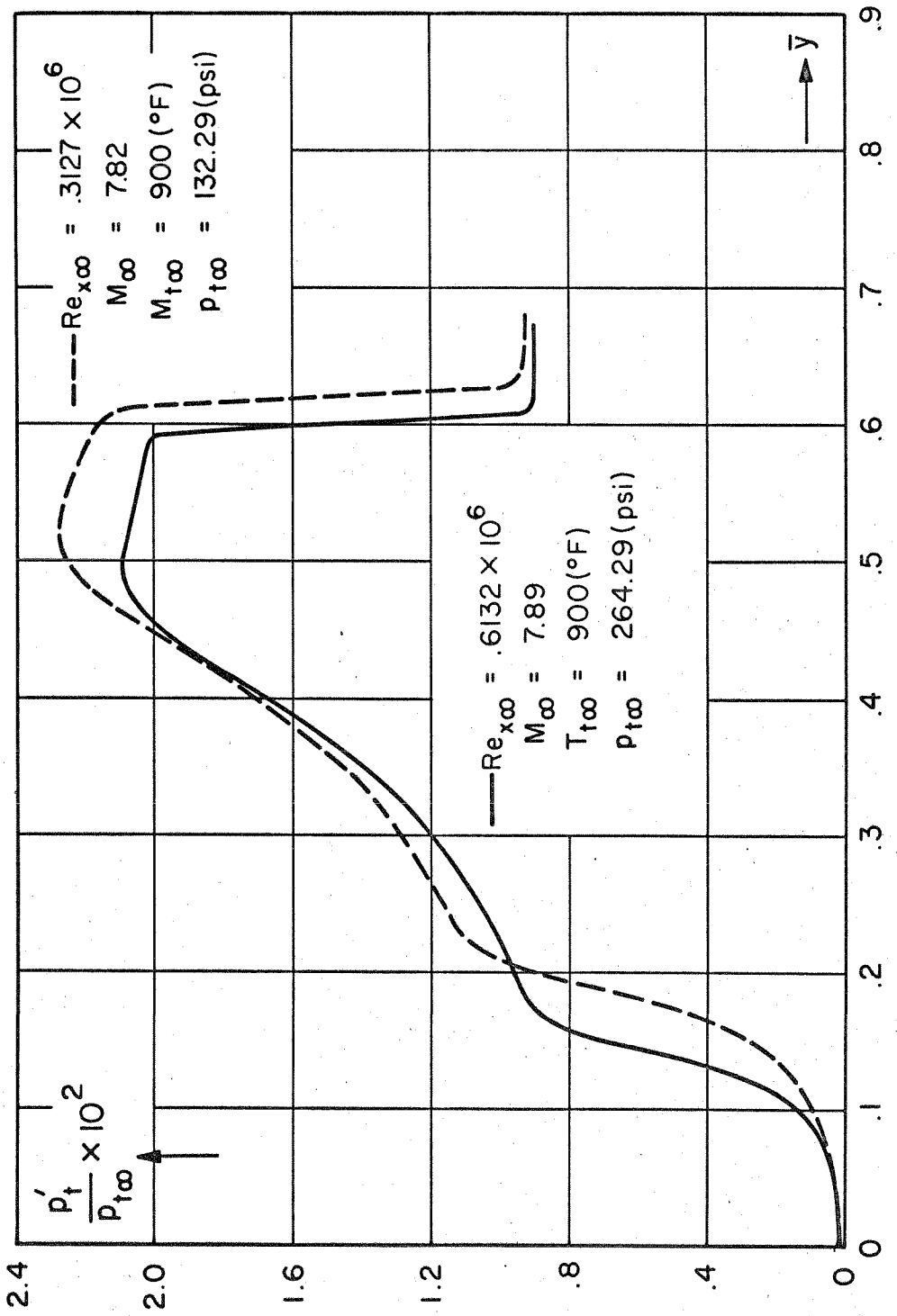

FIG. 6h. IMPACT PRESSURE PROFILES AT s = 1.225 IN.

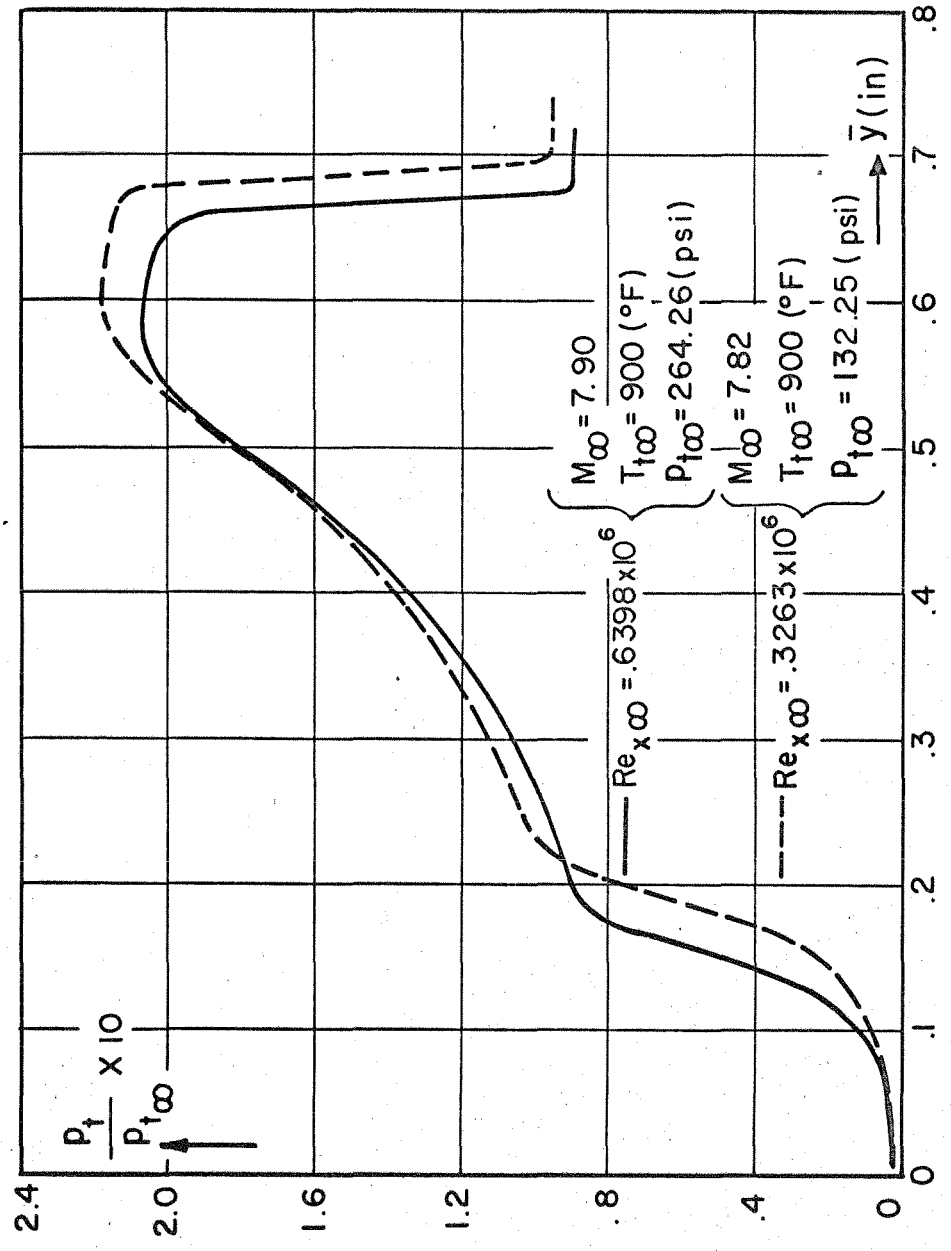

FIG. 6i. IMPACT PRESSURE PROFILES AT s = 1.48 in.

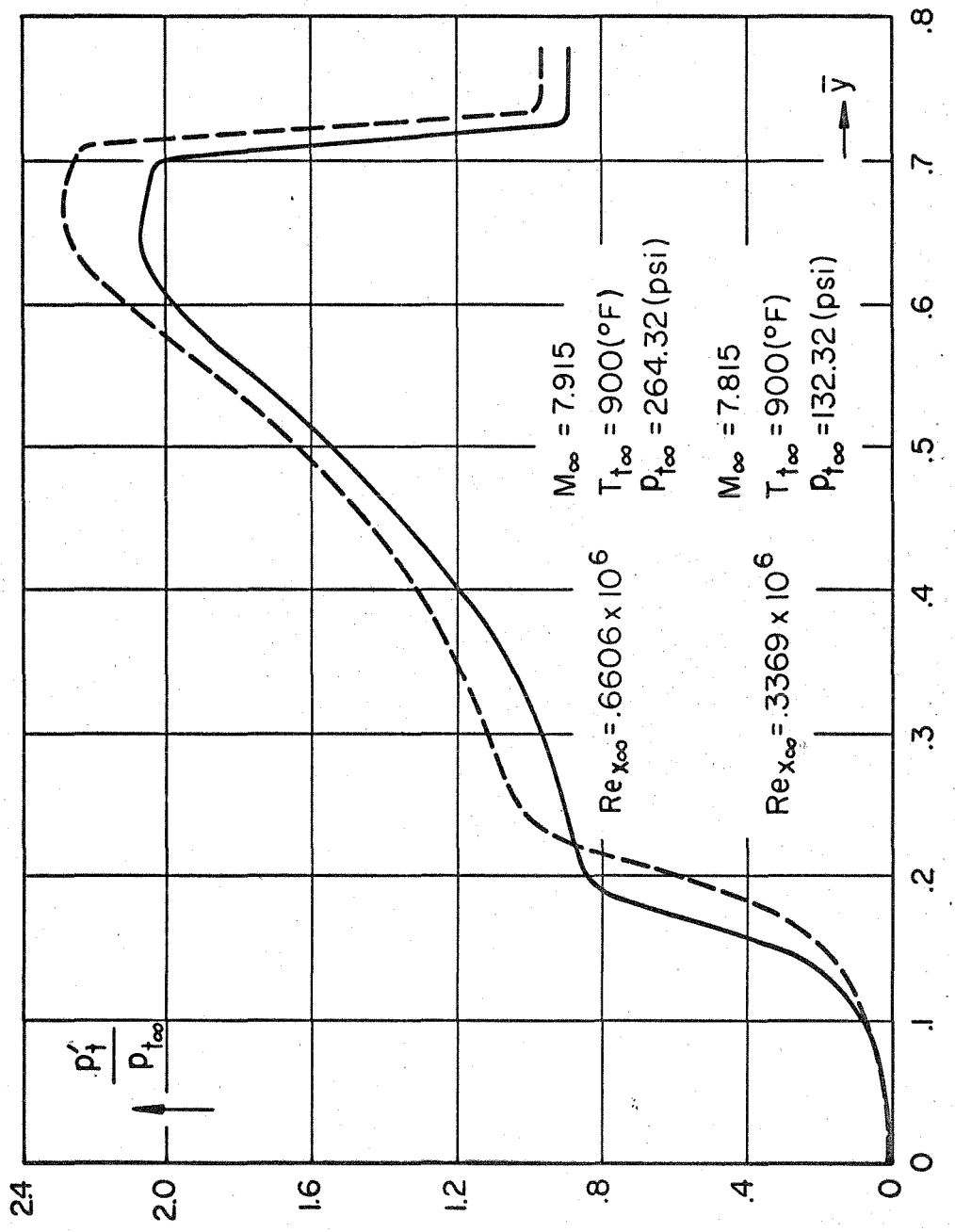

FIG. 6j. IMPACT PRESSURE PROFILES AT s = 1.68 IN.

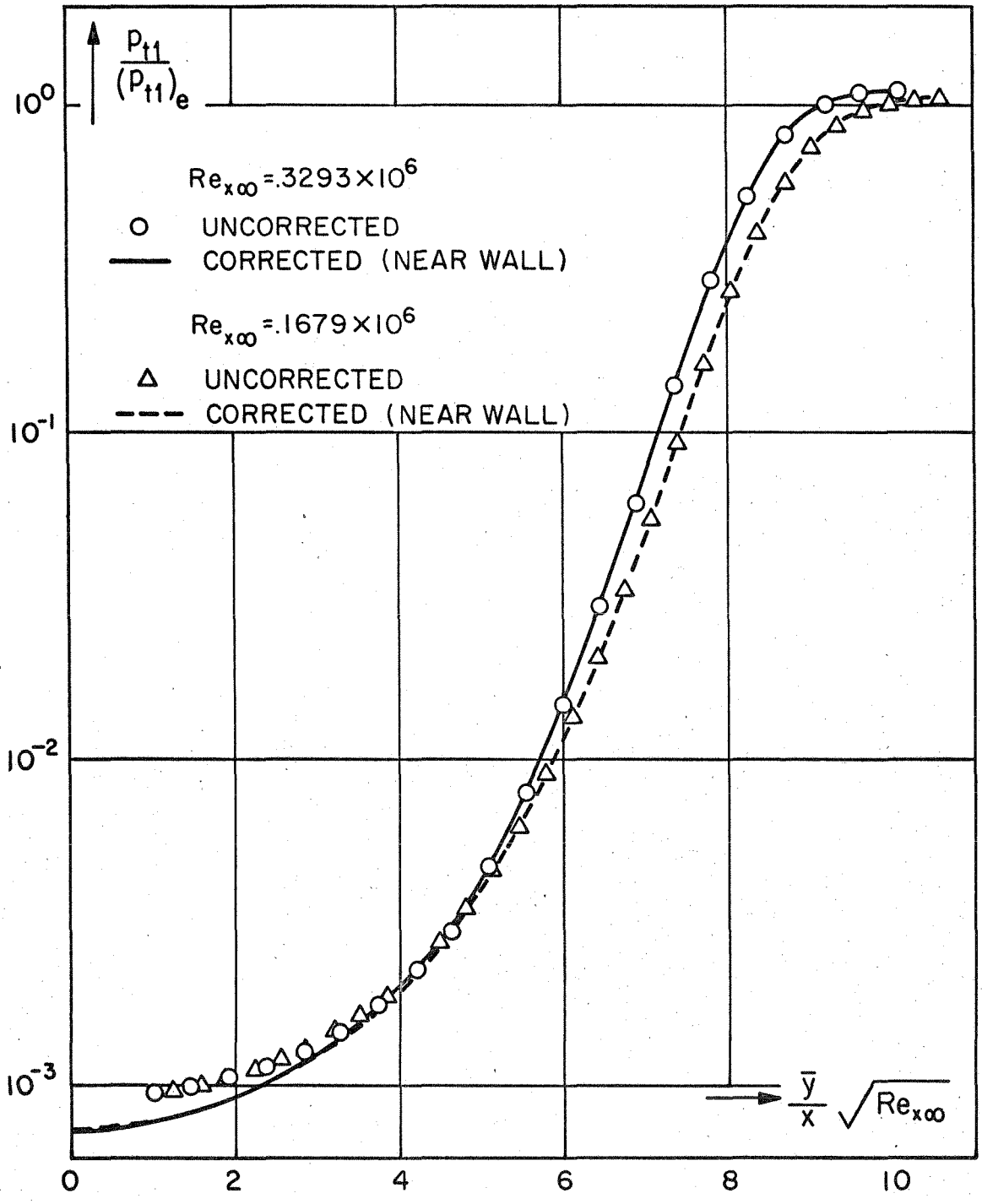

FIG. 7a. TOTAL PRESSURE PROFILES AT $-\bar{s} = 1.5$ IN.

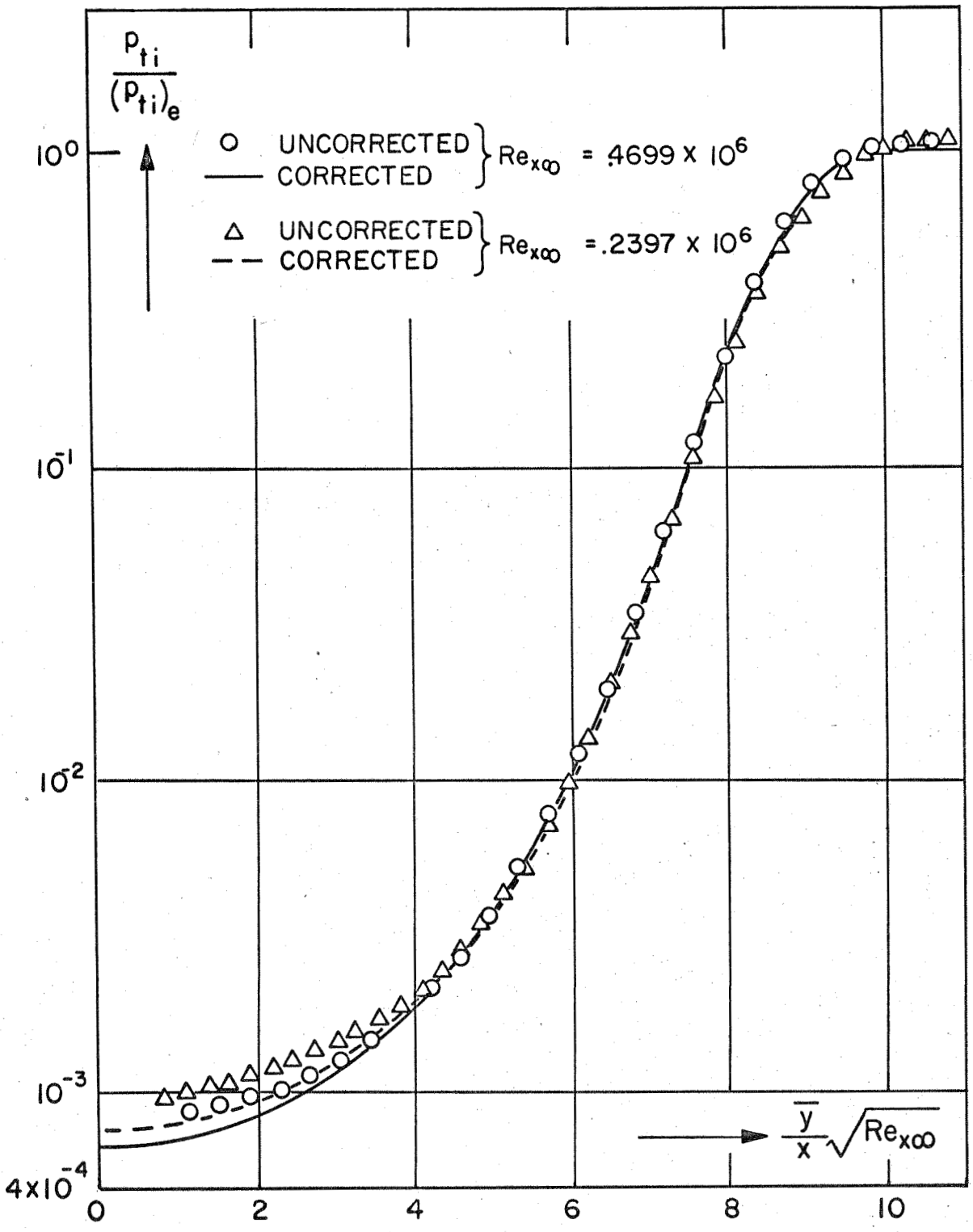

FIG. 7b. TOTAL PRESSURE PROFILES AT $-\bar{s}$ = .15 IN.

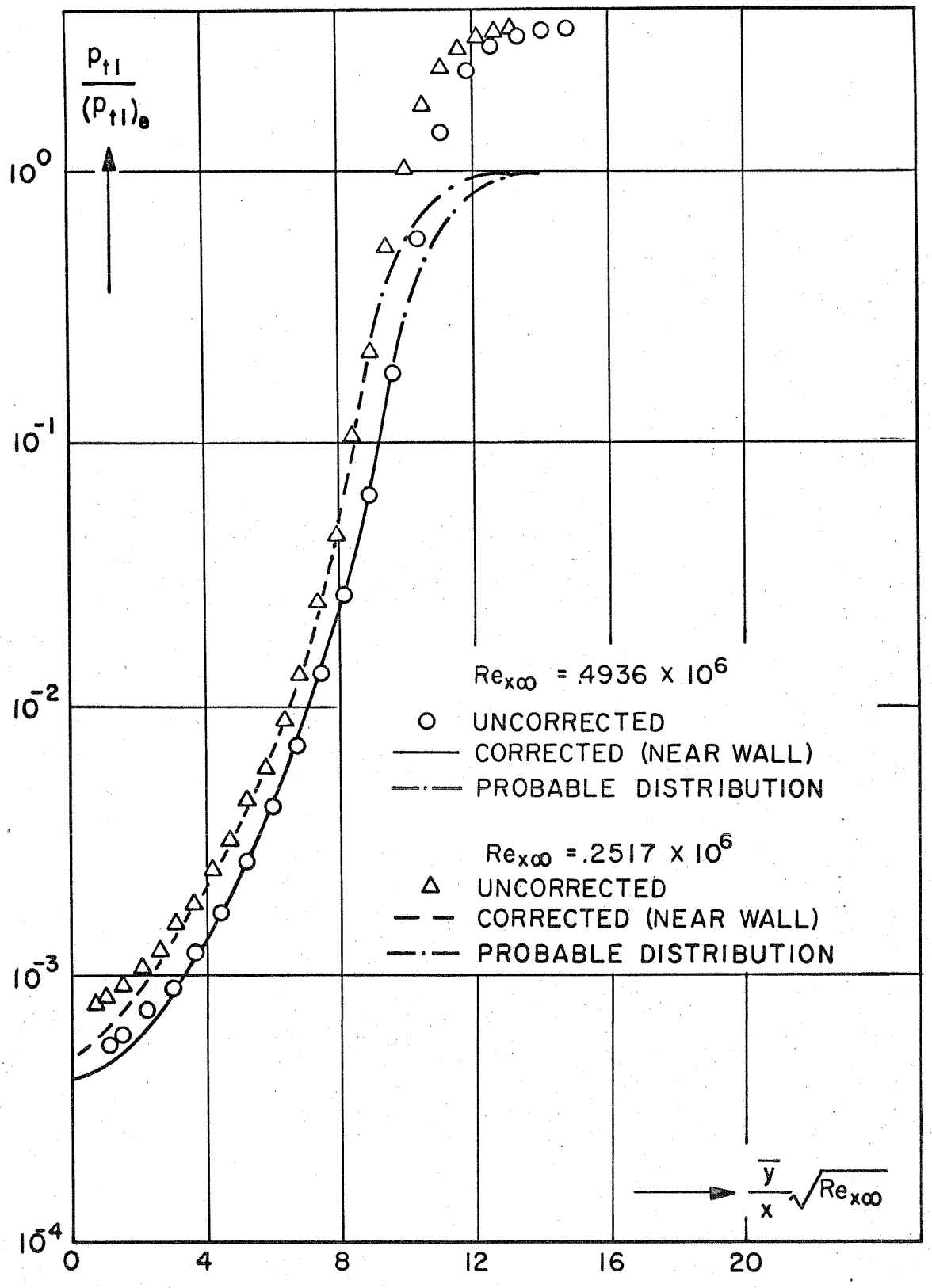

FIG. 7c. TOTAL PRESSURE PROFILES AT s = .0766 IN.

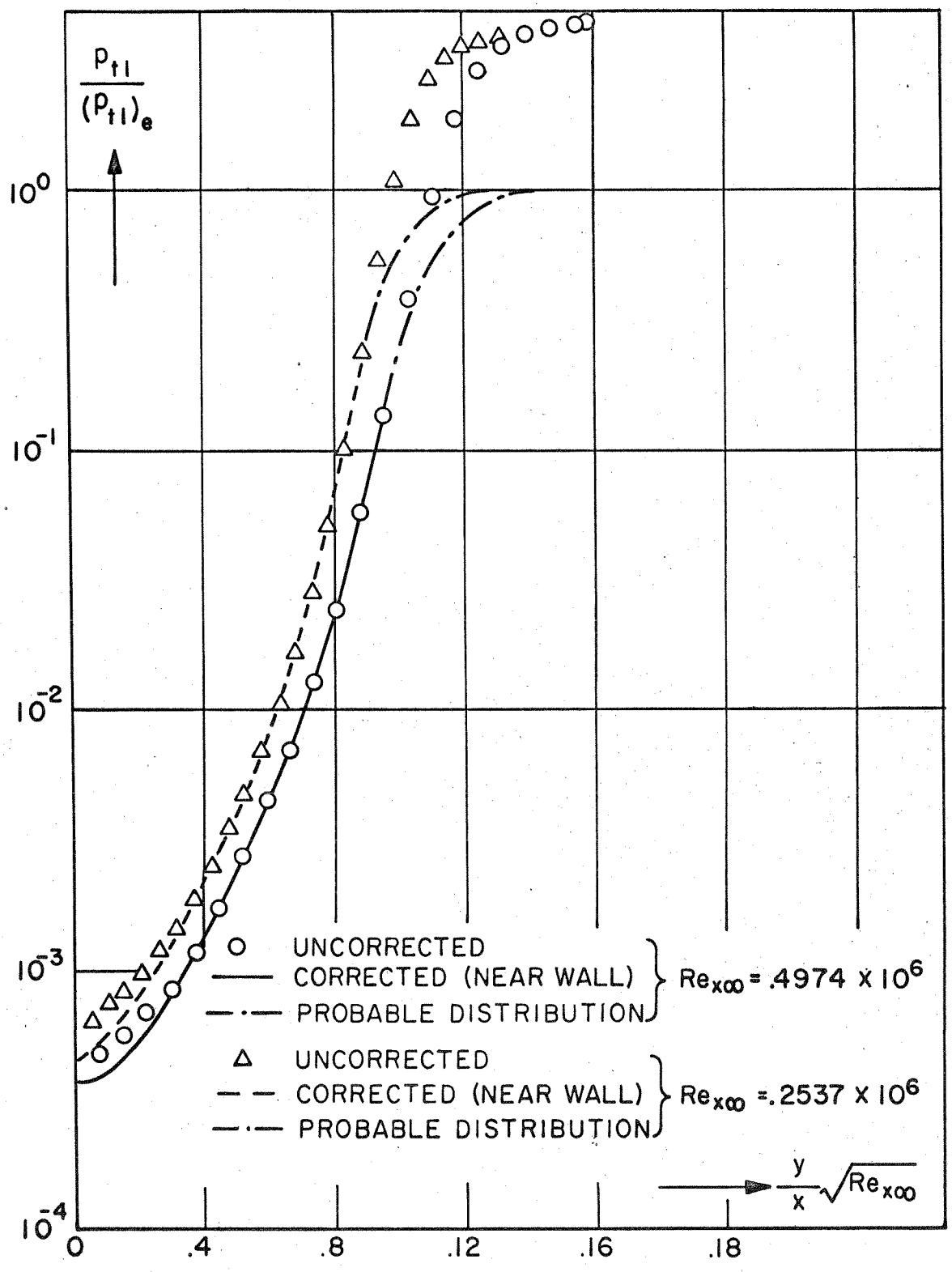

FIG. 7d. TOTAL PRESSURE PROFILES AT s = .1132 IN.

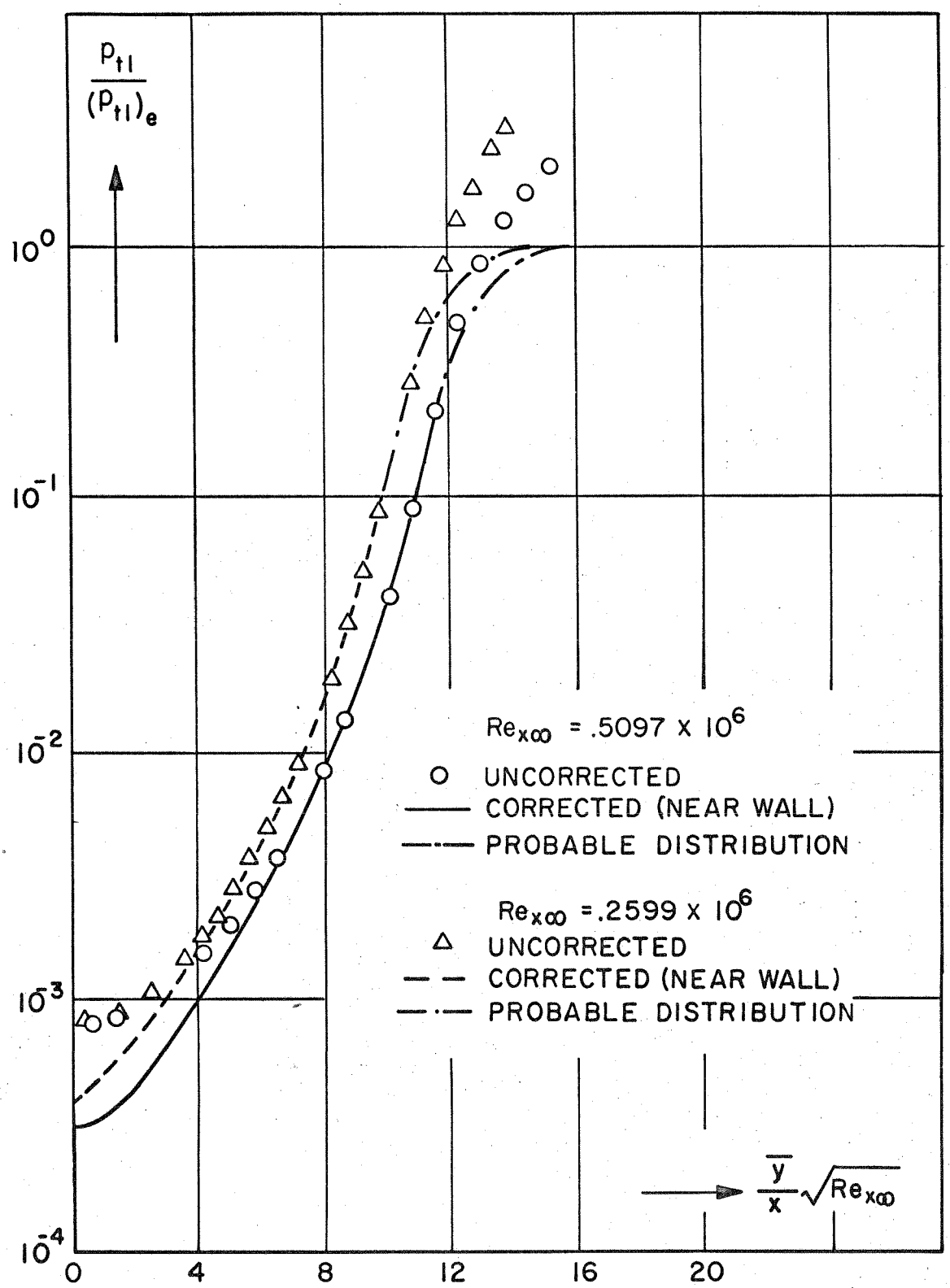

FIG. 7e. TOTAL PRESSURE PROFILES AT s = .2317 IN.

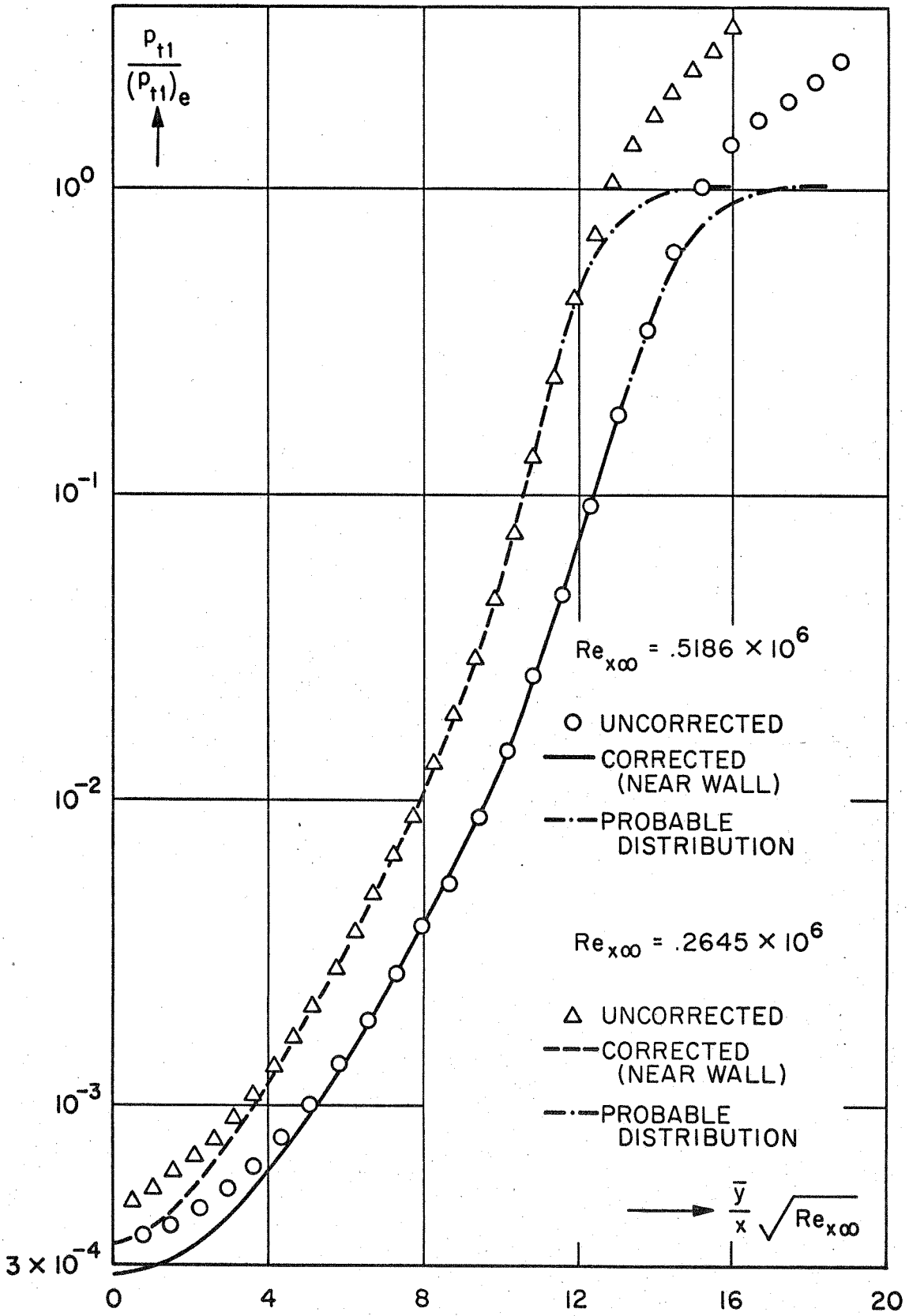

FIG. 7f. TOTAL PRESSURE PROFILES AT s = .317 IN.

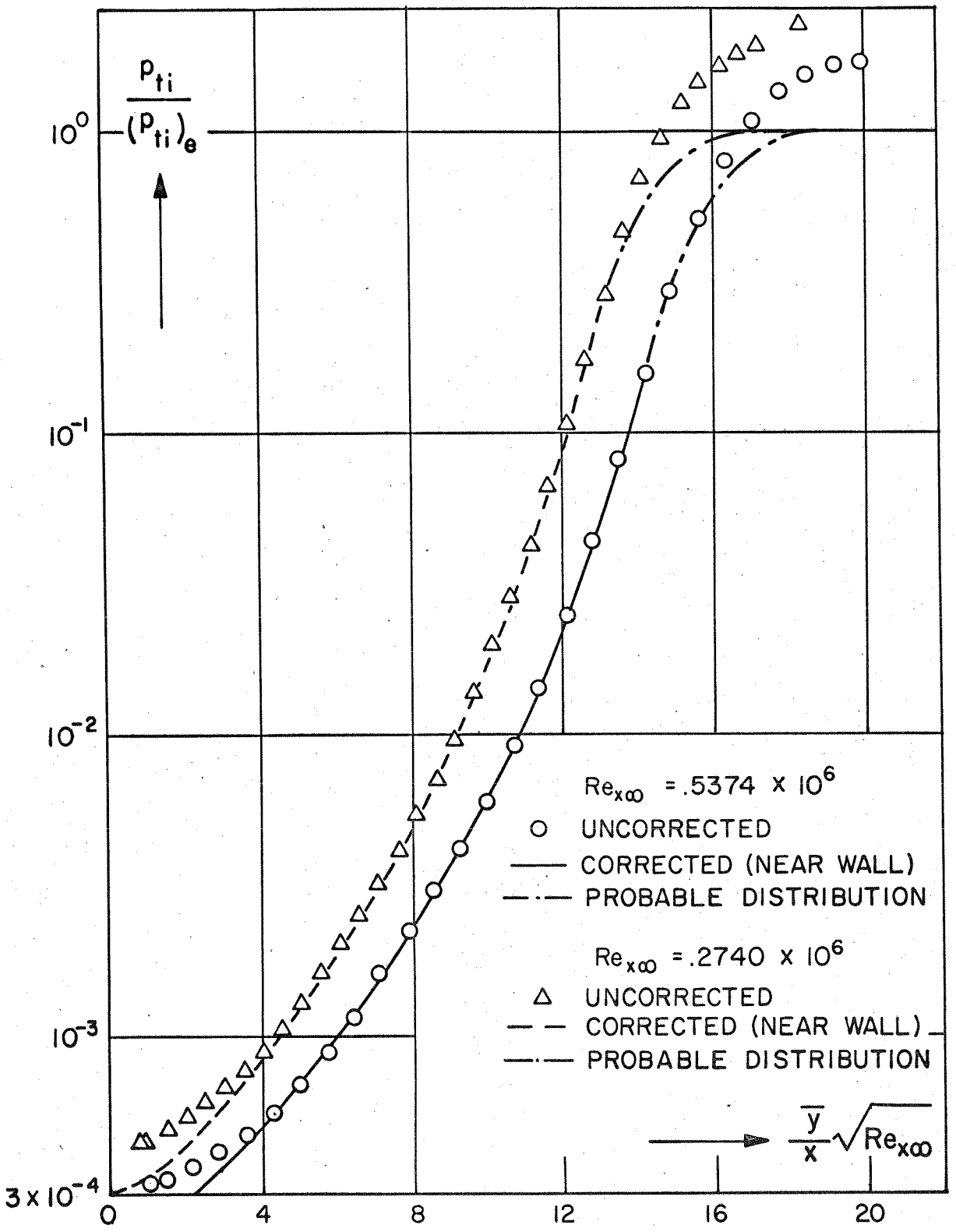

FIG. 7g. TOTAL PRESSURE PROFILES AT s = .497 IN.

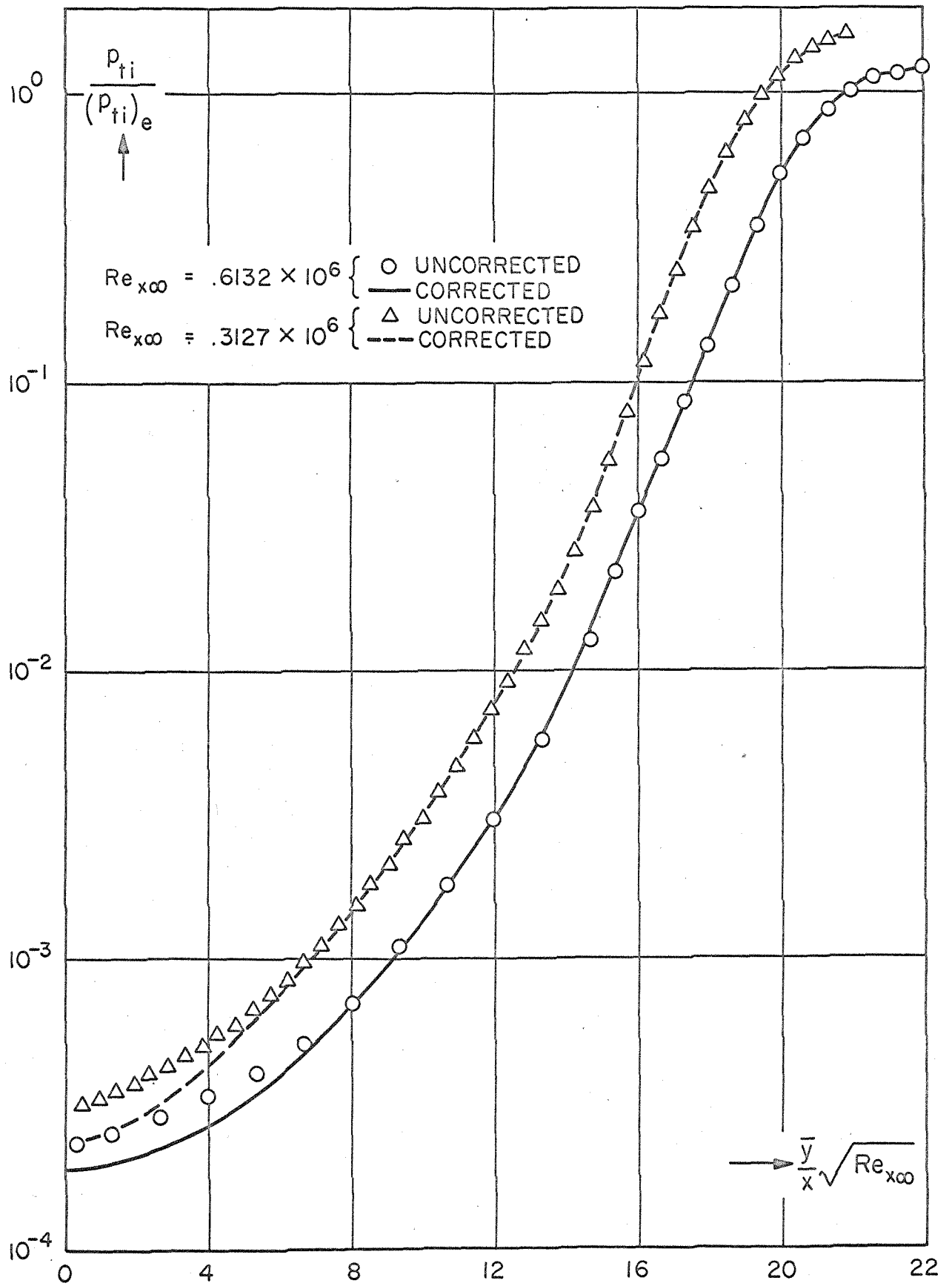

FIG. 7h. TOTAL PRESSURE PROFILES AT s = 1.225 IN.

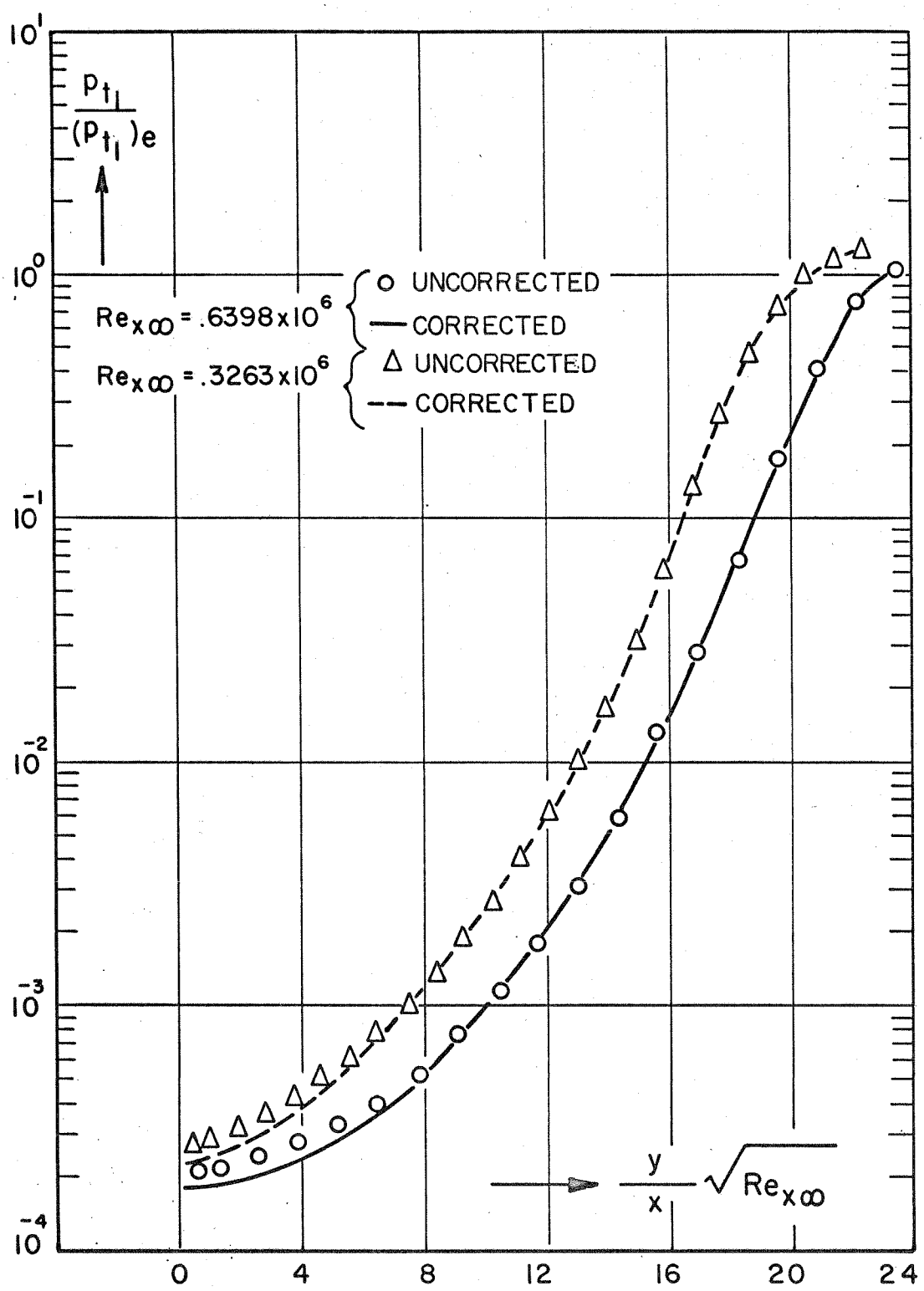

FIG. 7i. TOTAL PRESSURE PROFILES AT s=1.48 IN.

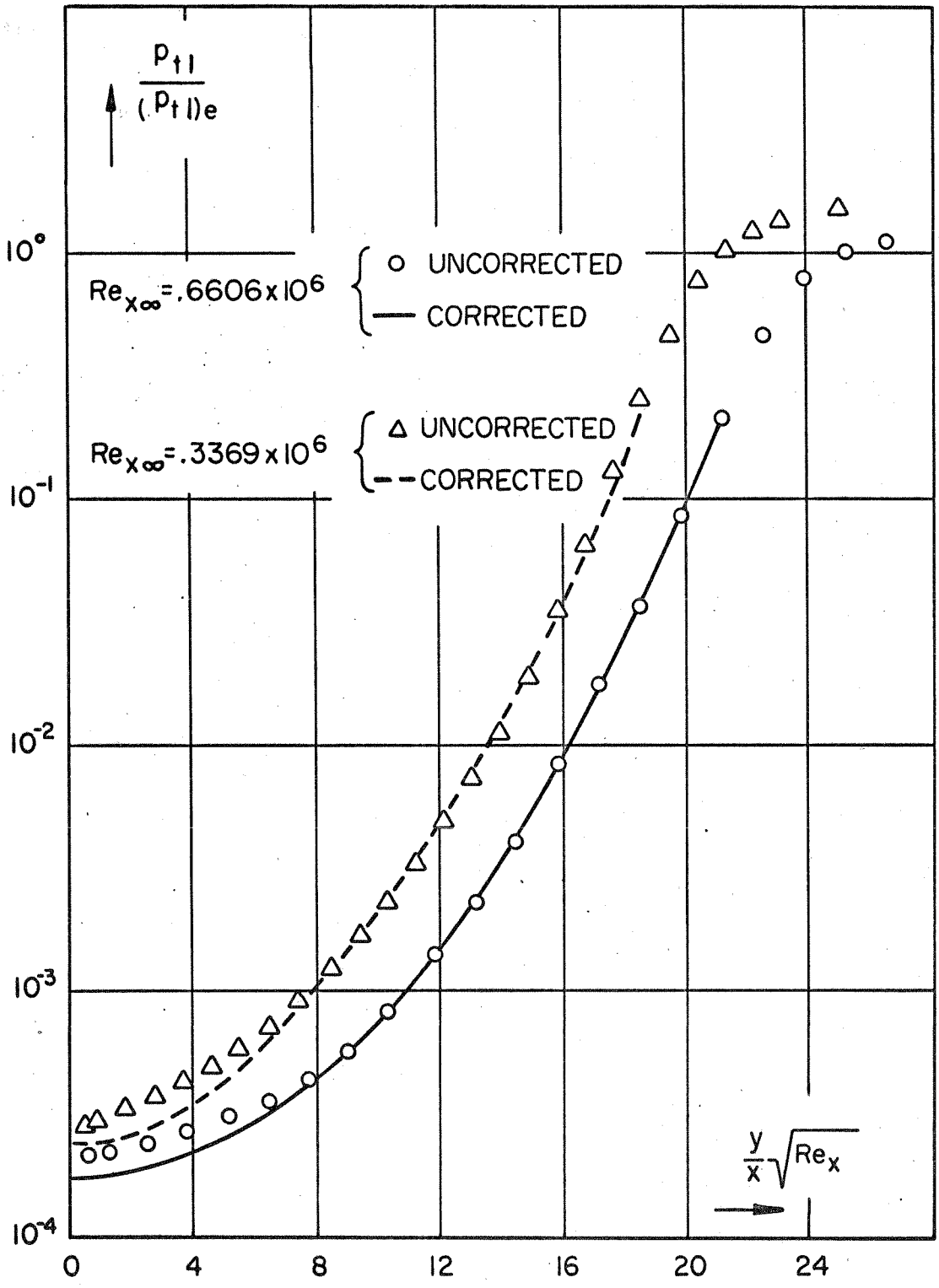

FIG. 7j. TOTAL PRESSURE PROFILES AT s = 1.68 IN.

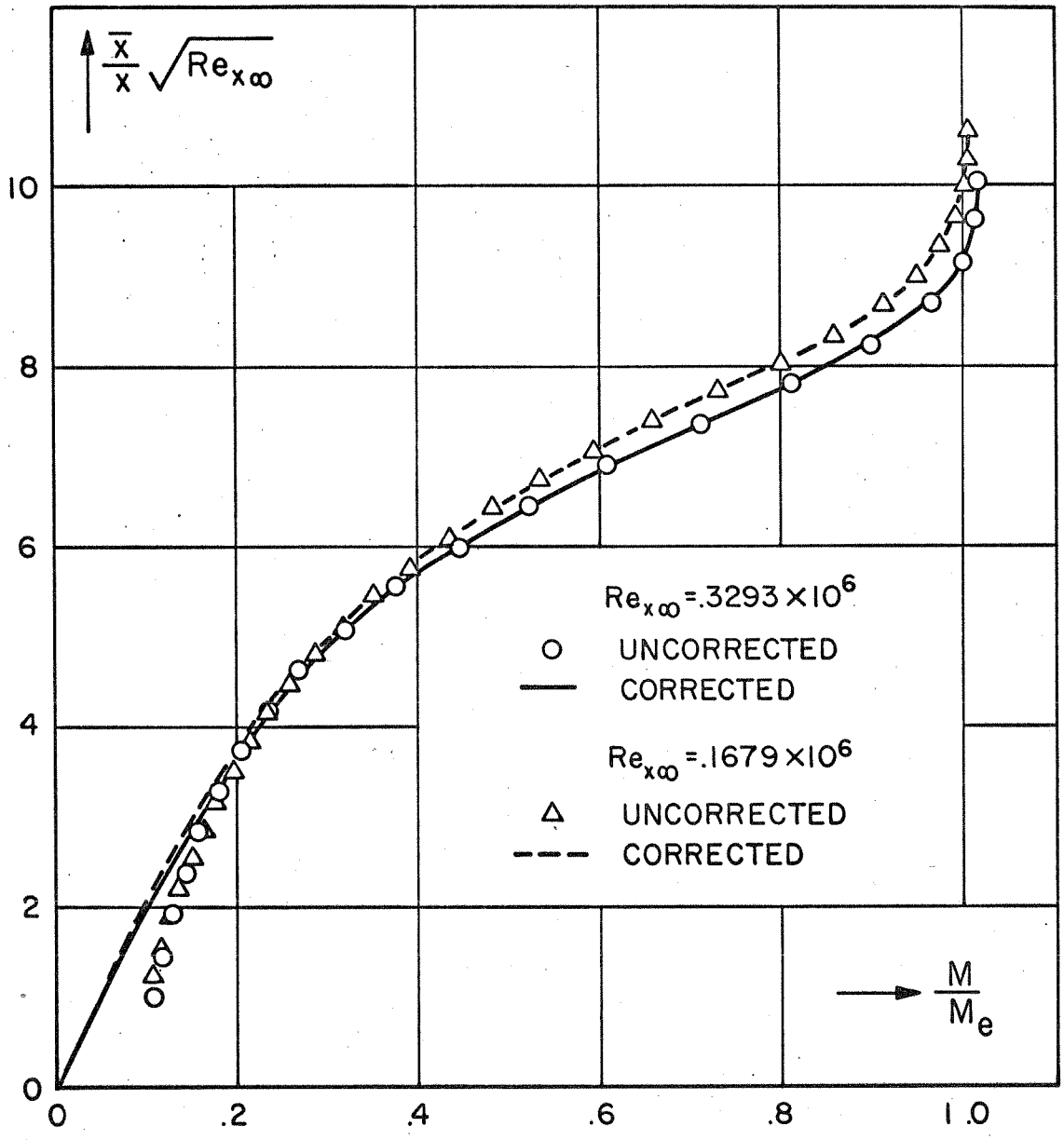

FIG. 8a. MACH NUMBER PROFILES AT $-\bar{s}$=1.5 IN.

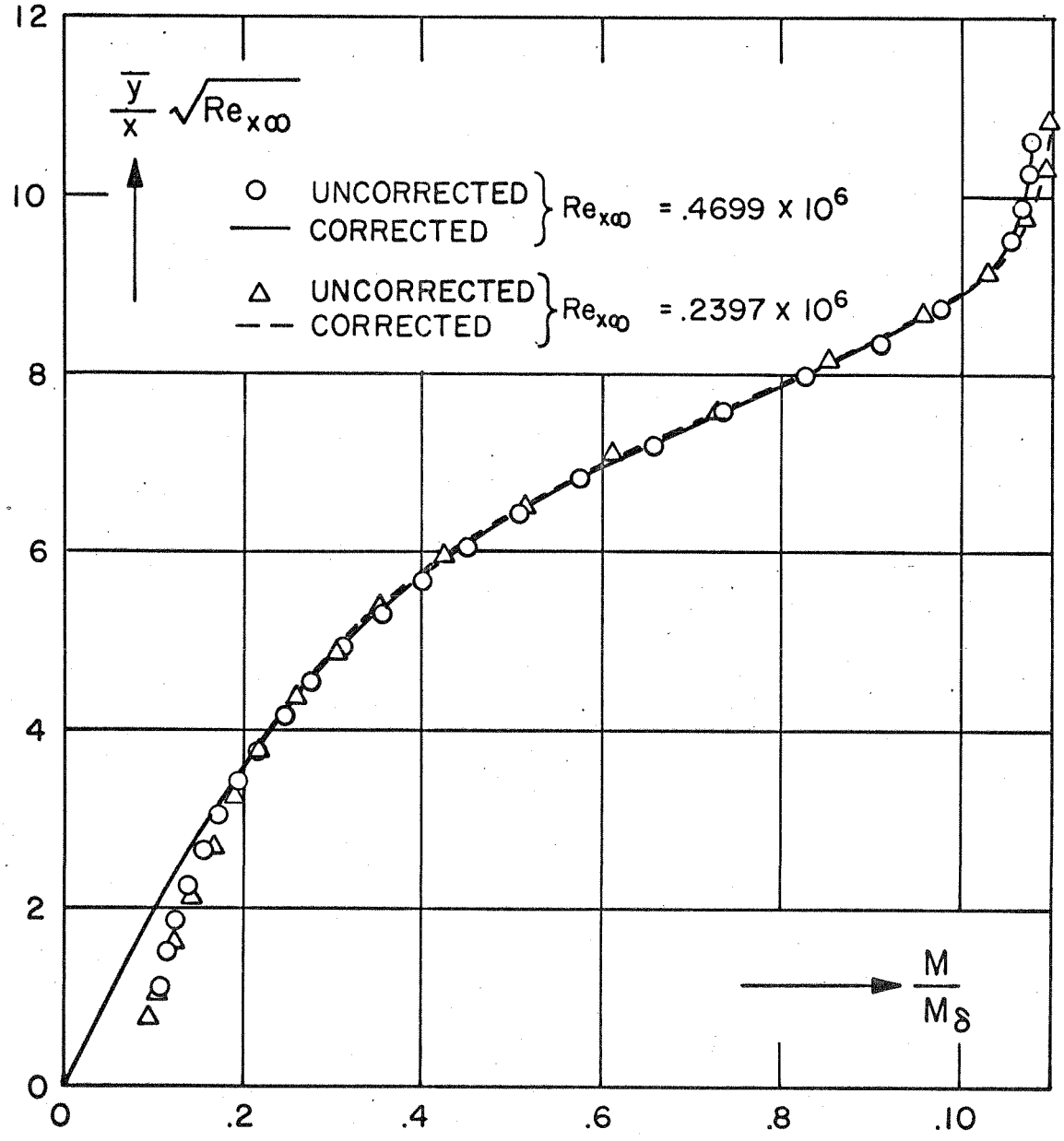

FIG. 8b. MACH NUMBER PROFILES AT $-\bar{s}$ = .15 IN.

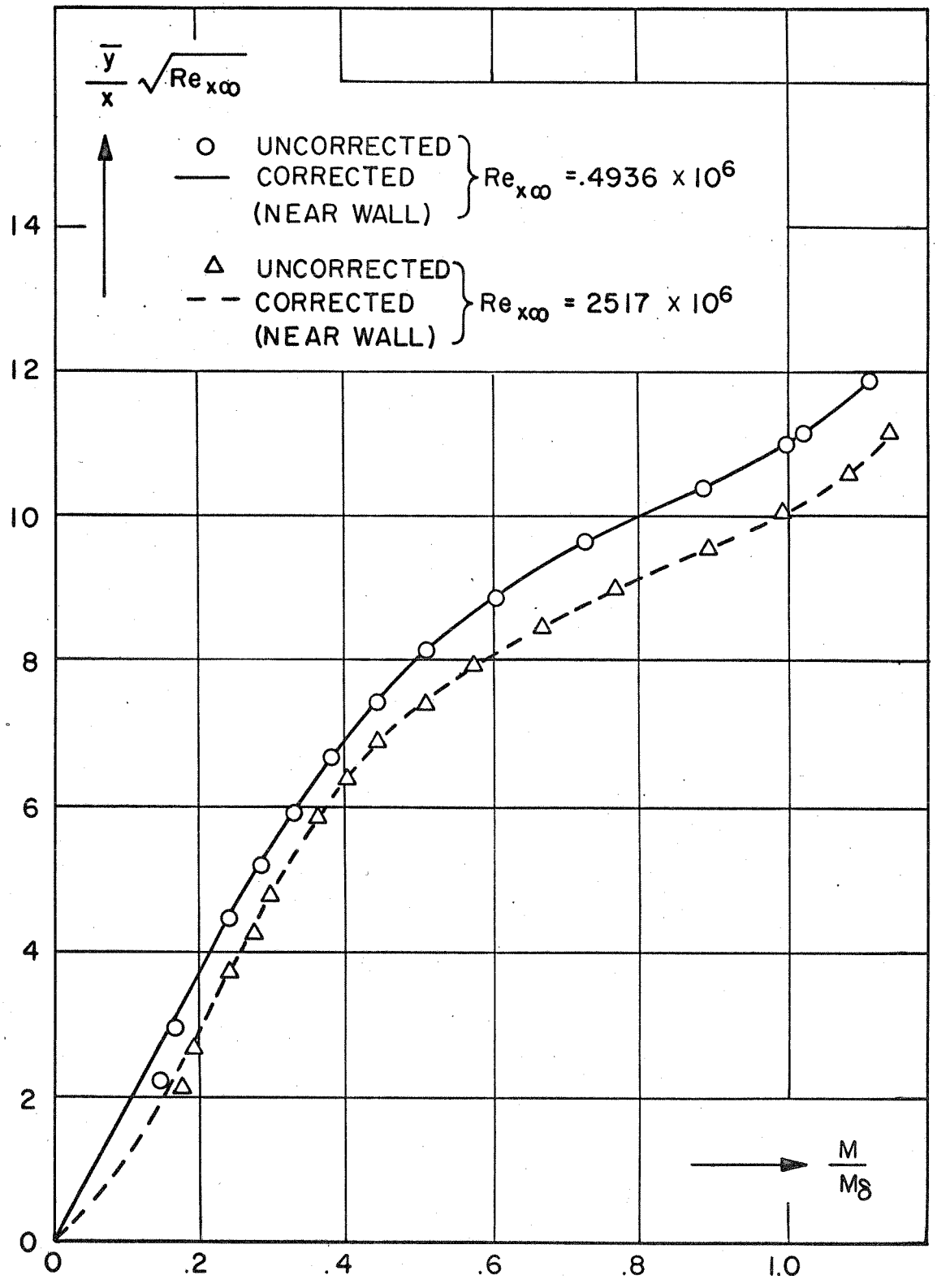

FIG. 8c. MACH NUMBER PROFILES AT s = .0766 IN.

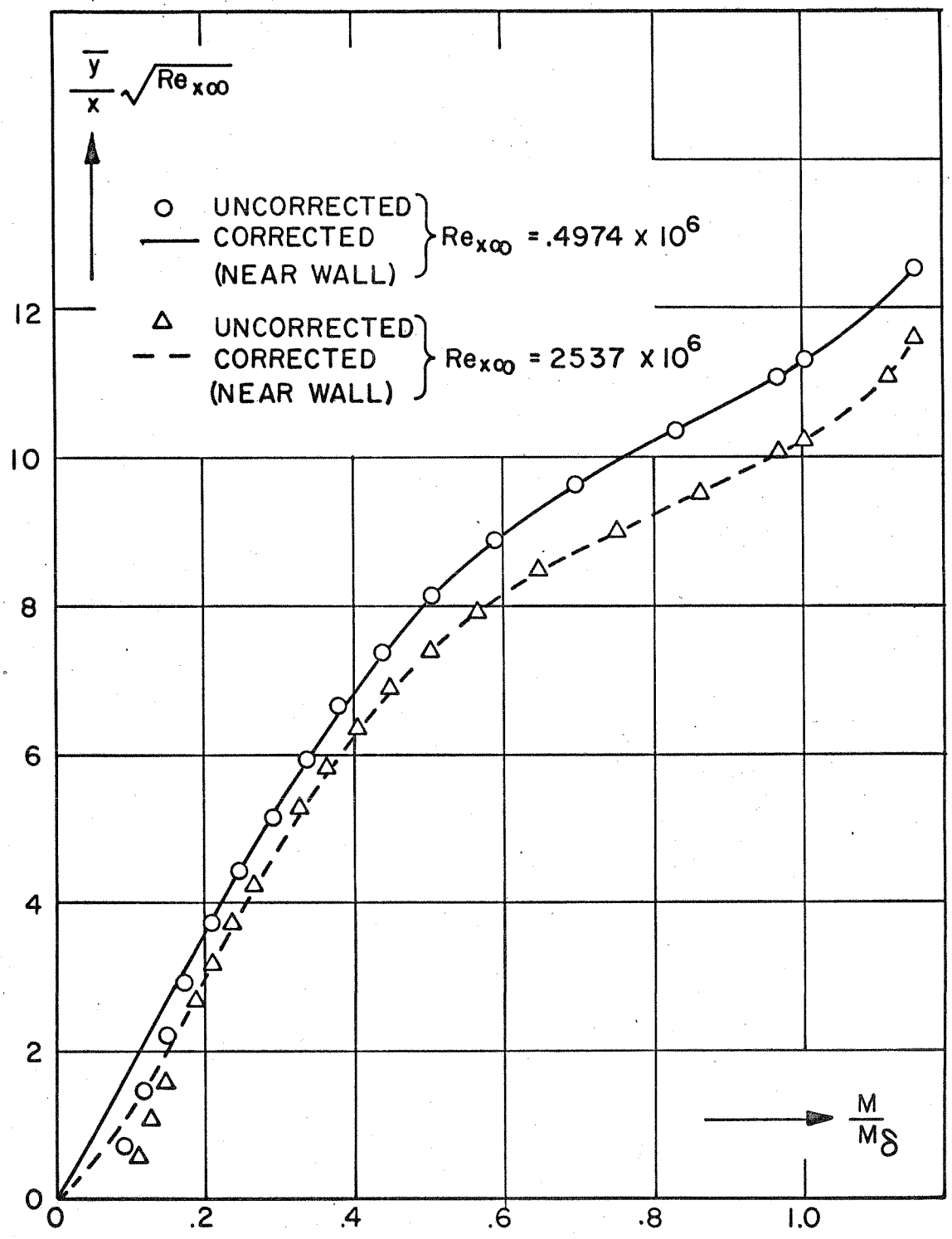

FIG. 8d. MACH NUMBER PROFILES AT s = .1132 IN.

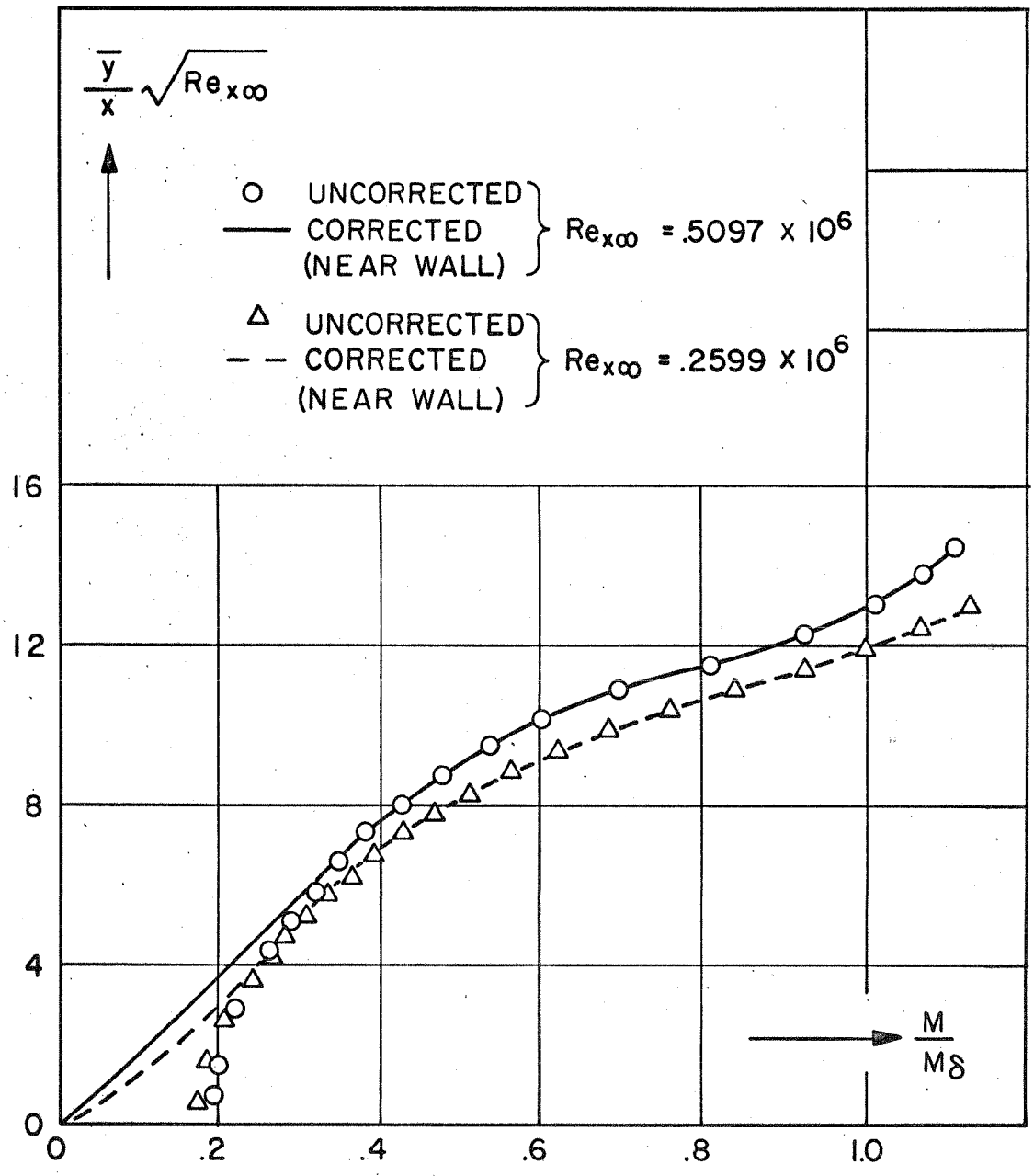

FIG. 8e. MACH NUMBER PROFILES AT s = .2317 IN.

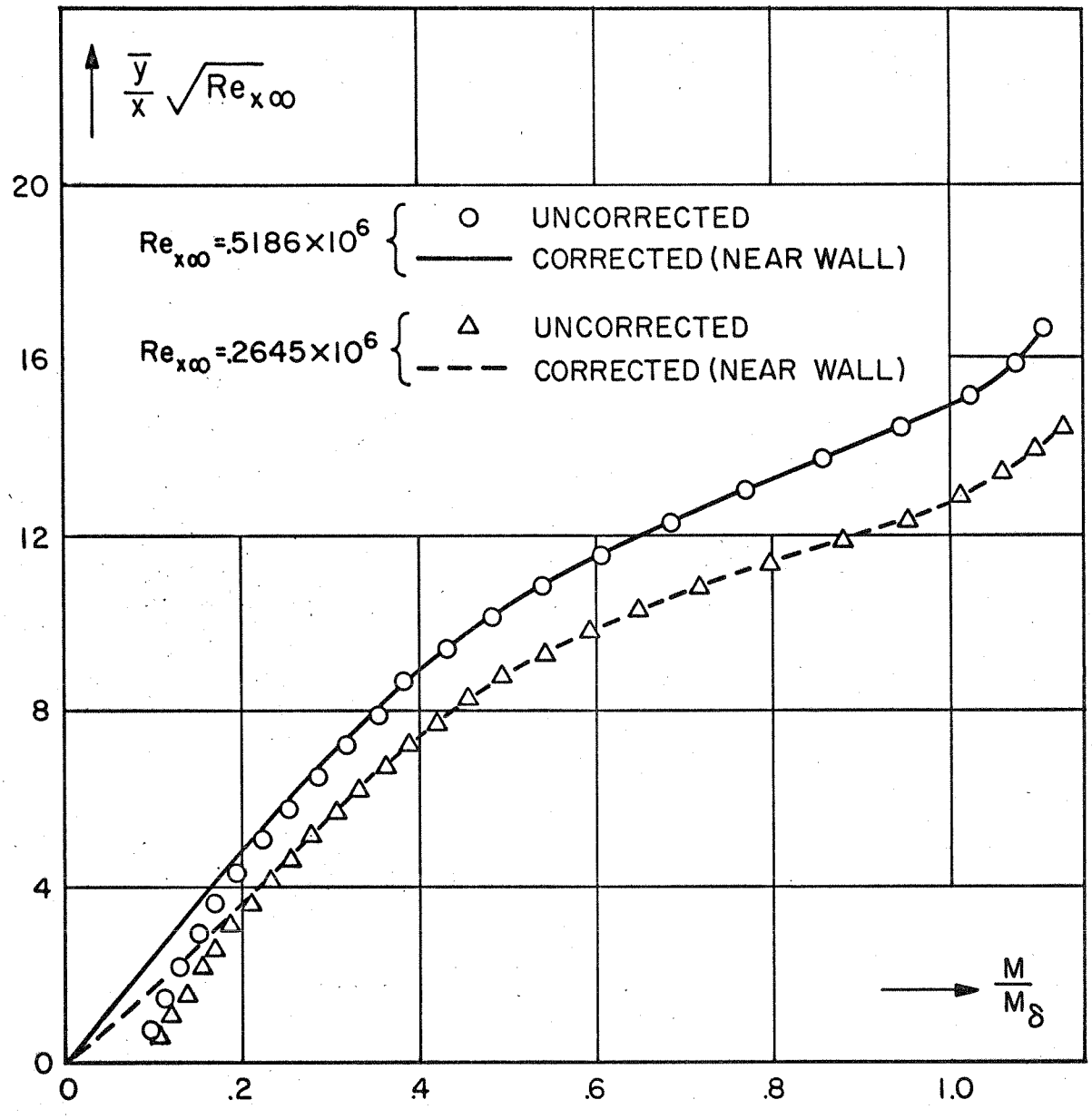

FIG. 8f. MACH NUMBER PROFILES AT s = .317 IN.

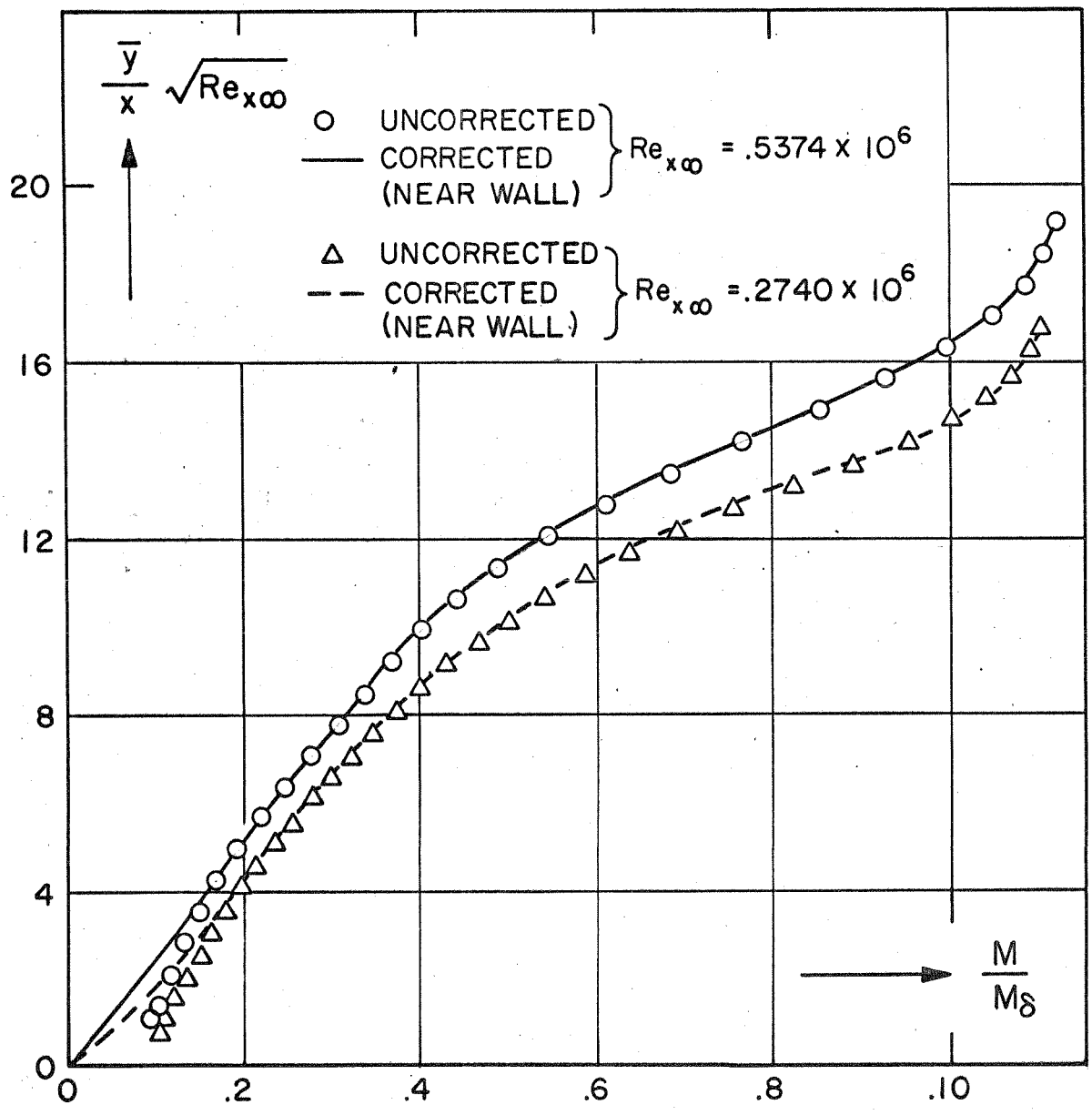

FIG. 8g. MACH NUMBER PROFILES AT s = .497 IN.

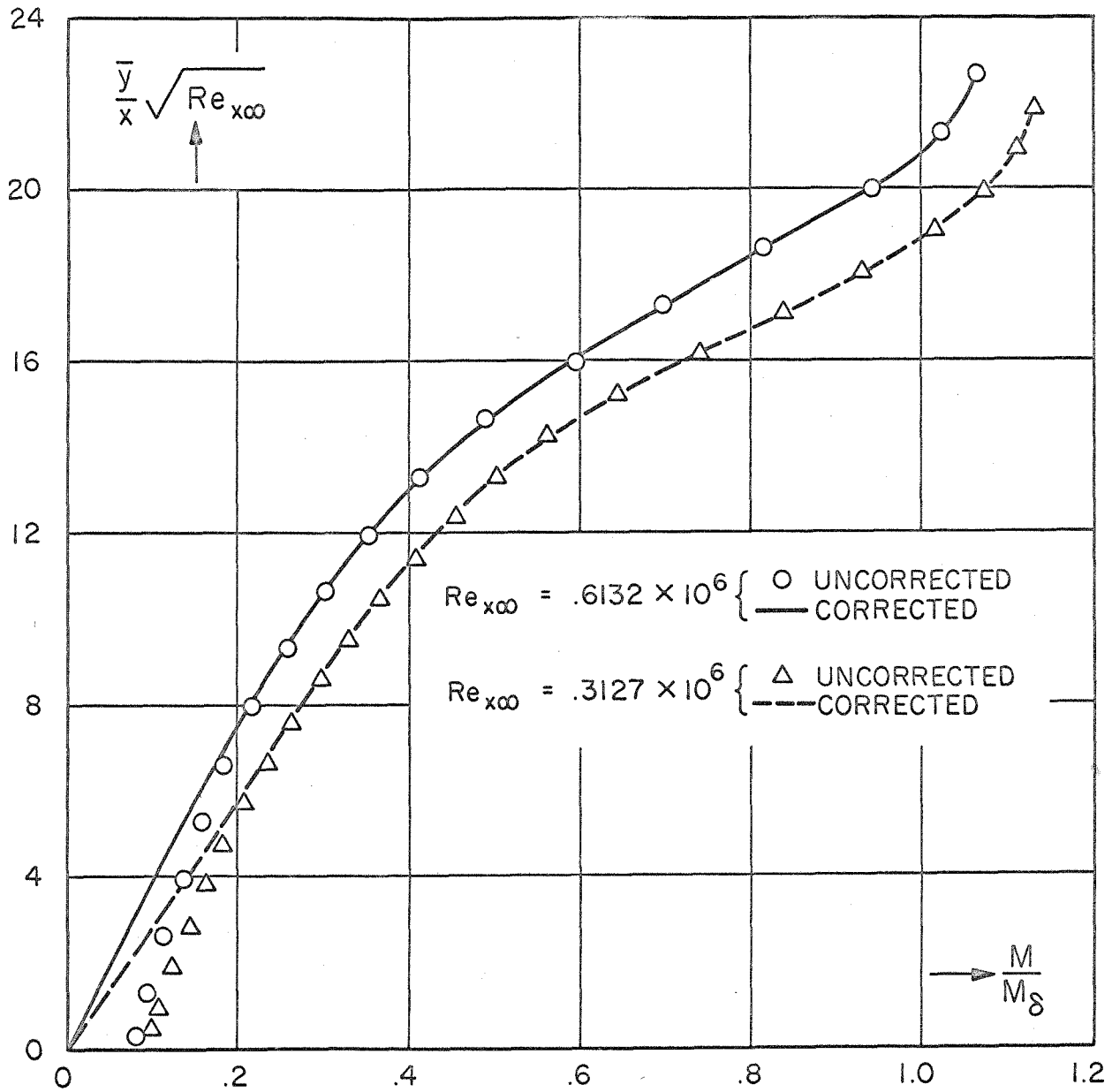

FIG. 8h. MACH NUMBER PROFILES AT s = 1.225 IN.

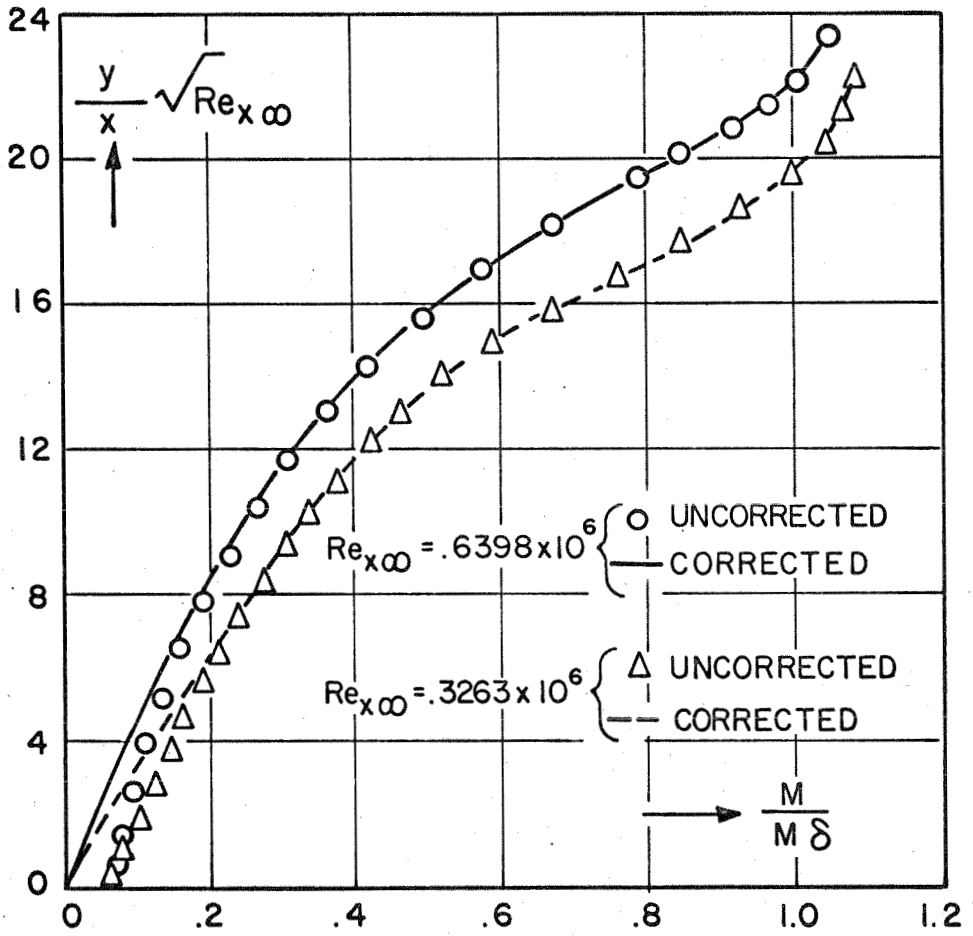

FIG. 8i. MACH NUMBER PROFILES AT s = 1.48 IN.

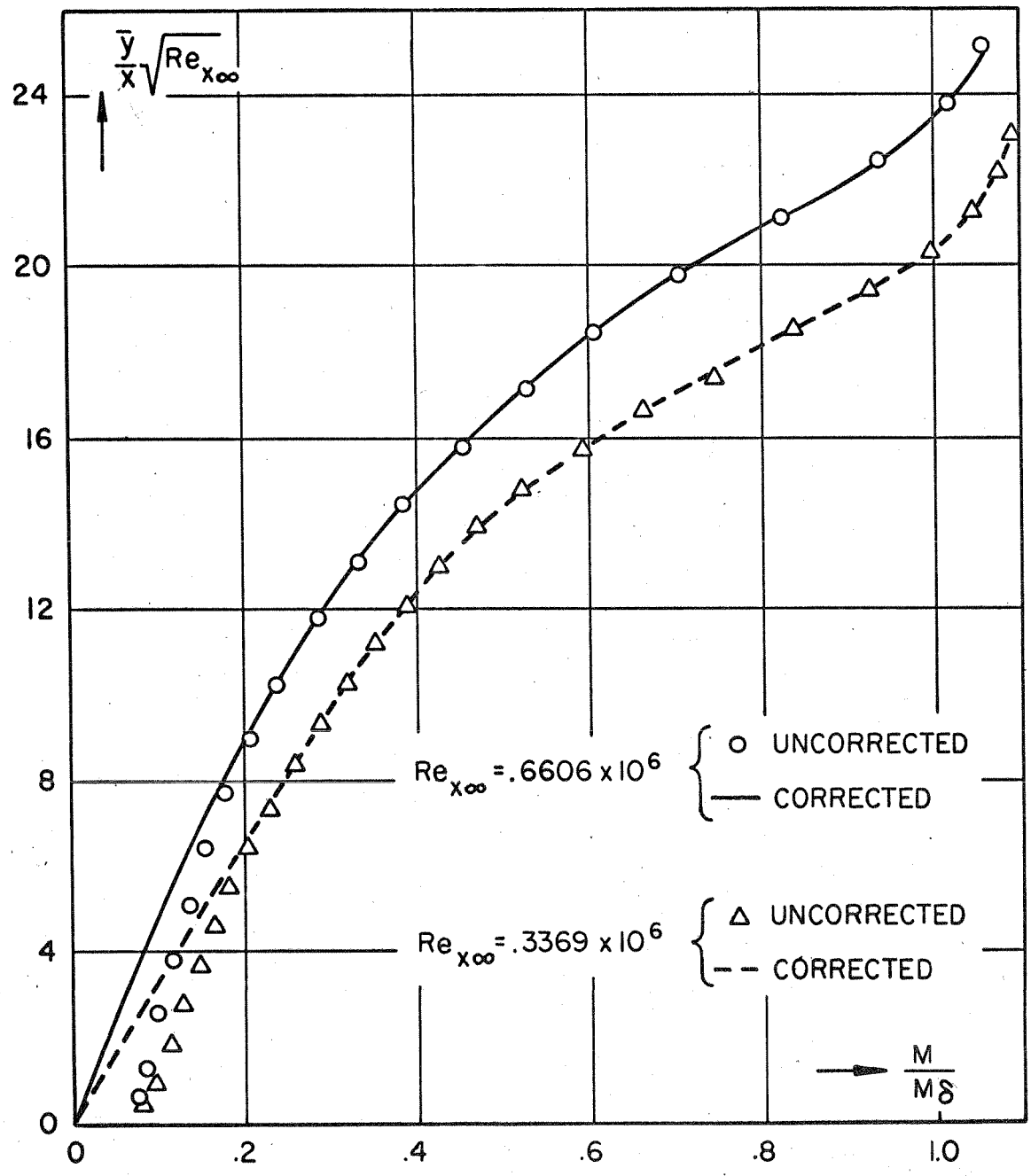

FIG. 8j. MACH NUMBER PROFILES AT s = 1.68 IN.

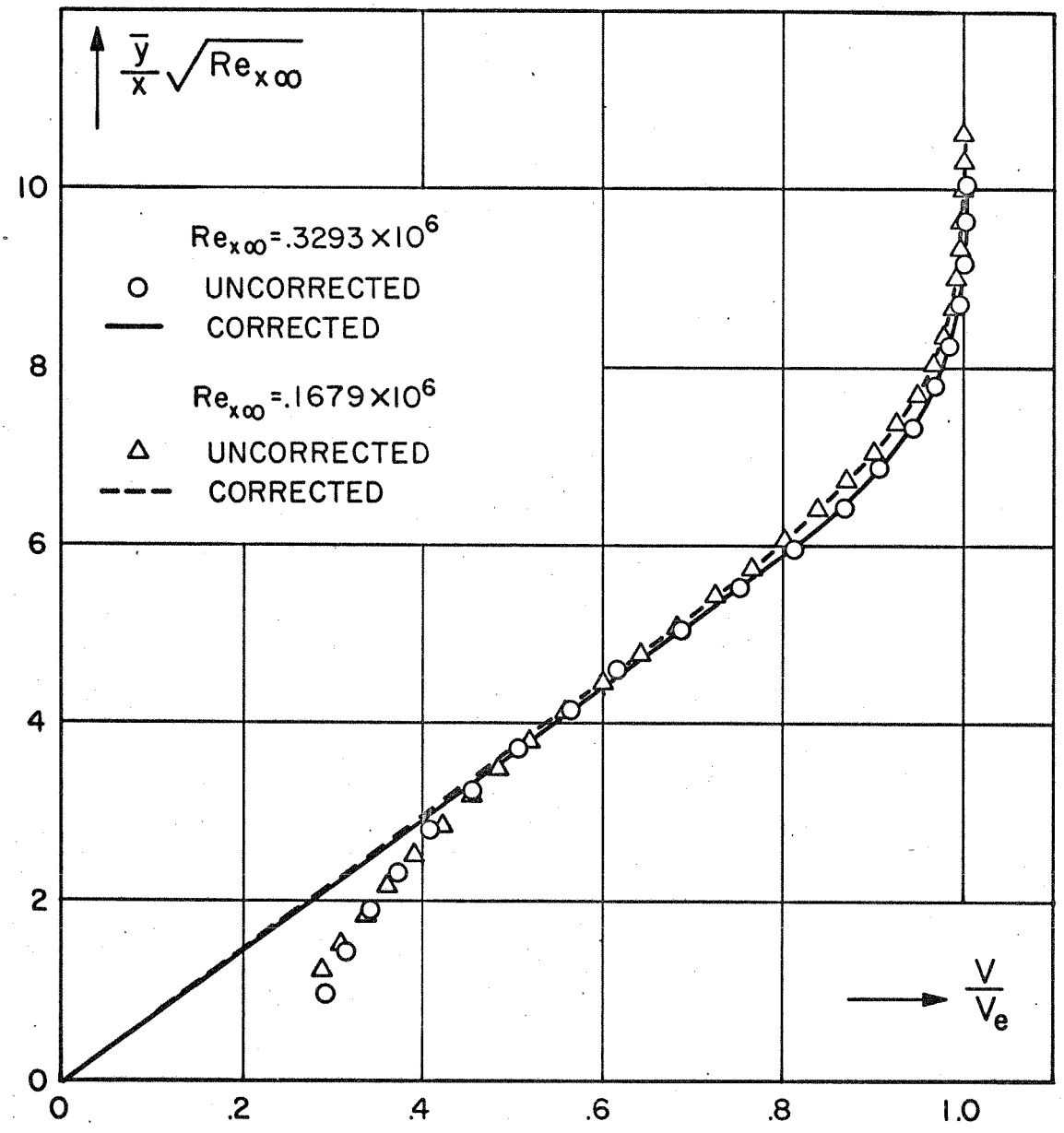

FIG. 9a. VELOCITY PROFILES AT $-\bar{s}$ = 1.5 IN.

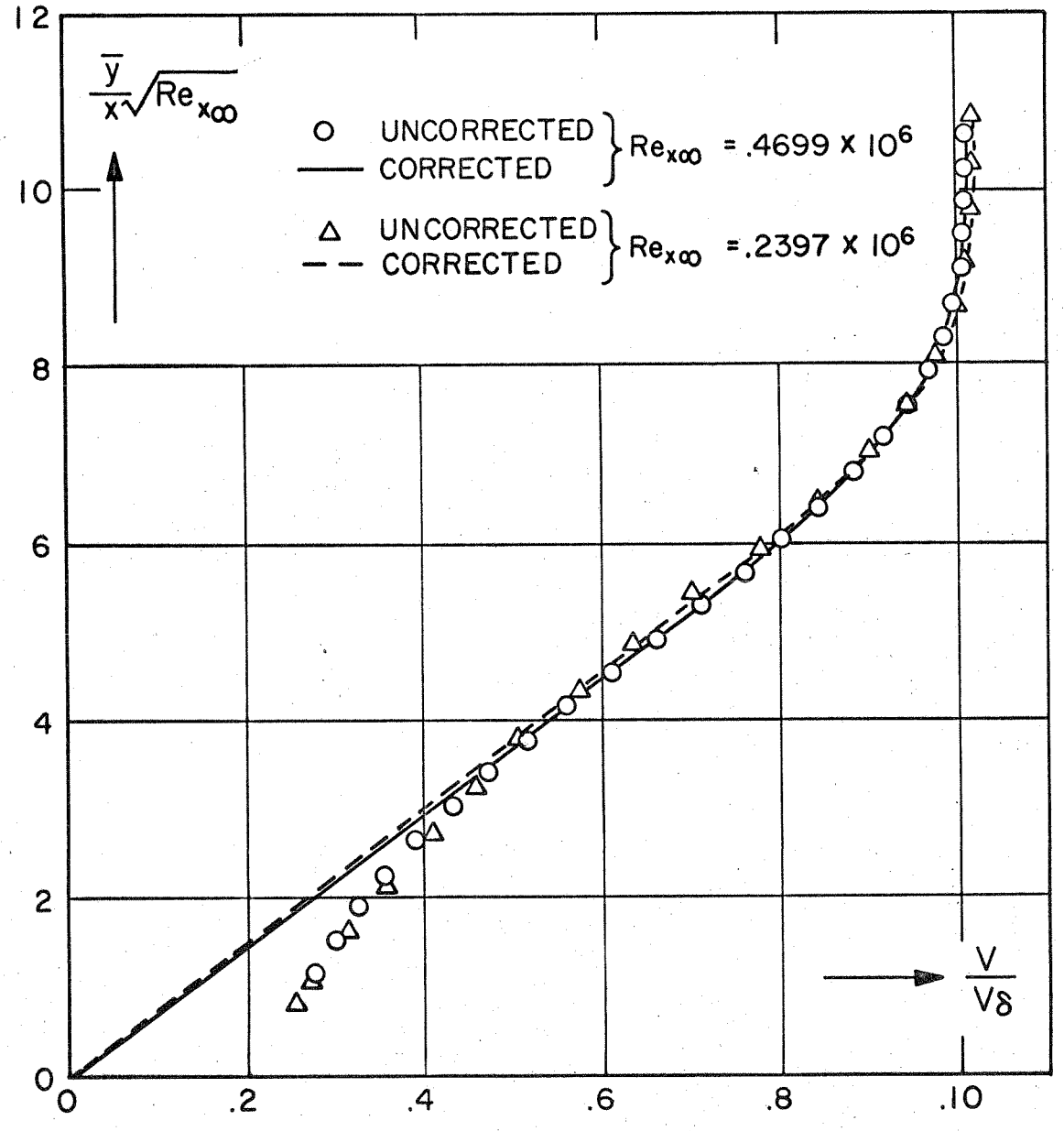

FIG. 9b. VELOCITY PROFILES AT $\bar{s}$ = .15 IN

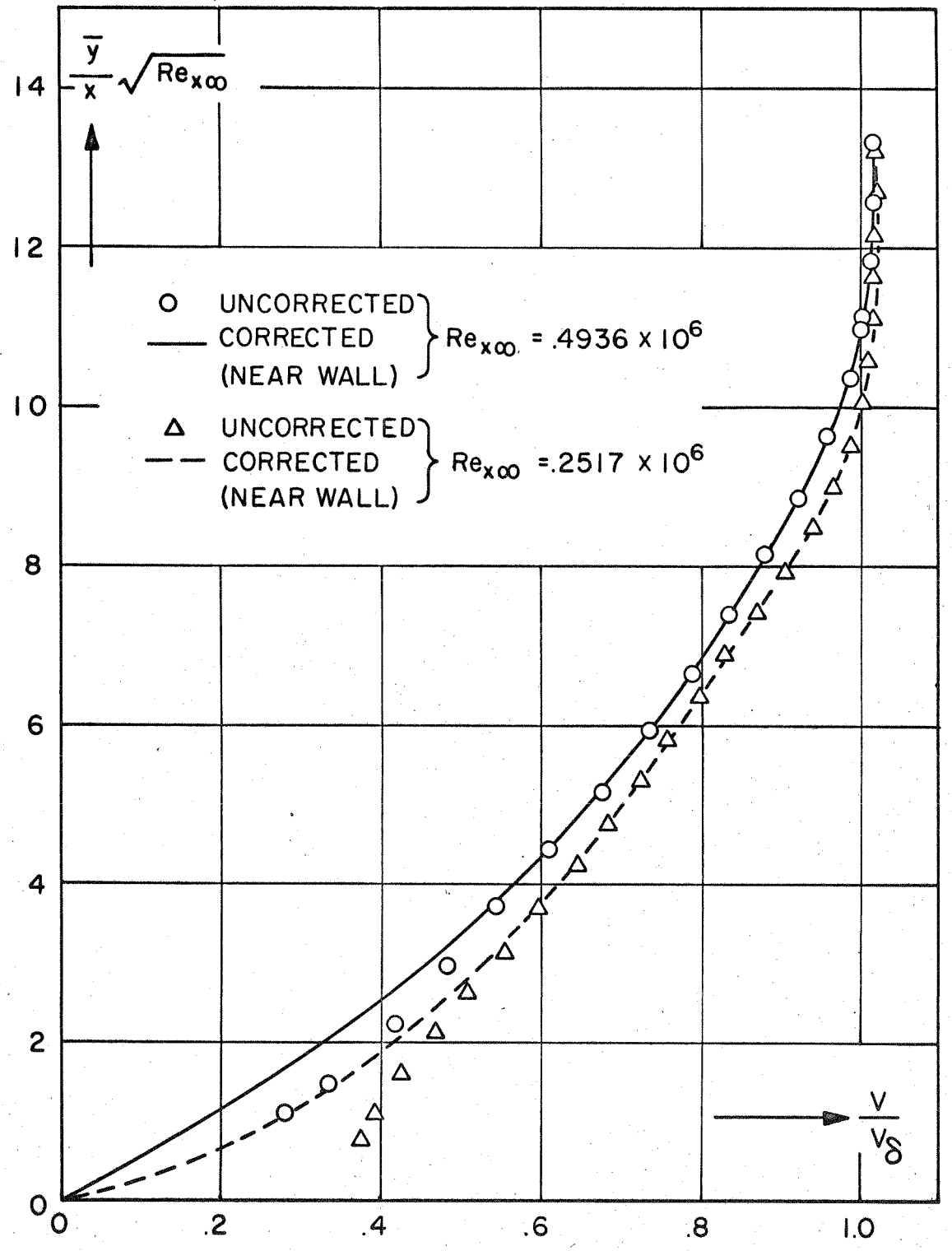

FIG. 9c. VELOCITY PROFILES AT s = .0766 IN.

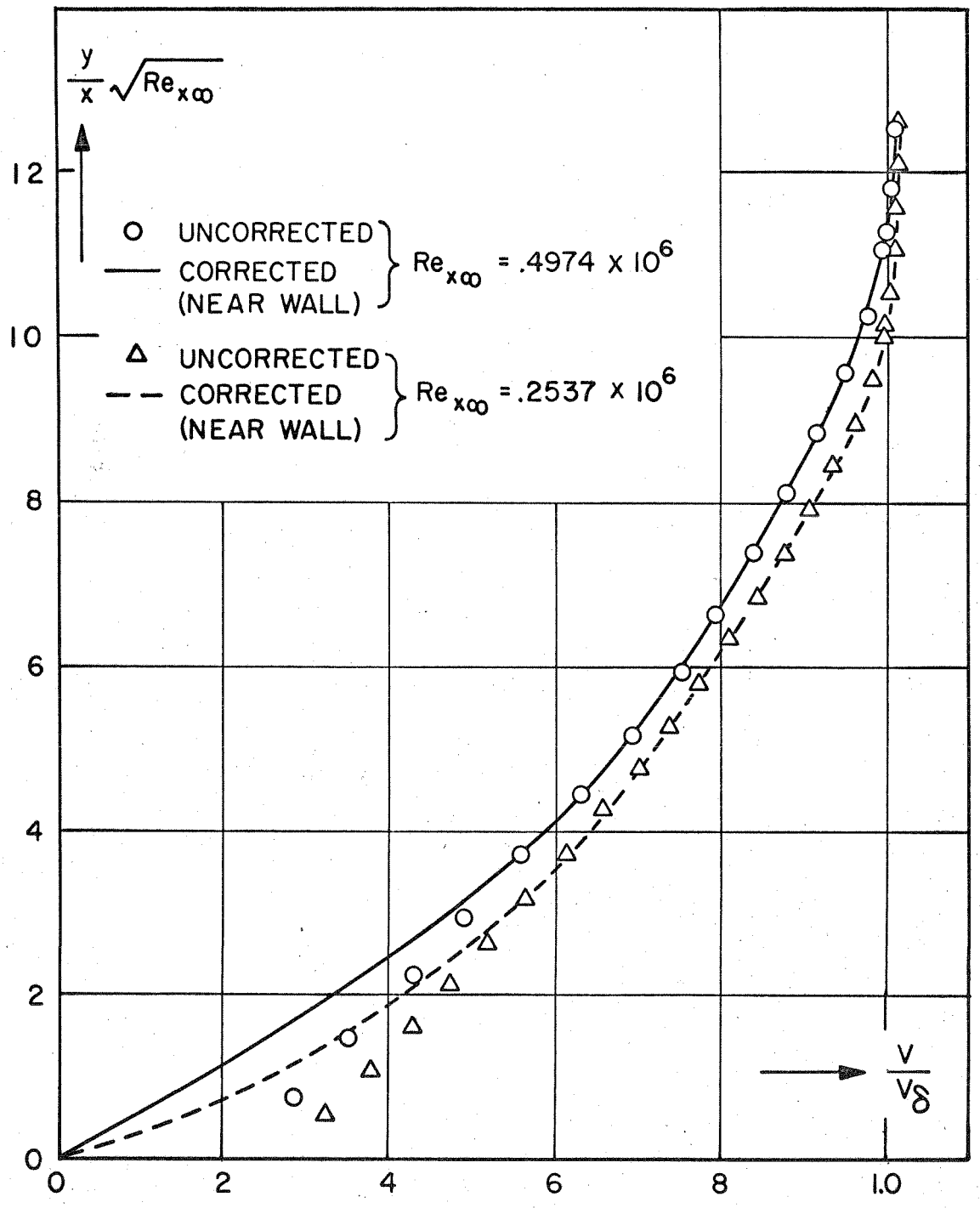

FIG. 9d. VELOCITY PROFILES AT s = .1132 IN.

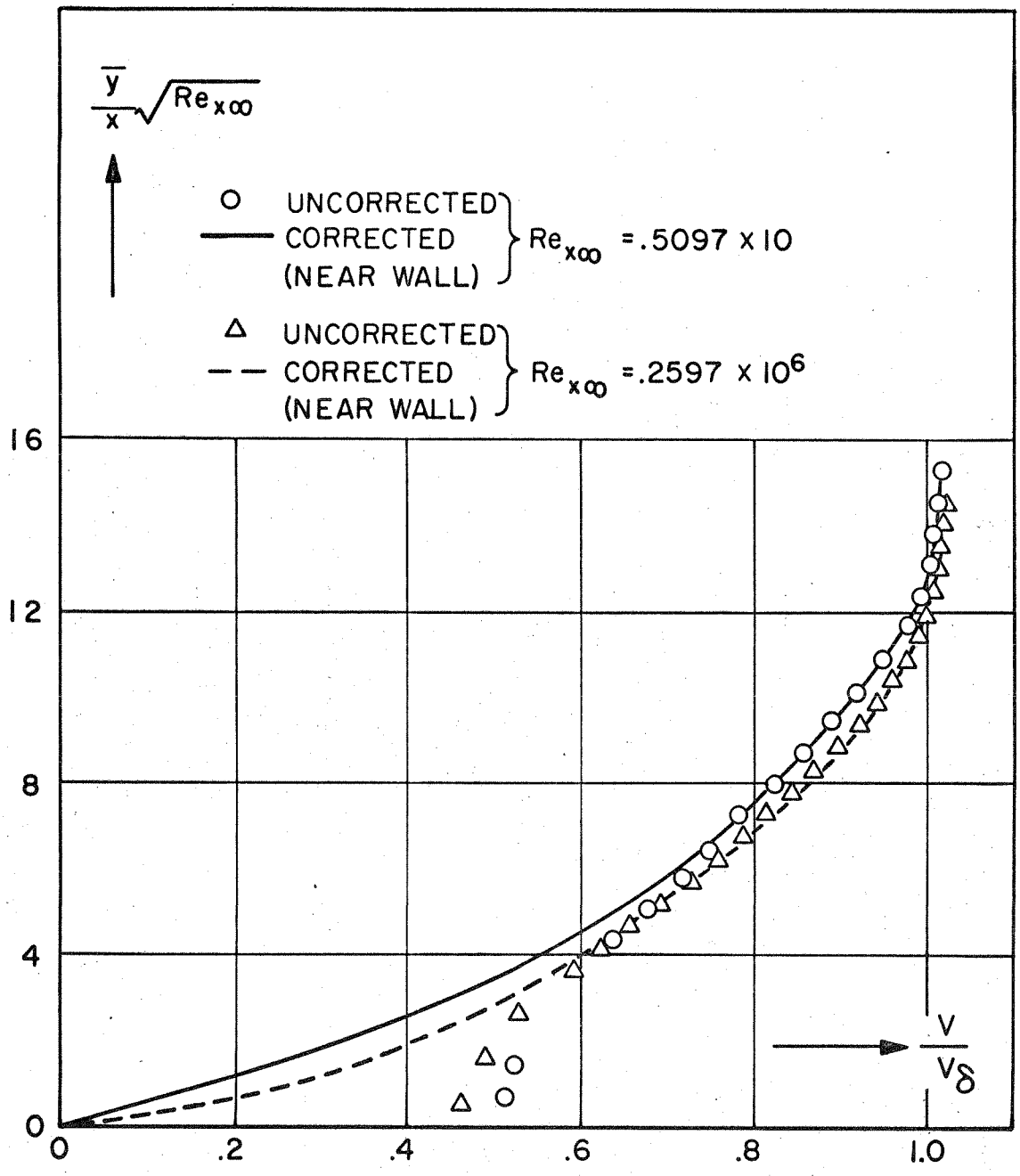

FIG. 9e. VELOCITY PROFILES AT s = .2317 IN.

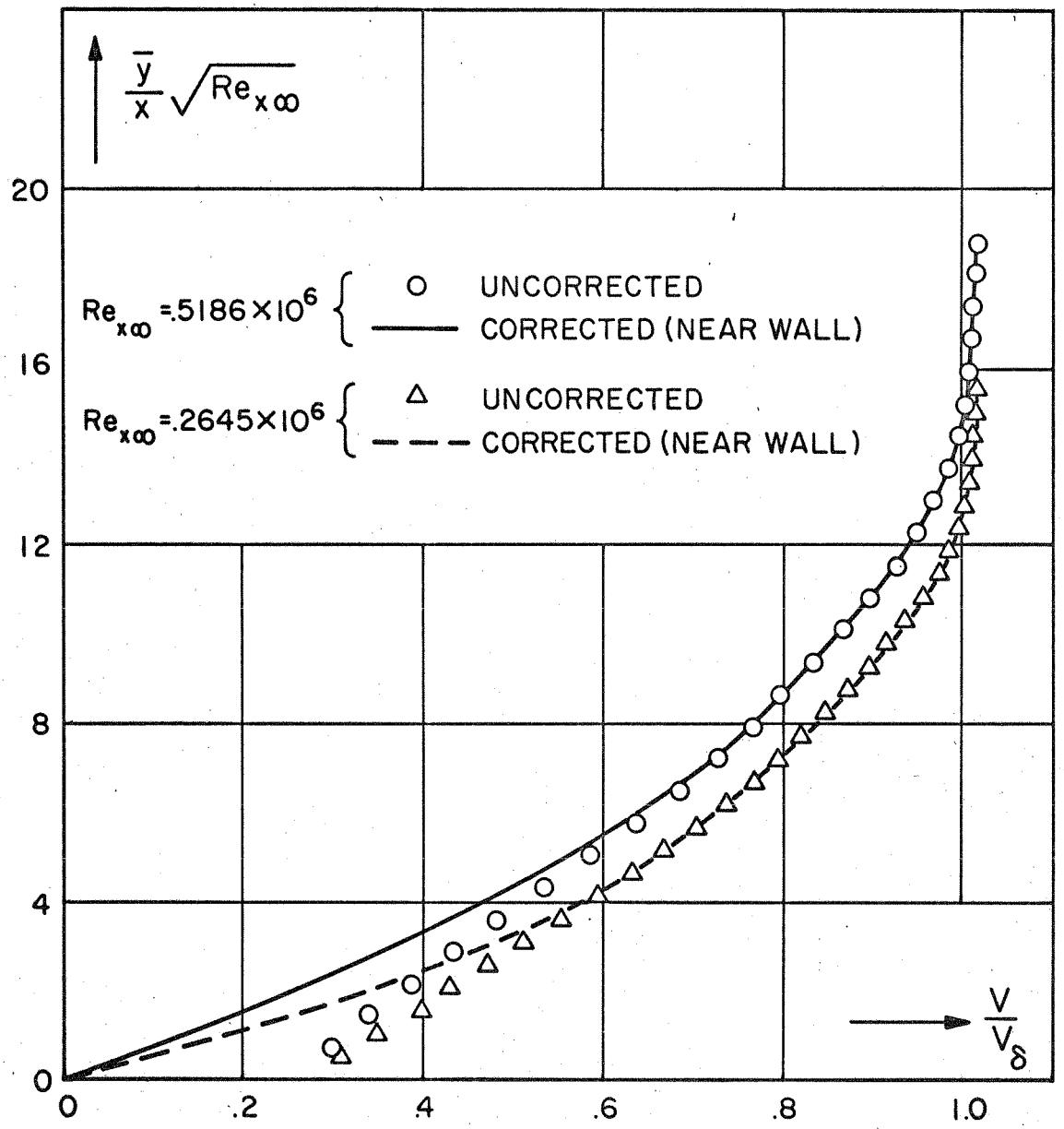

FIG. 9f. VELOCITY PROFILES AT s = .317 IN.

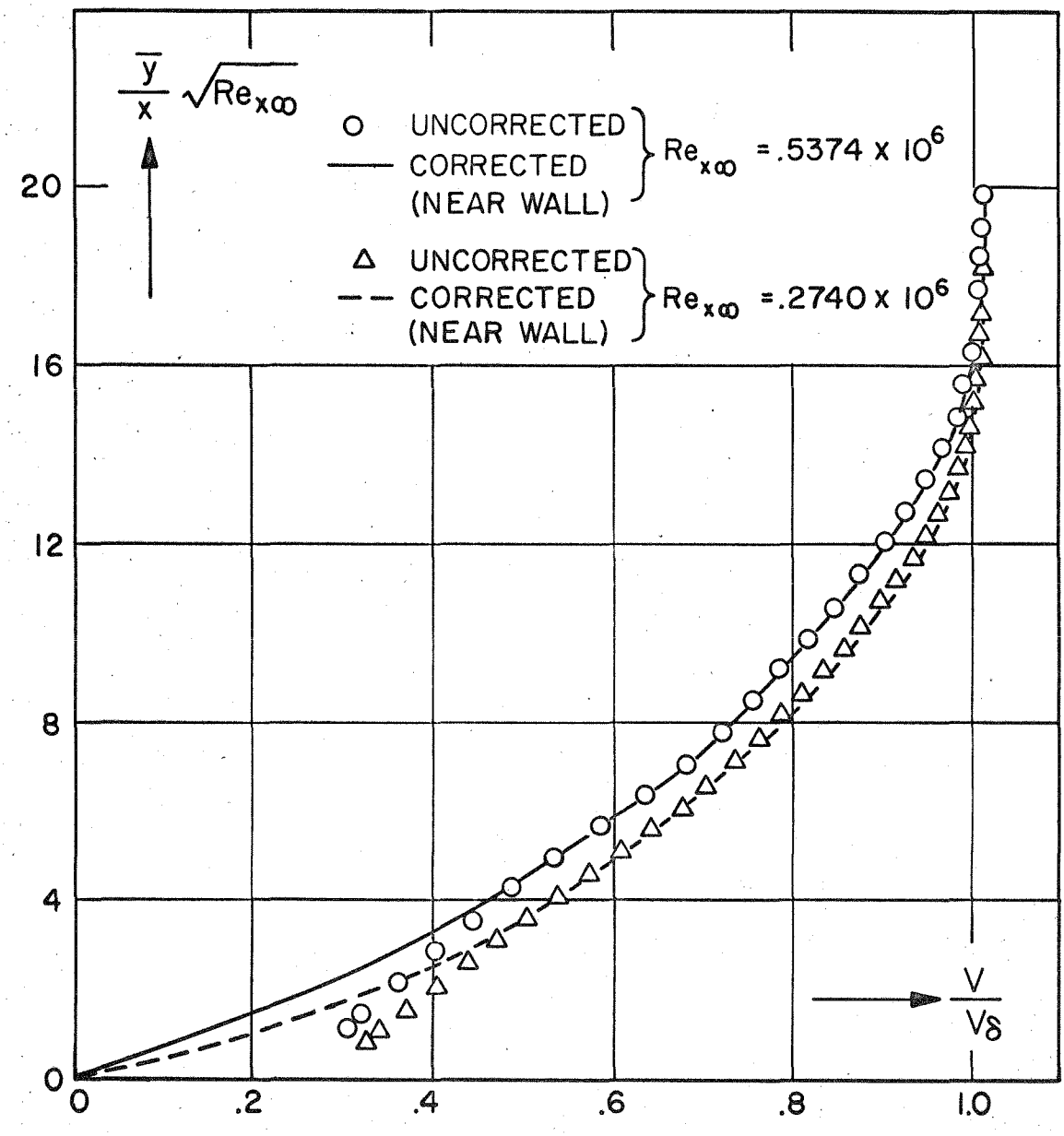

FIG. 9g. VELOCITY PROFILES AT s = .497 IN.

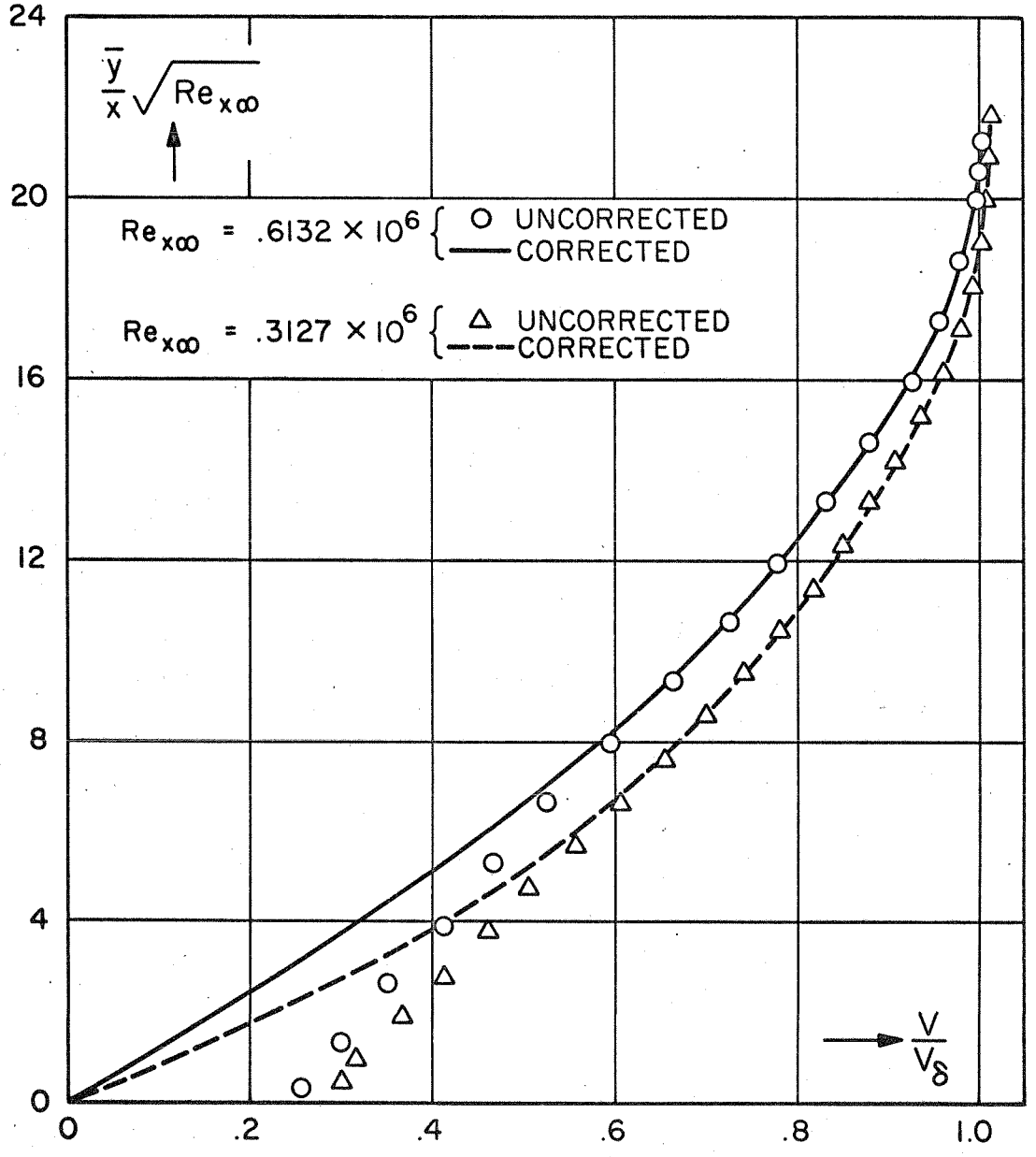

FIG.9h. VELOCITY PROFILES AT s = 1.225 IN.

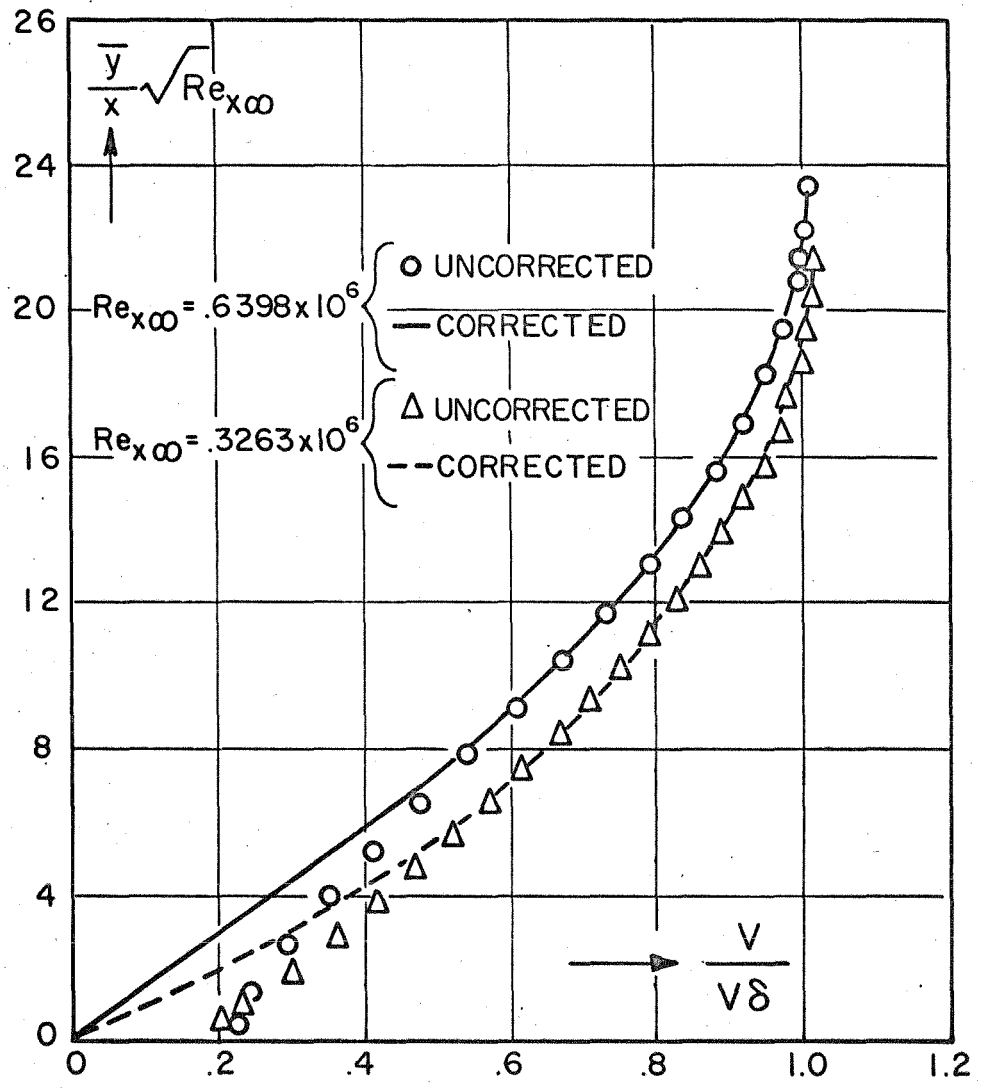

FIG. 9i. VELOCITY PROFILES AT s = 1.48 IN.

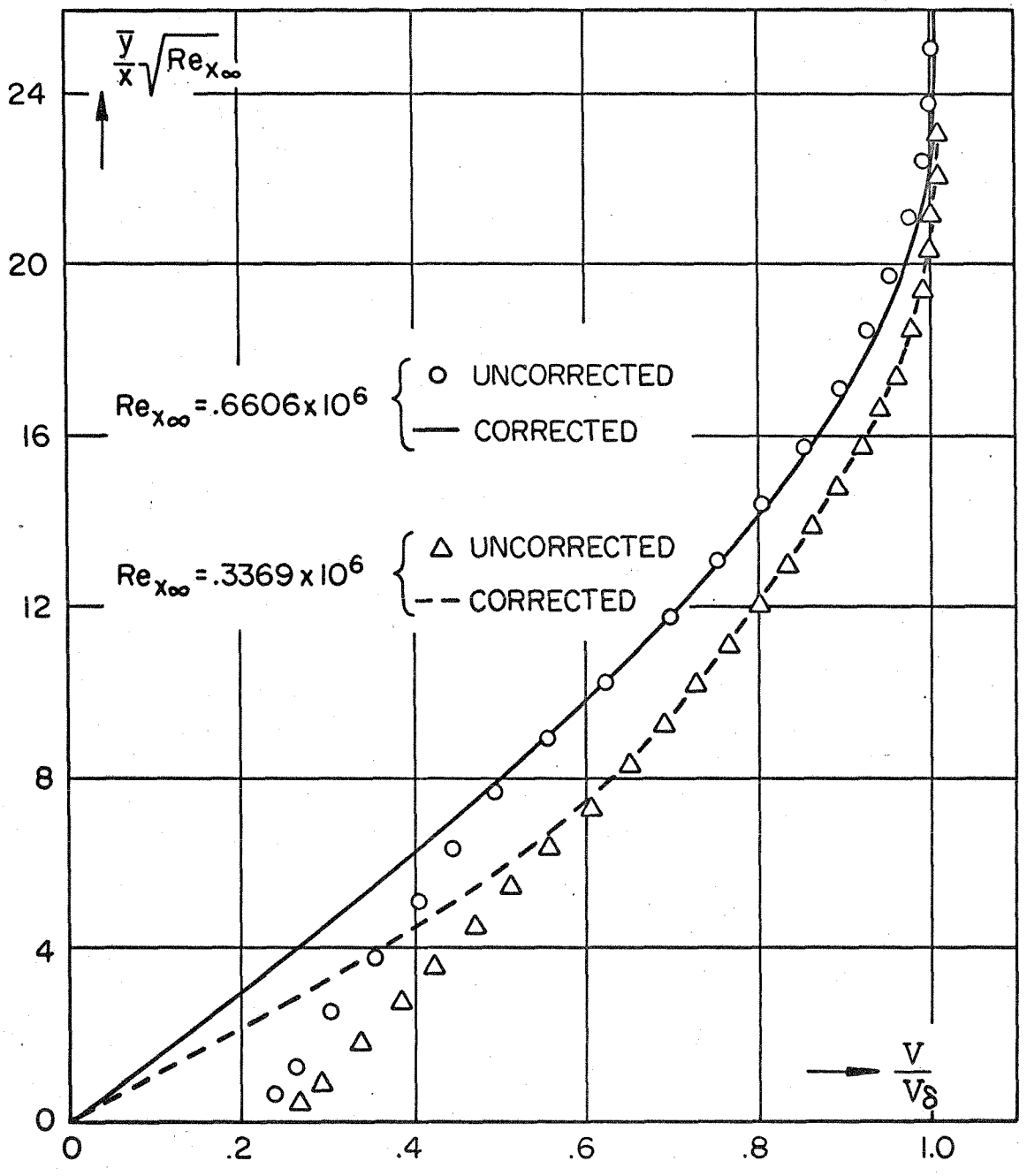

FIG. 9j VELOCITY PROFILES AT s = 1.68 IN.

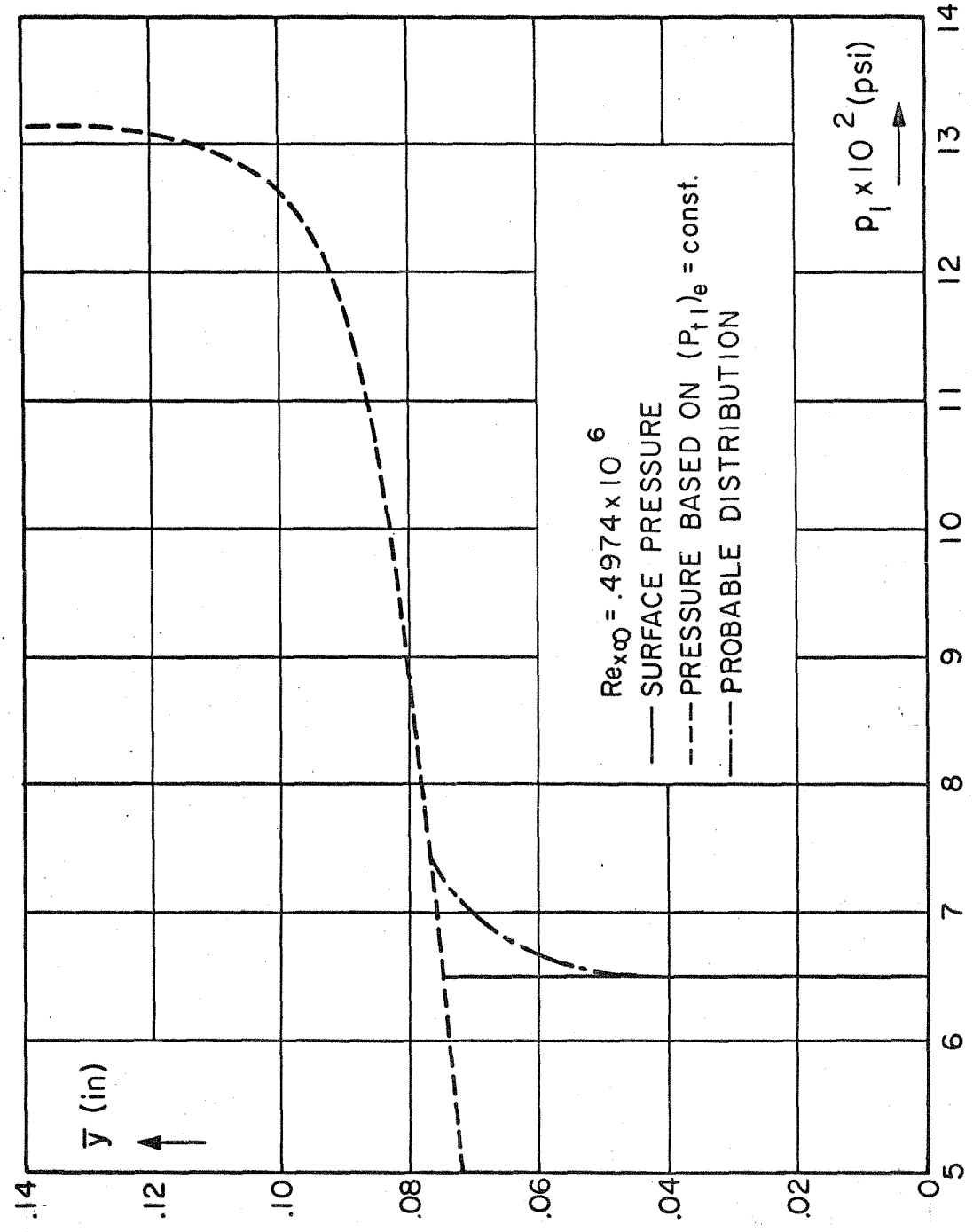

FIG. 10d_α. STATIC PRESSURE PROFILE AT s = .1132 IN.

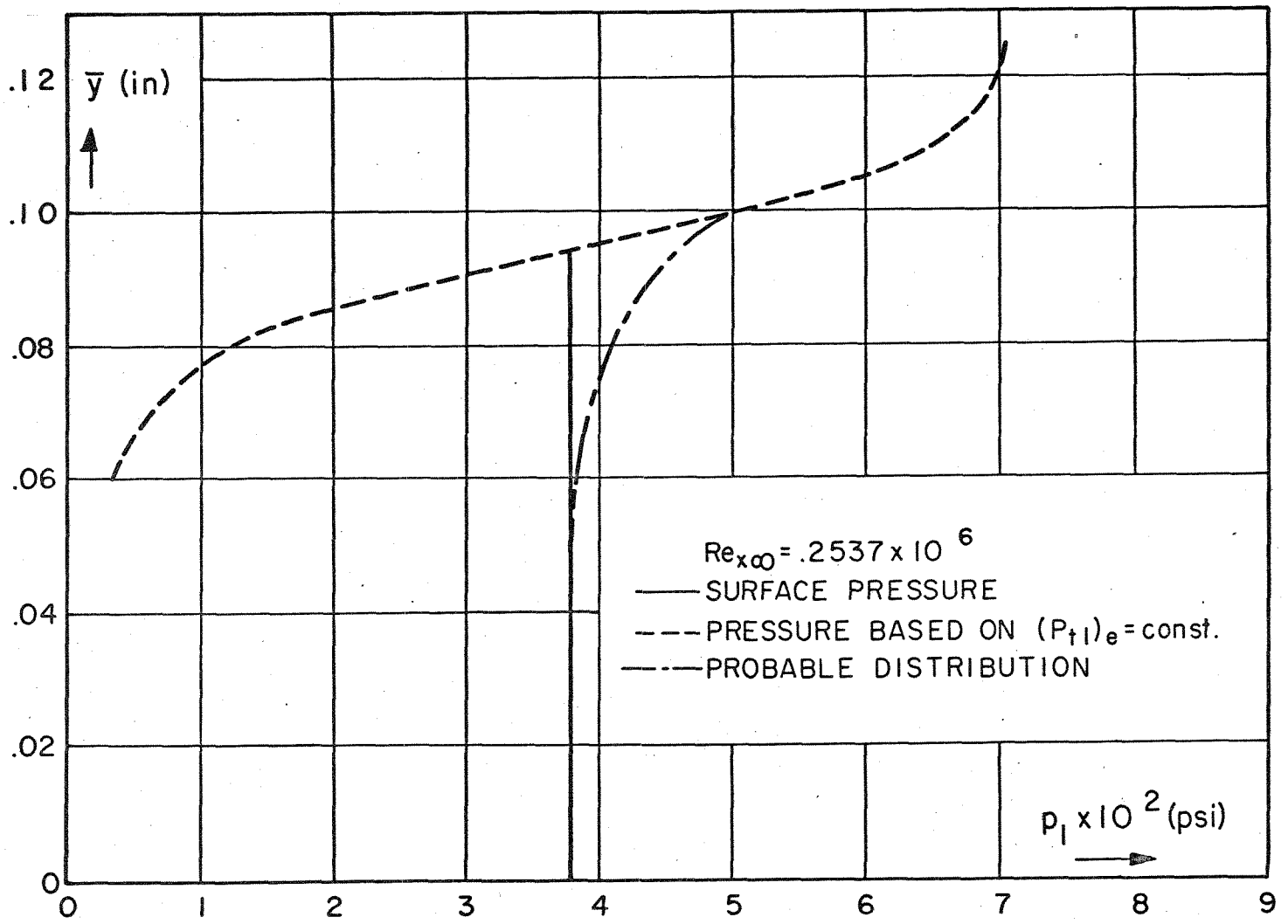

FIG. 10d_β STATIC PRESSURE PROFILE AT s = .1132 IN.

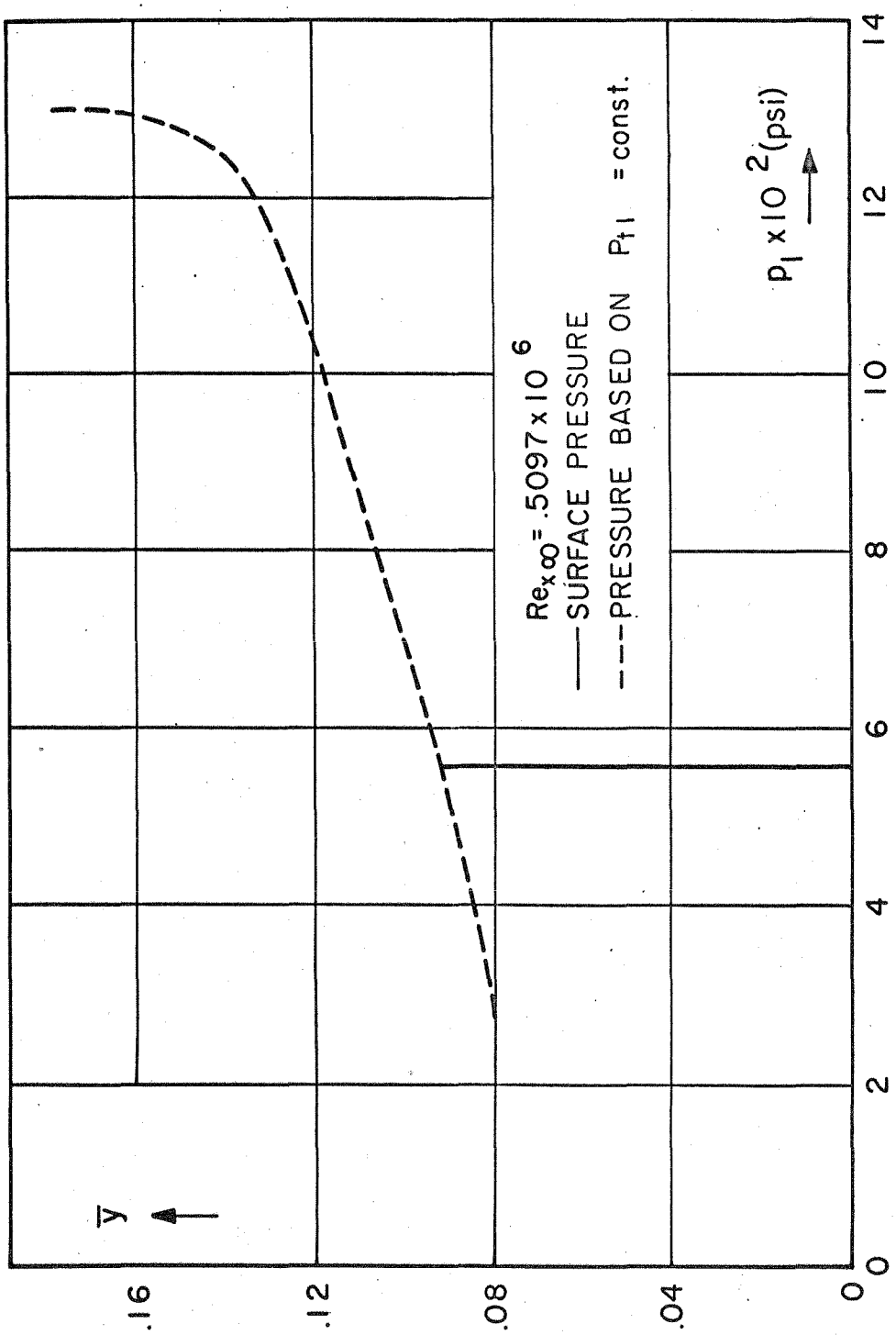

FIG. 10eα STATIC PRESSURE DISTRIBUTION AT s = .2317 IN.

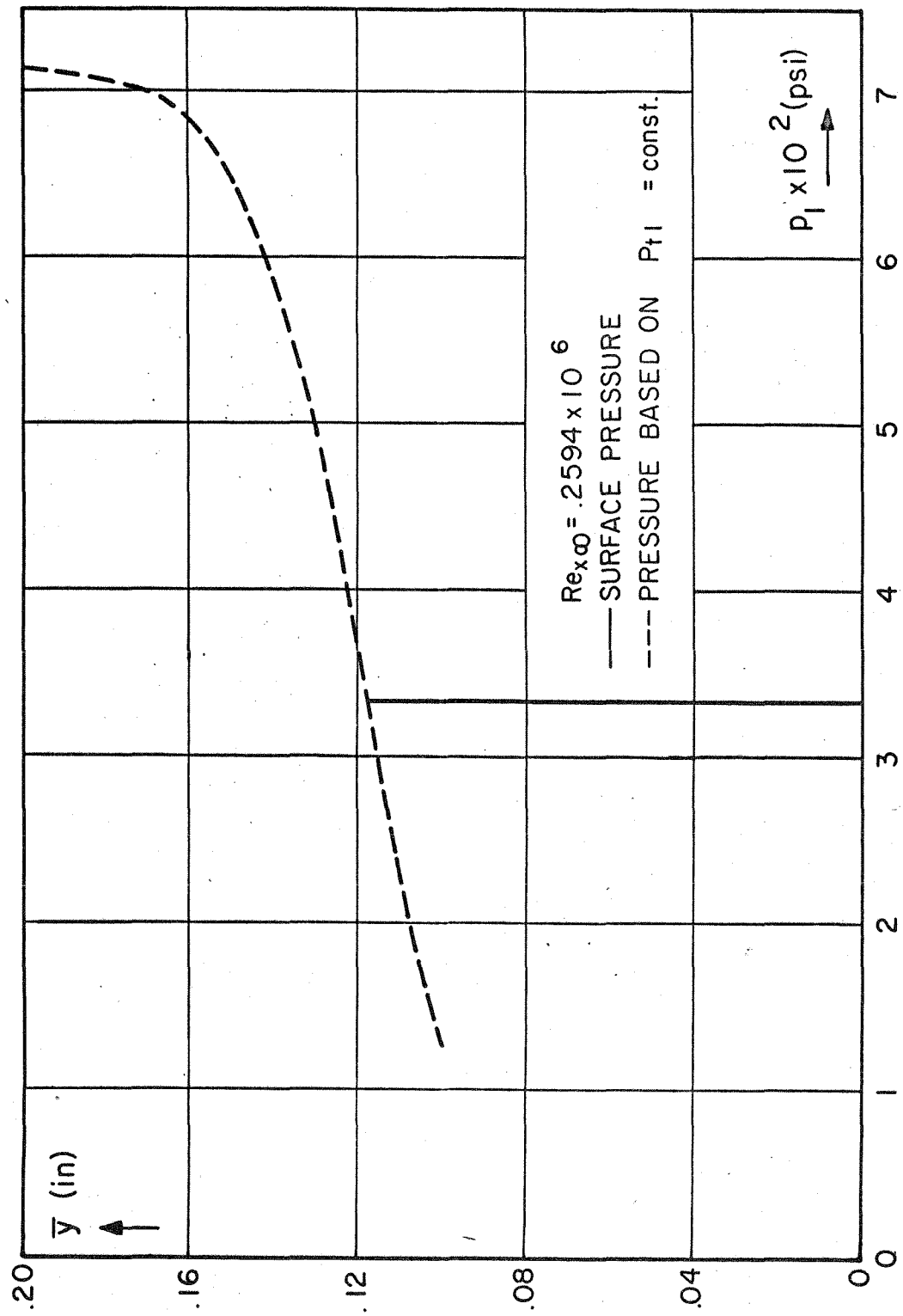

FIG. 10e$_\beta$. STATIC PRESSURE DISTRIBUTION AT s=.2317 IN.

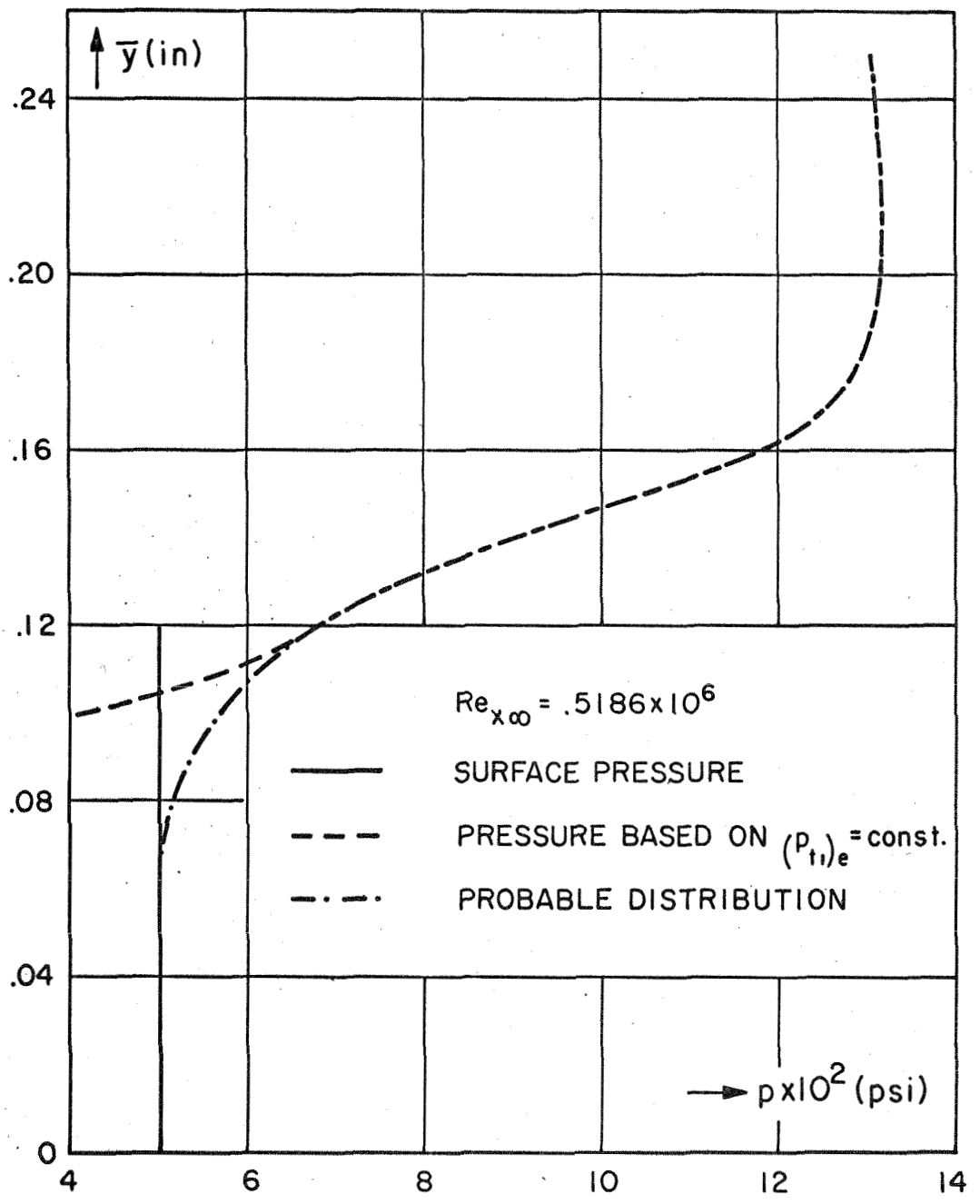

FIG. 10 f_α. STATIC PRESSURE PROFILE AT s = .317 IN.

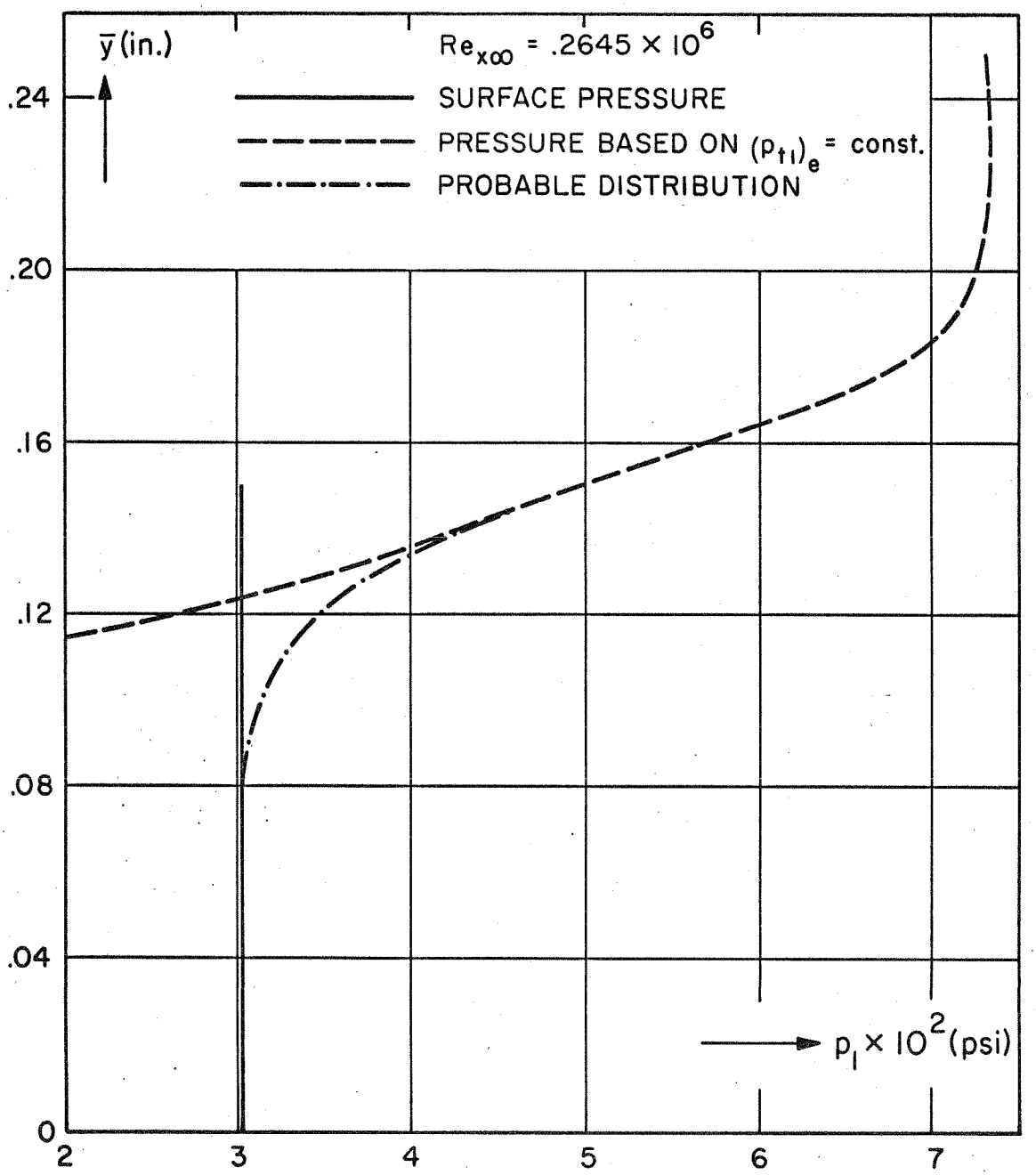

FIG. 10 f_β. STATIC PRESSURE PROFILE AT s = .317 IN.

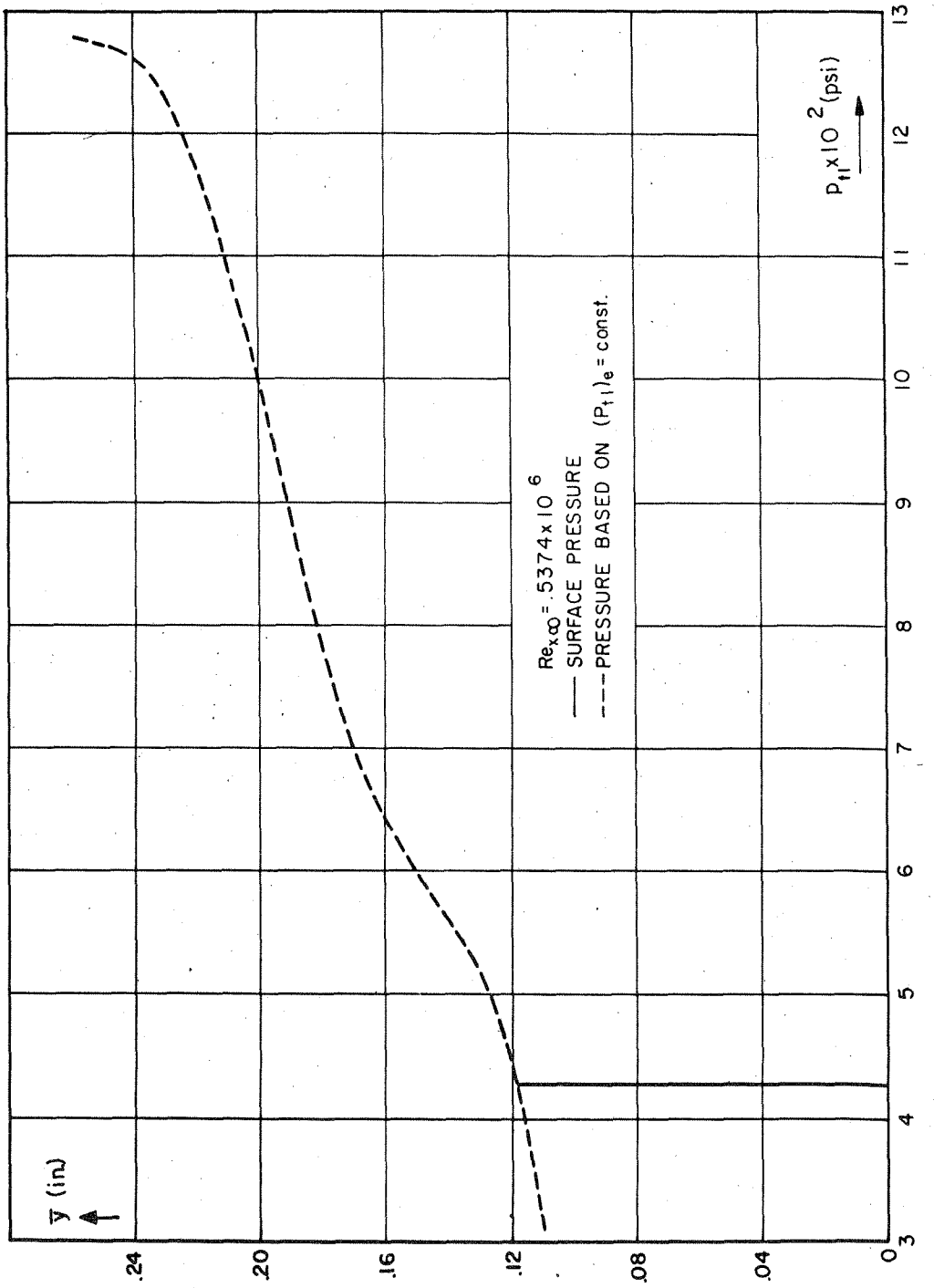

FIG. $10g_\alpha$. STATIC PRESSURE PROFILES AT s=.497 IN.

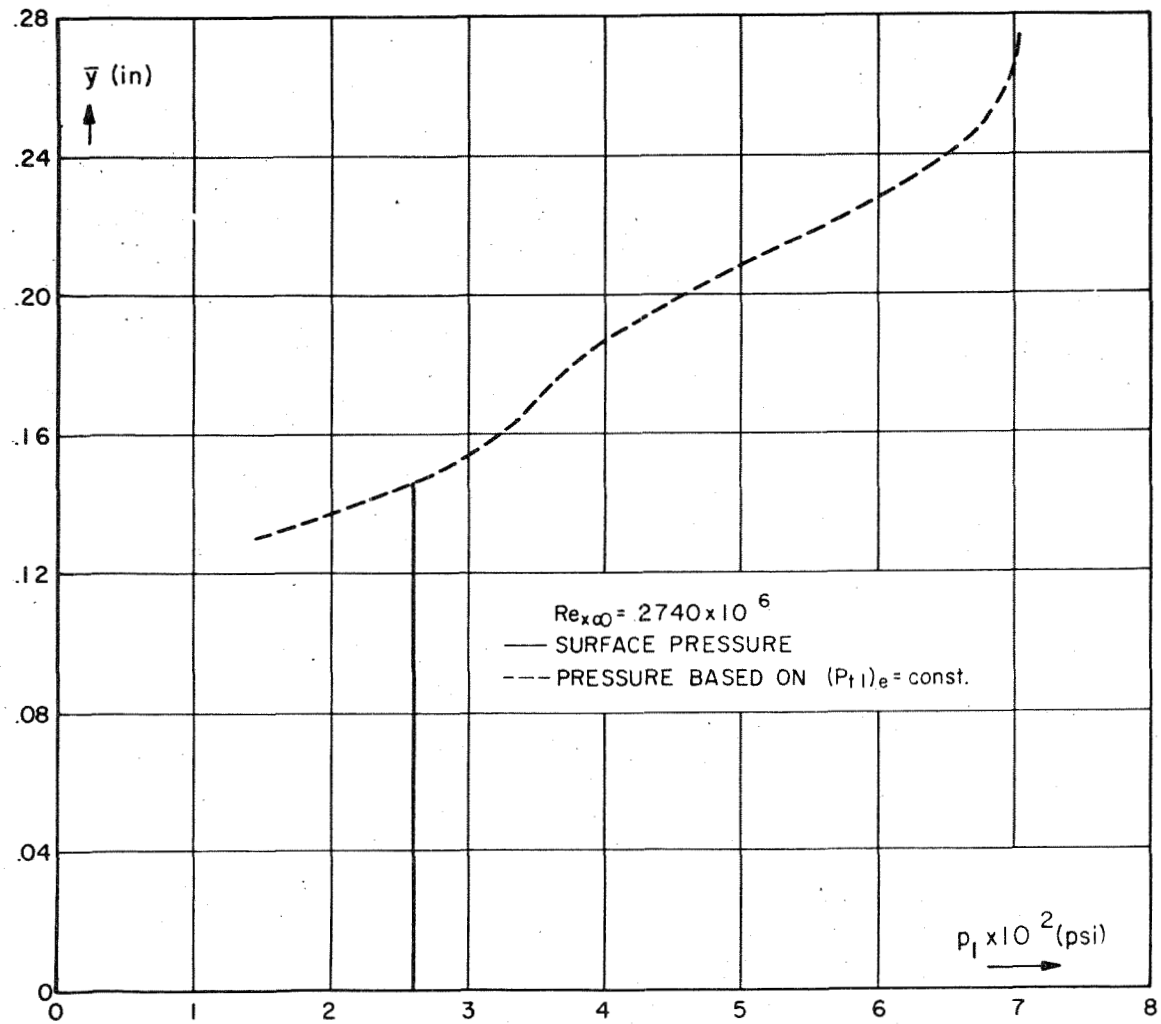

FIG. 10g$_\beta$. STATIC PRESSURE PROFILES AT s = 497 IN.

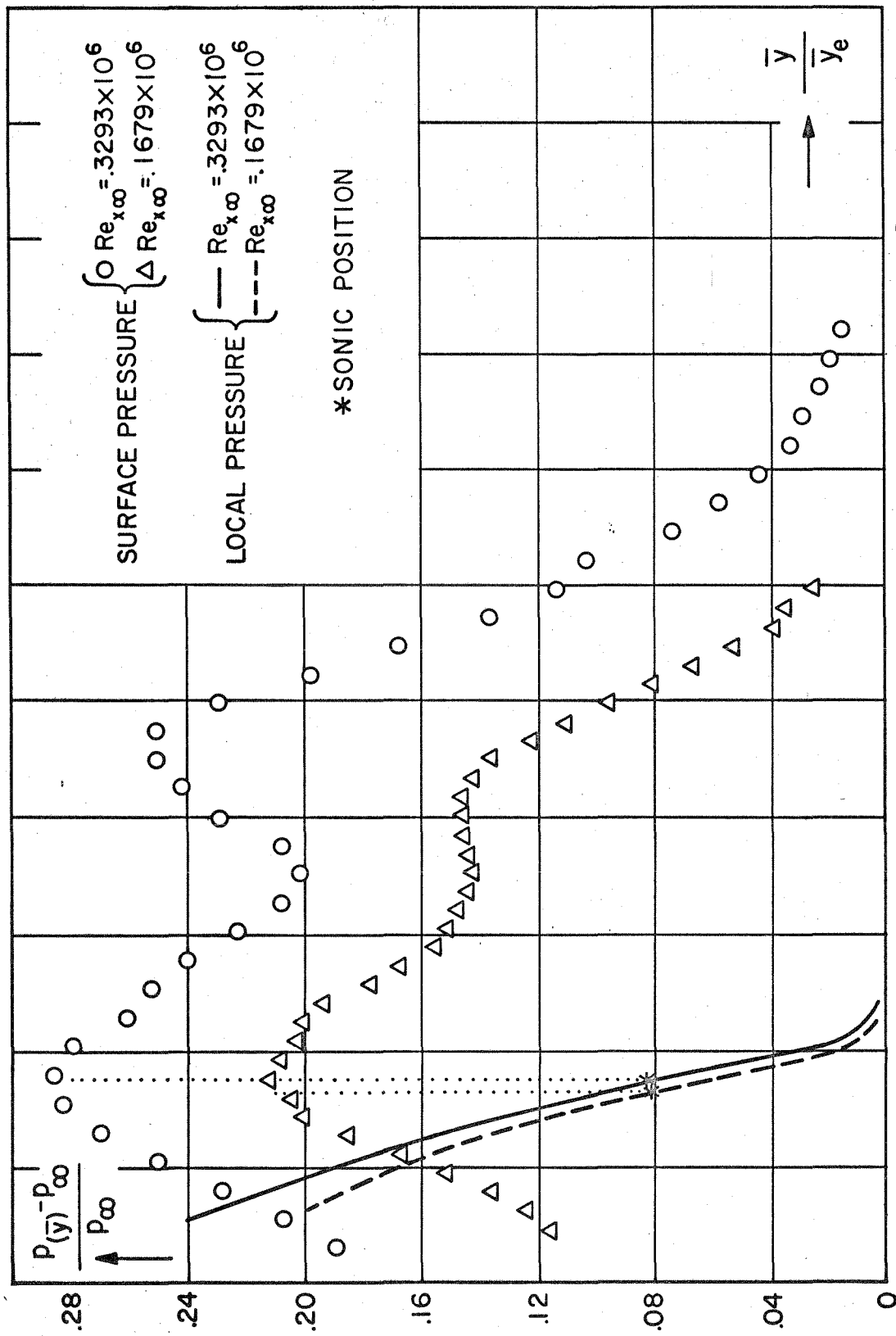

FIG. 11. STATIC PRESSURE VARIATION DUE TO PROBE-BODY INTERFERENCE AT $\bar{s}$ = 1.5 IN.

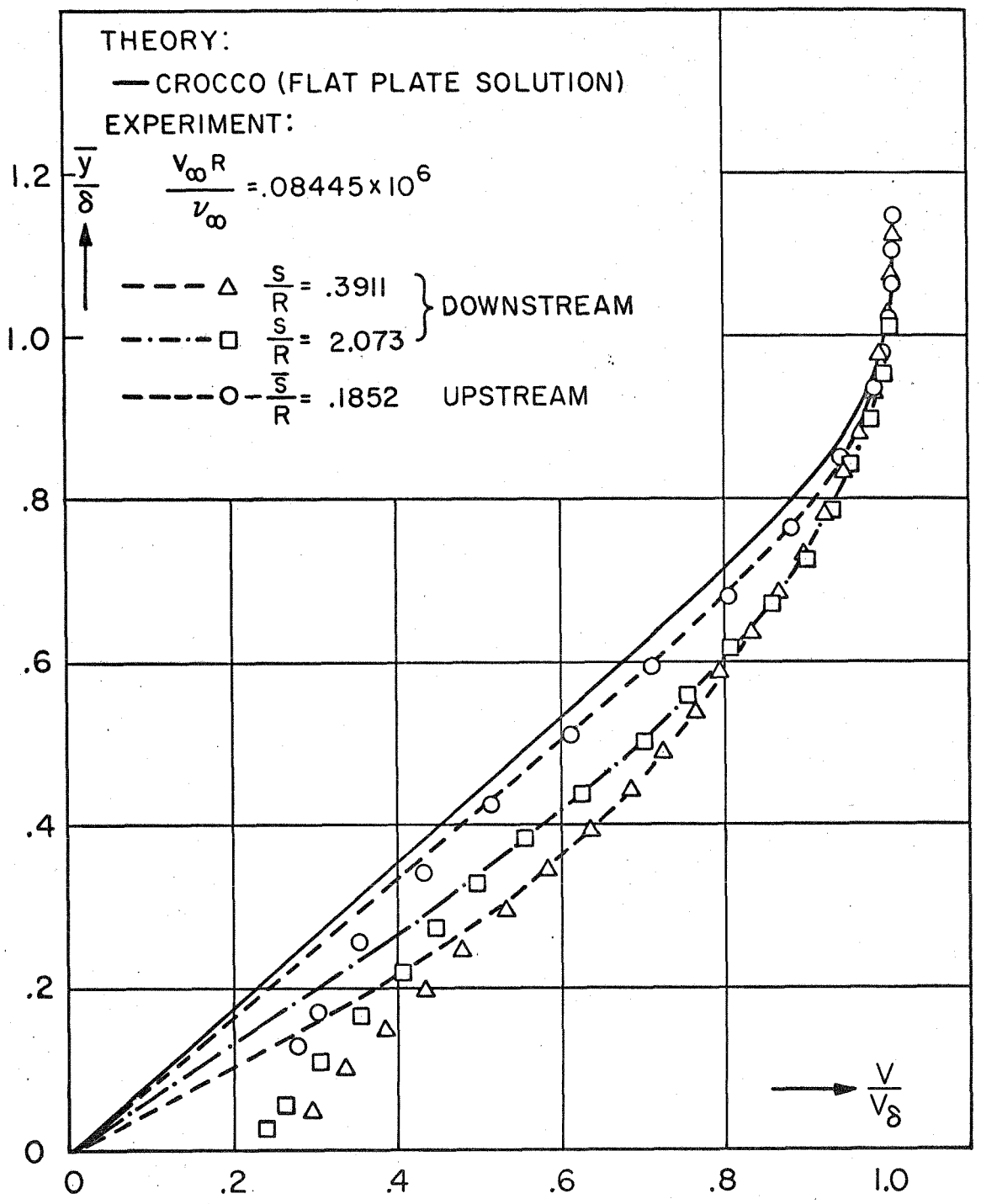

FIG. 12a. BOUNDARY LAYER VELOCITY PROFILES NEAR SHARP CONE - CYLINDER JUNCTURE AT $M_\infty = 7.87$

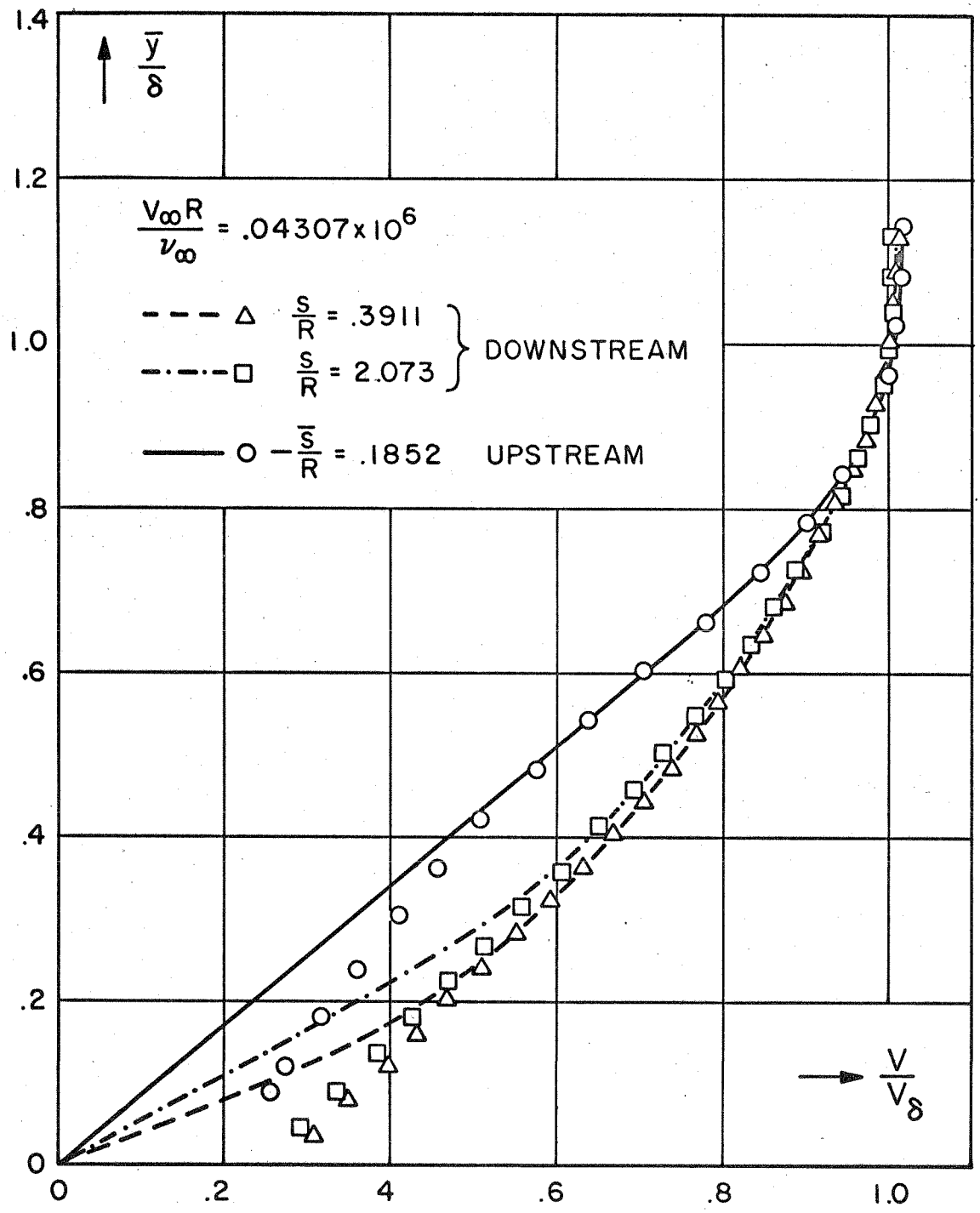

FIG. 12β. BOUNDARY LAYER VELOCITY PROFILES NEAR SHARP CONE-CYLINDER JUNCTURE AT $M_\infty = 7.81$

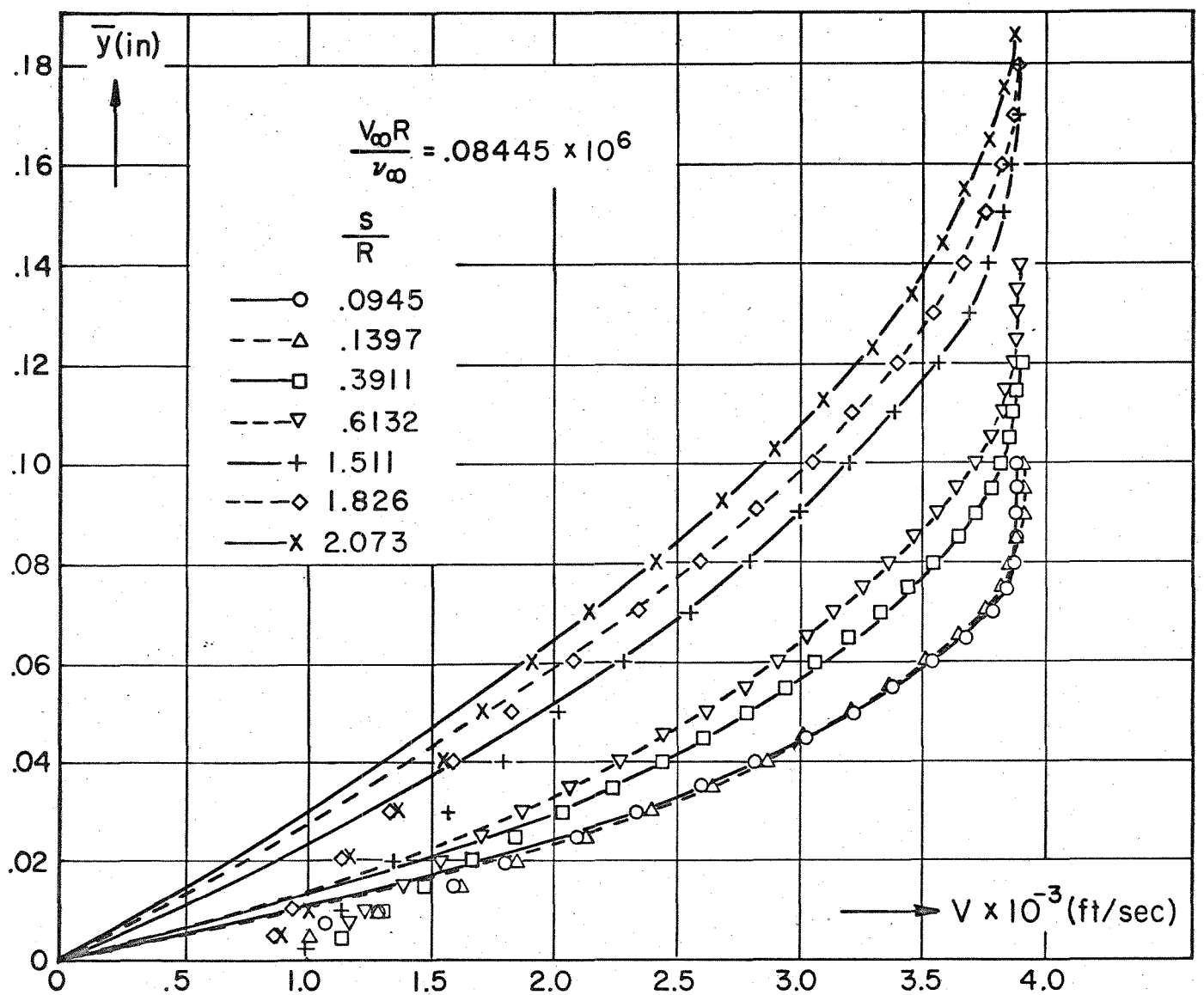

FIG. 13α. BOUNDARY LAYER VELOCITY PROFILES DOWNSTREAM OF SHARP CONE-CYLINDER JUNCTURE AT $M_\infty = 7.87$

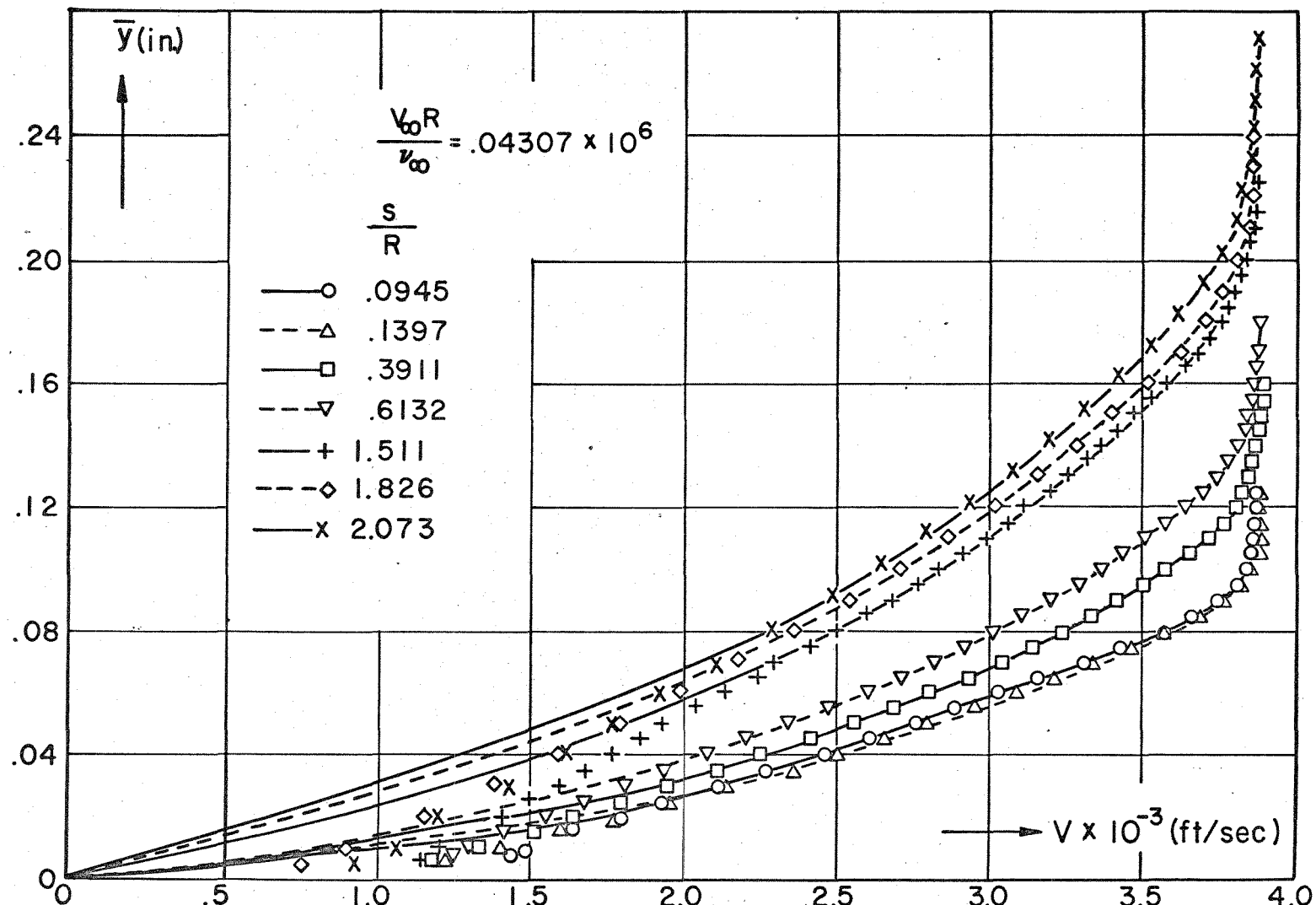

FIG. 13β. BOUNDARY LAYER VELOCITY PROFILES DOWNSTREAM OF SHARP CONE-CYLINDER JUNCTURE AT $M_\infty = 7.81$

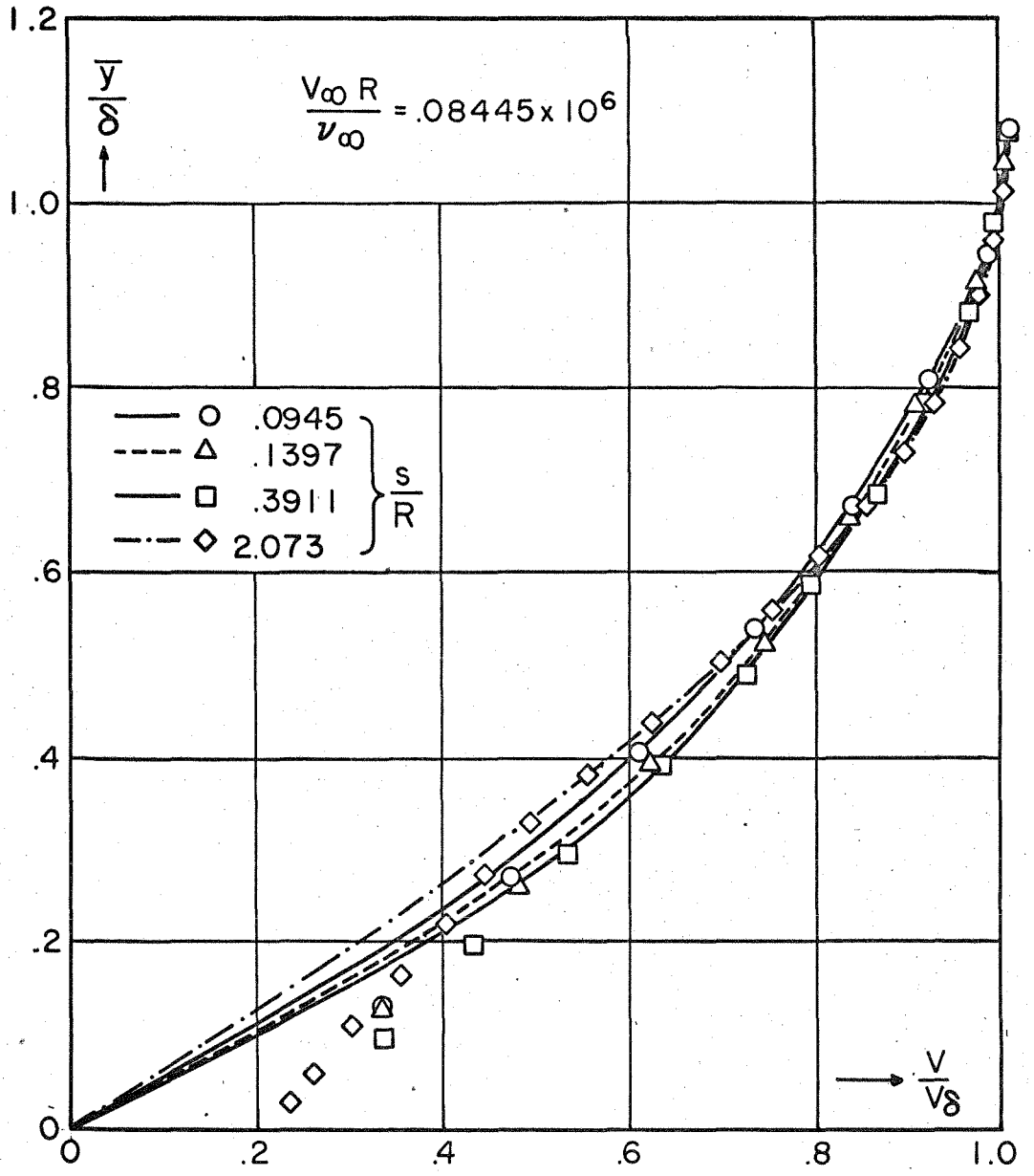

FIG. 14a. BOUNDARY LAYER VELOCITY PROFILES DOWNSTREAM OF SHARP CONE-CYLINDER JUNCTURE AT $M_\infty = 7.87$

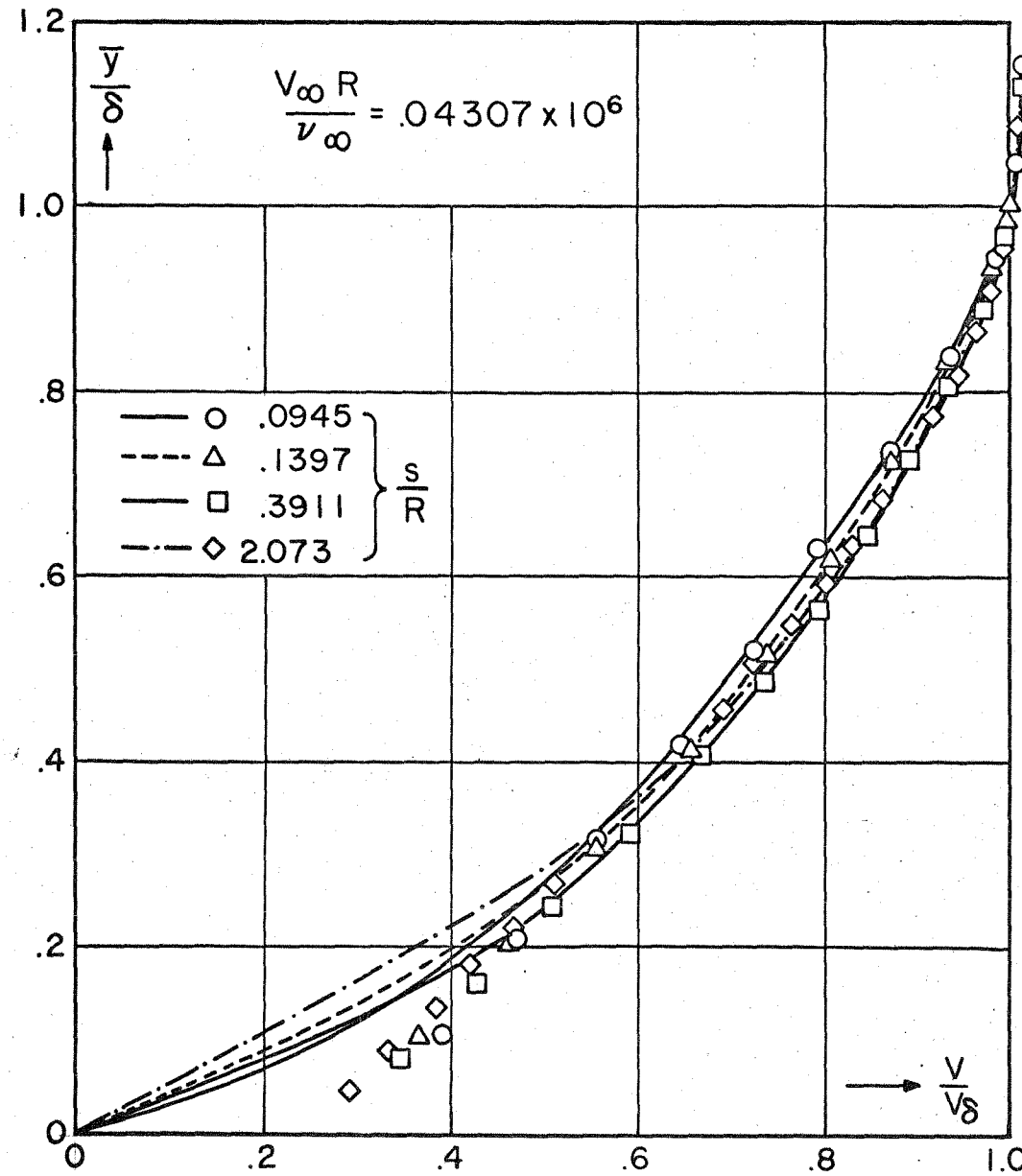

FIG. 14 β. BOUNDARY LAYER VELOCITY PROFILES DOWNSTREAM OF SHARP CONE-CYLINDER JUNCTURE AT $M_\infty = 7.81$

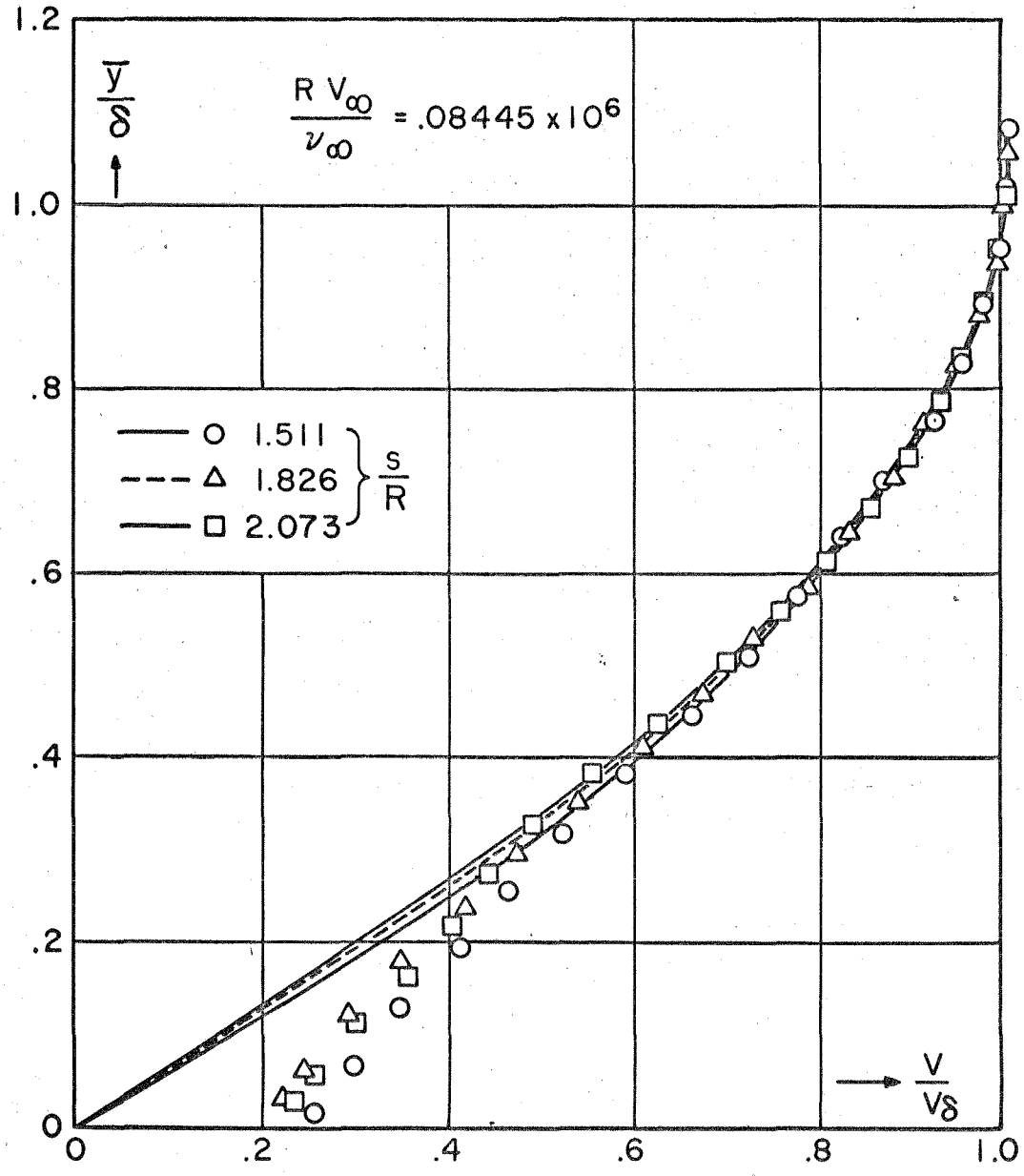

FIG. 15a. VELOCITY PROFILES "FAR" DOWNSTREAM OF SHARP CORNER AT $M_\infty = 7.87$

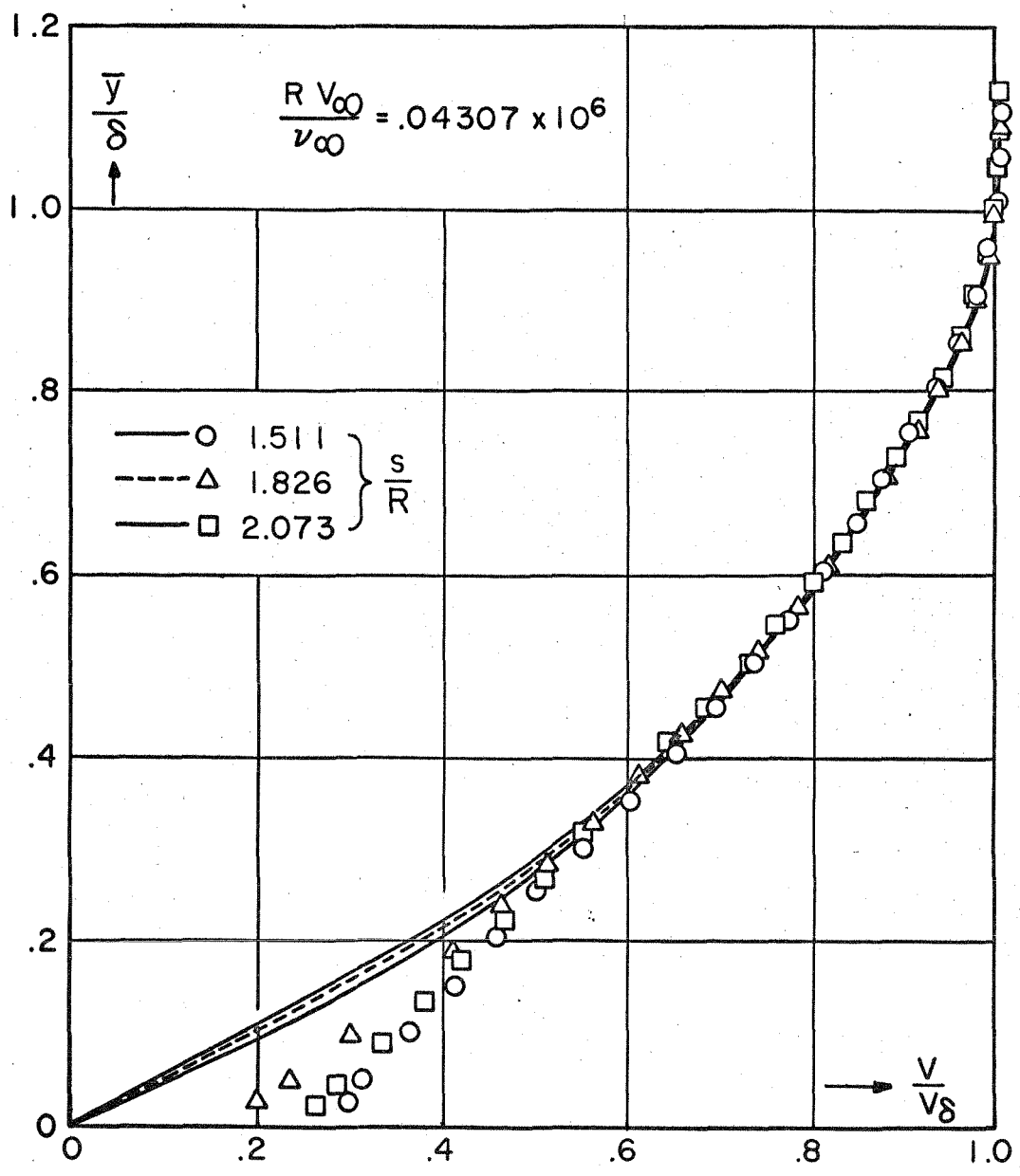

FIG. 15β. VELOCITY PROFILES "FAR" DOWNSTREAM OF SHARP CORNER AT $M_\infty = 7.81$

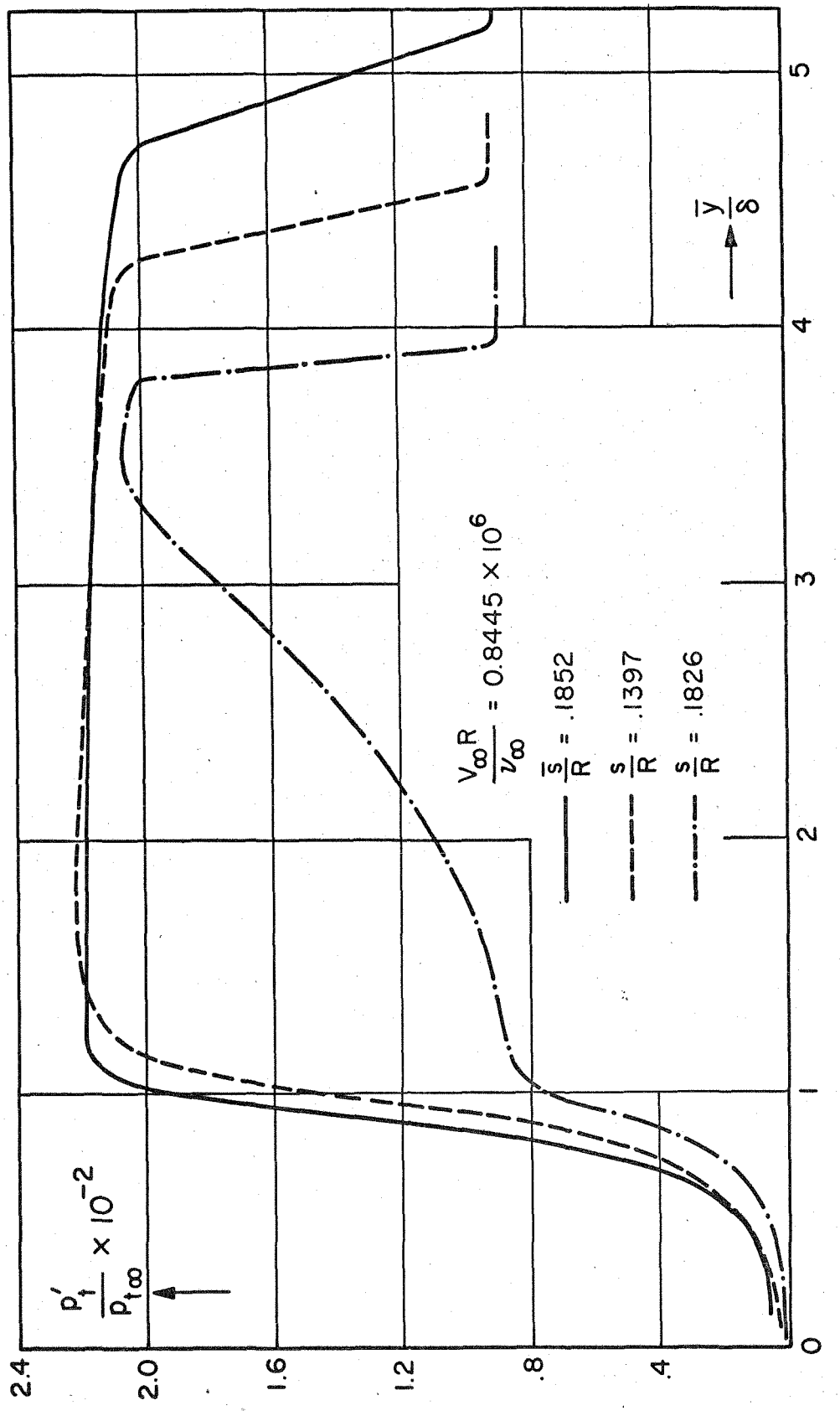

FIG. 16. TOTAL HEAD PROFILES UPSTREAM AND DOWNSTREAM OF SHARP CORNER AT $M_\infty = 7.87$

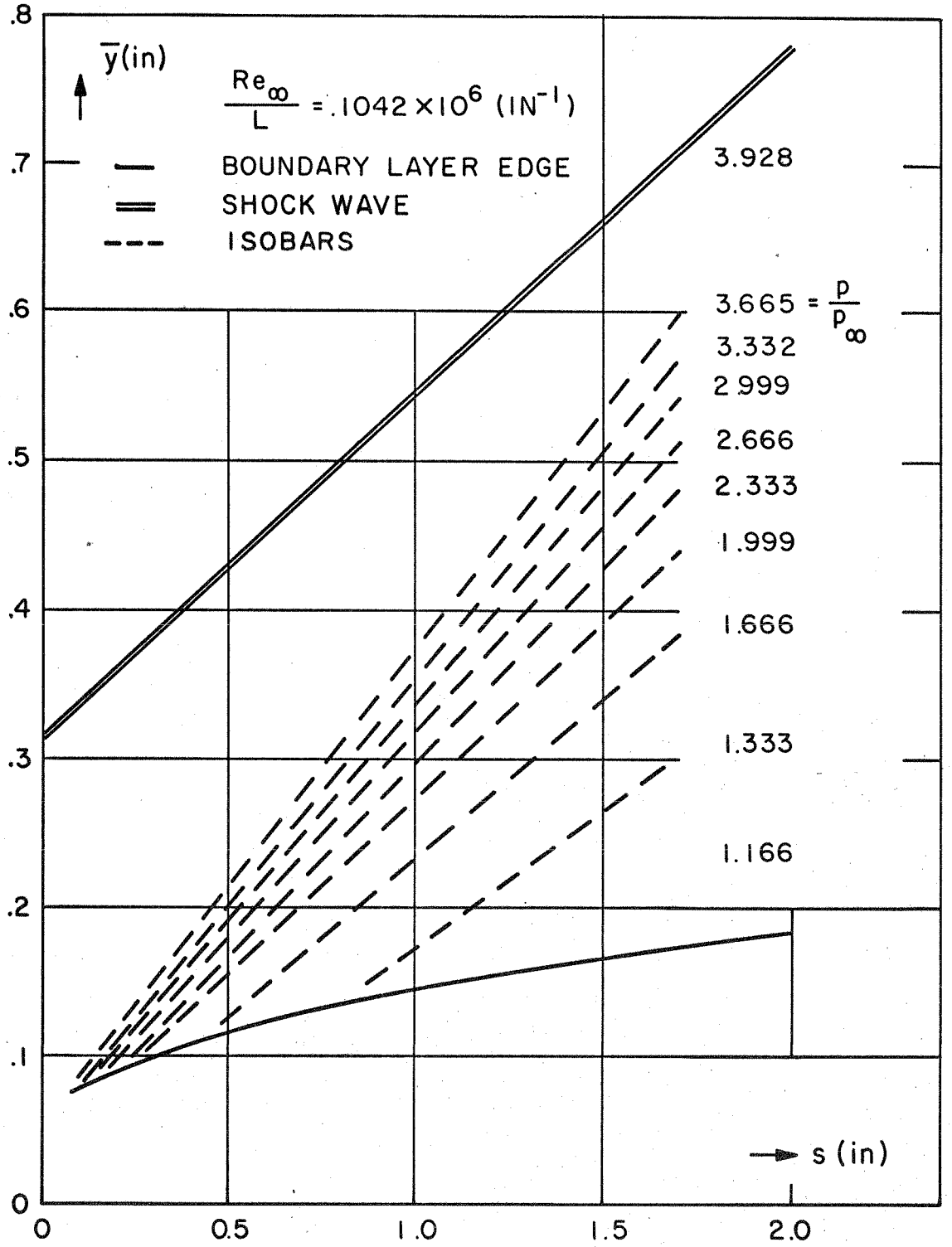

FIG. 17α. FLOW DOWNSTREAM OF SHARP CONE-CYLINDER JUNCTURE AT $M_\infty = 7.87$

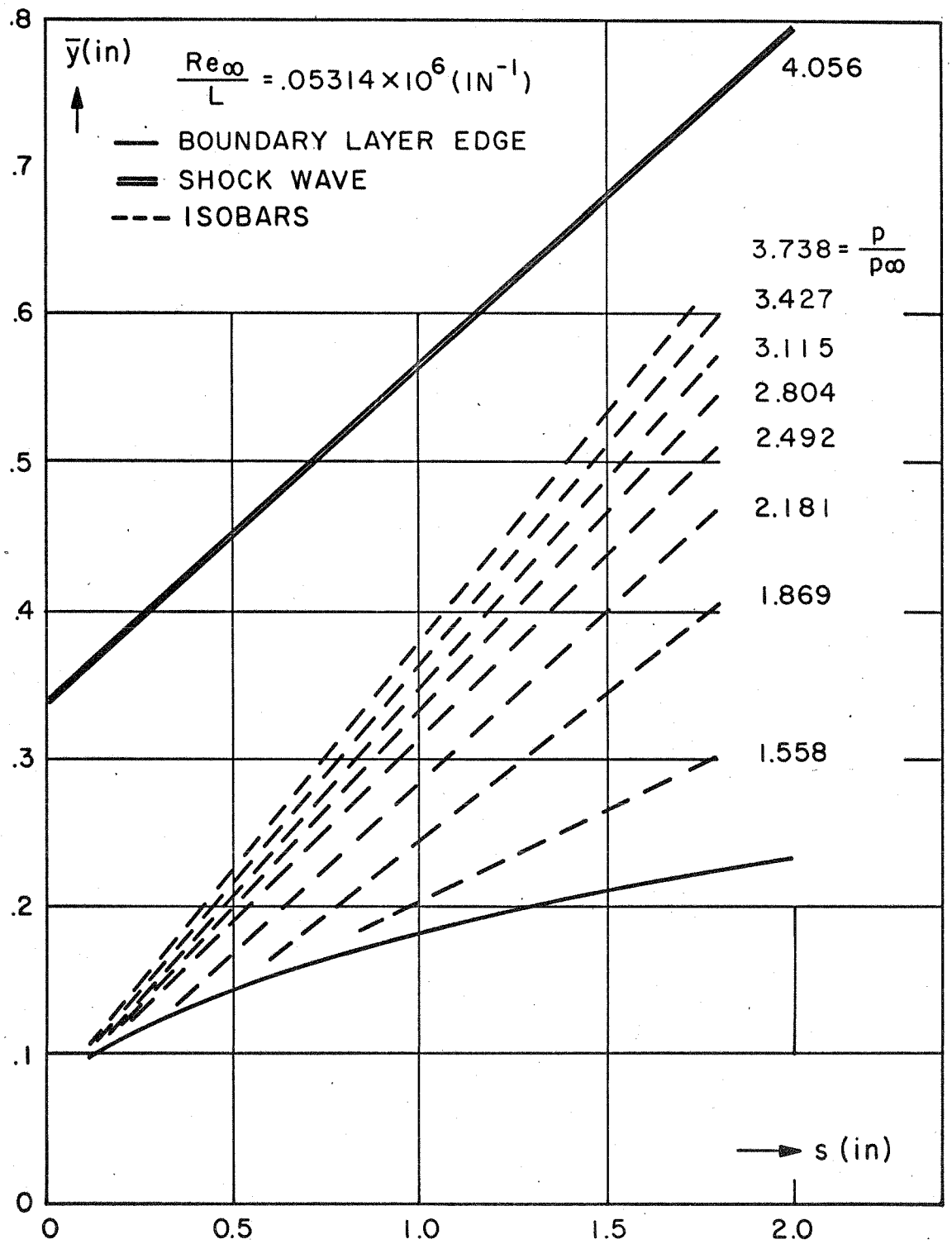

FIG. 17β. FLOW DOWNSTREAM OF SHARP CONE–CYLINDER JUNCTURE AT $M_\infty = 7.81$

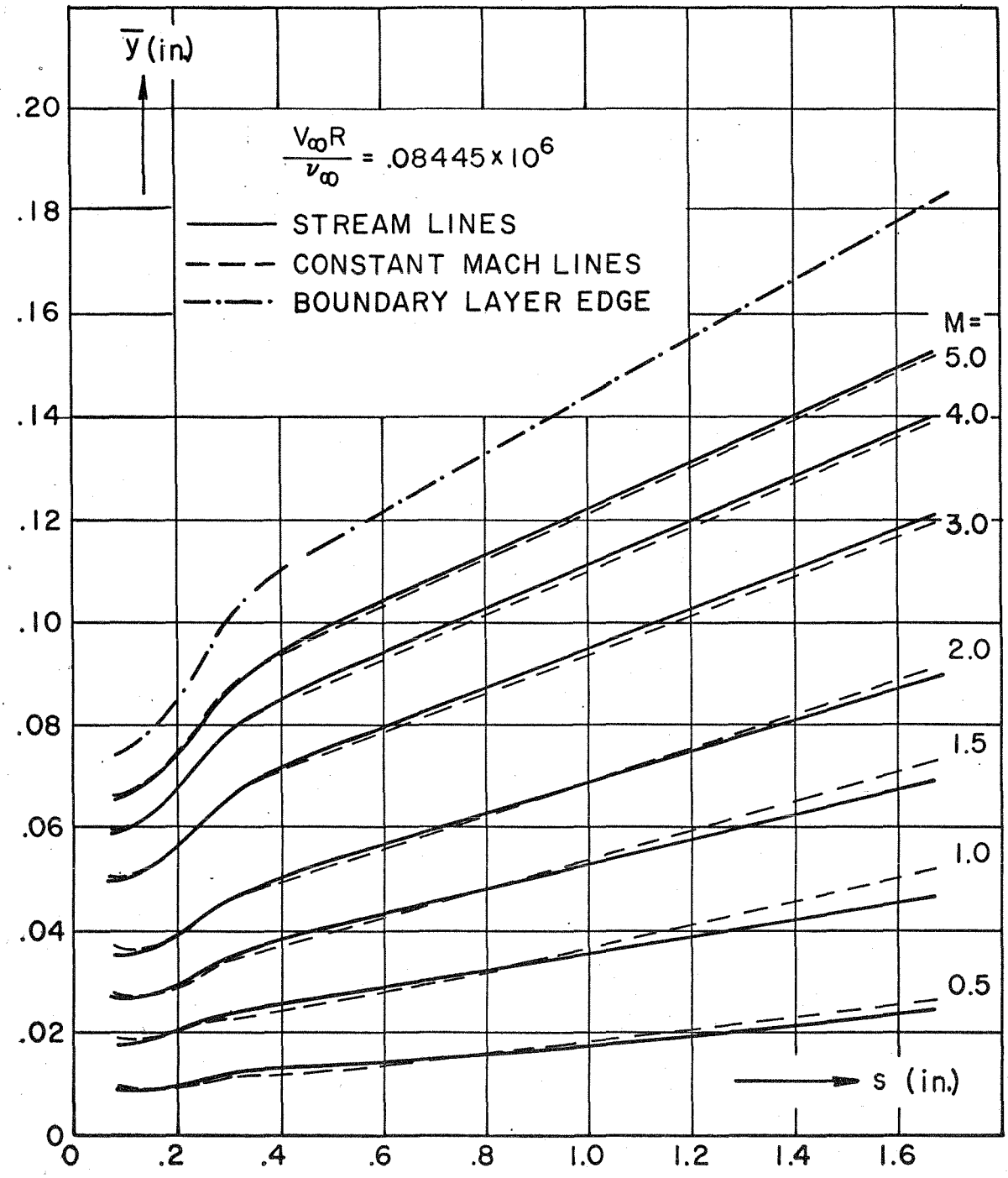

FIG. 18a. FLOW DOWNSTREAM OF SHARP CONE-CYLINDER JUNCTURE AT $M_\infty = 7.87$

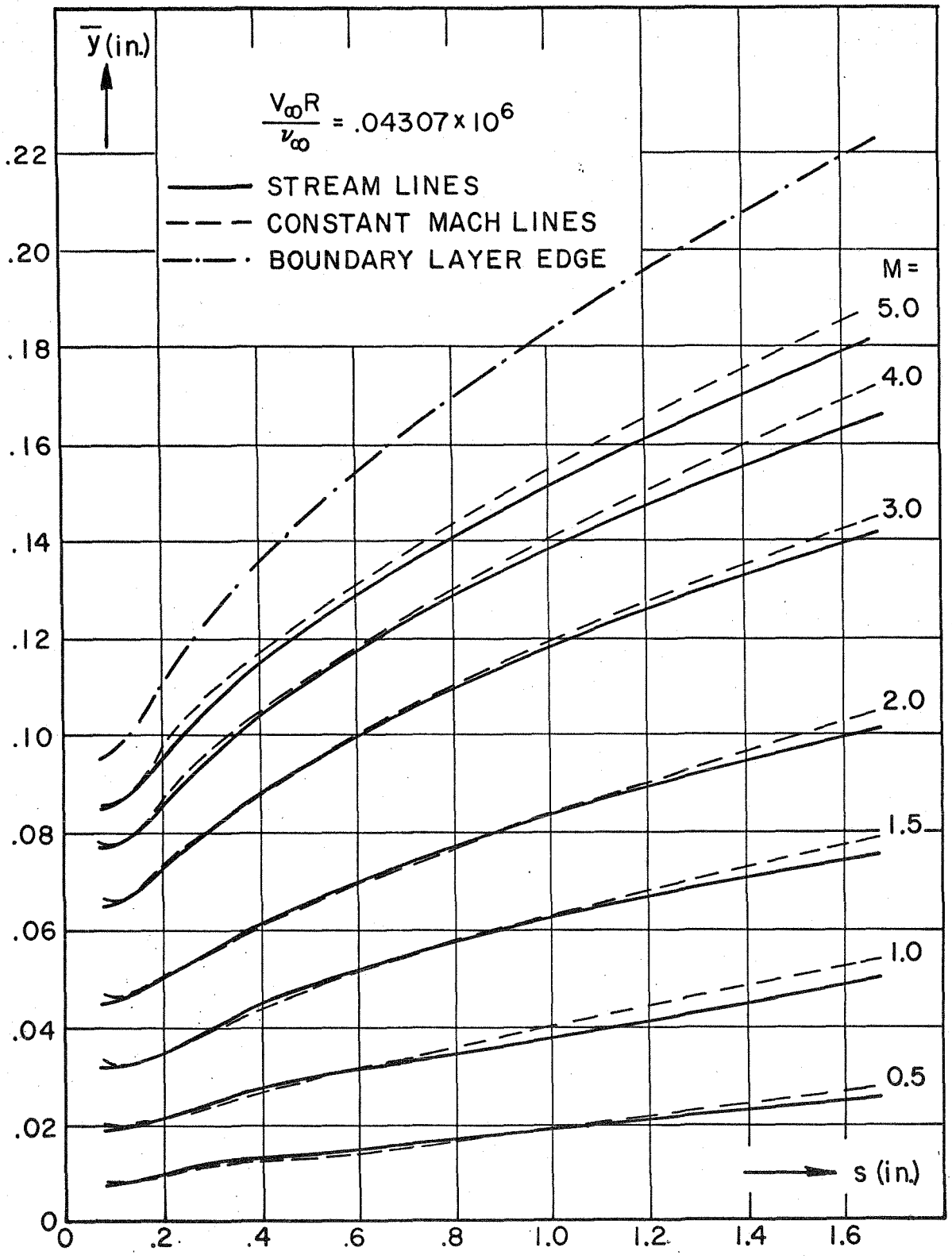

FIG. 18β. FLOW DOWNSTREAM OF SHARP CONE–CYLINDER JUNCTURE AT $M_\infty = 7.81$

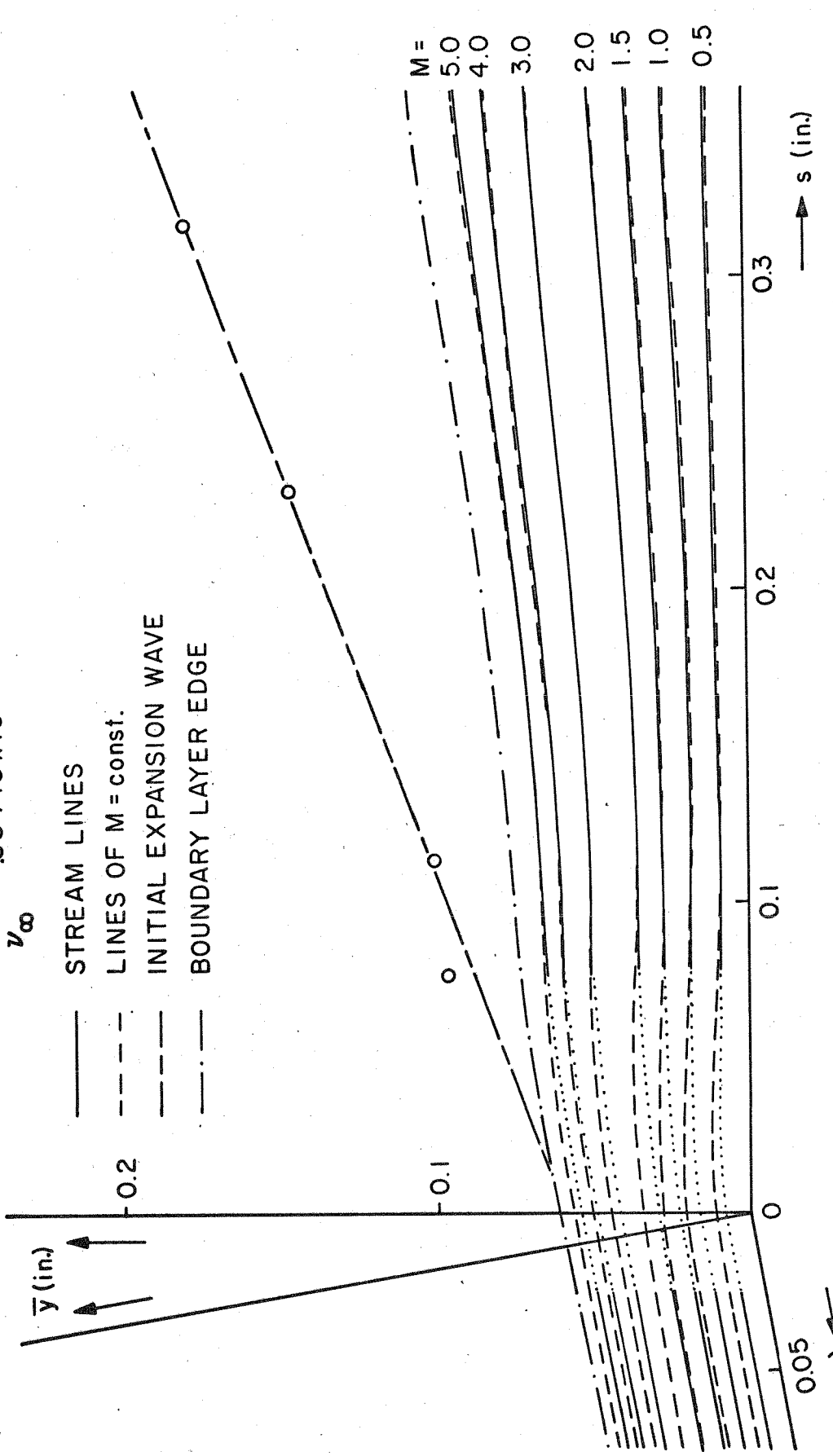

FIG. 19a. FLOW NEAR A SHARP CONE-CYLINDER JUNCTURE AT $M_\infty = 7.87$

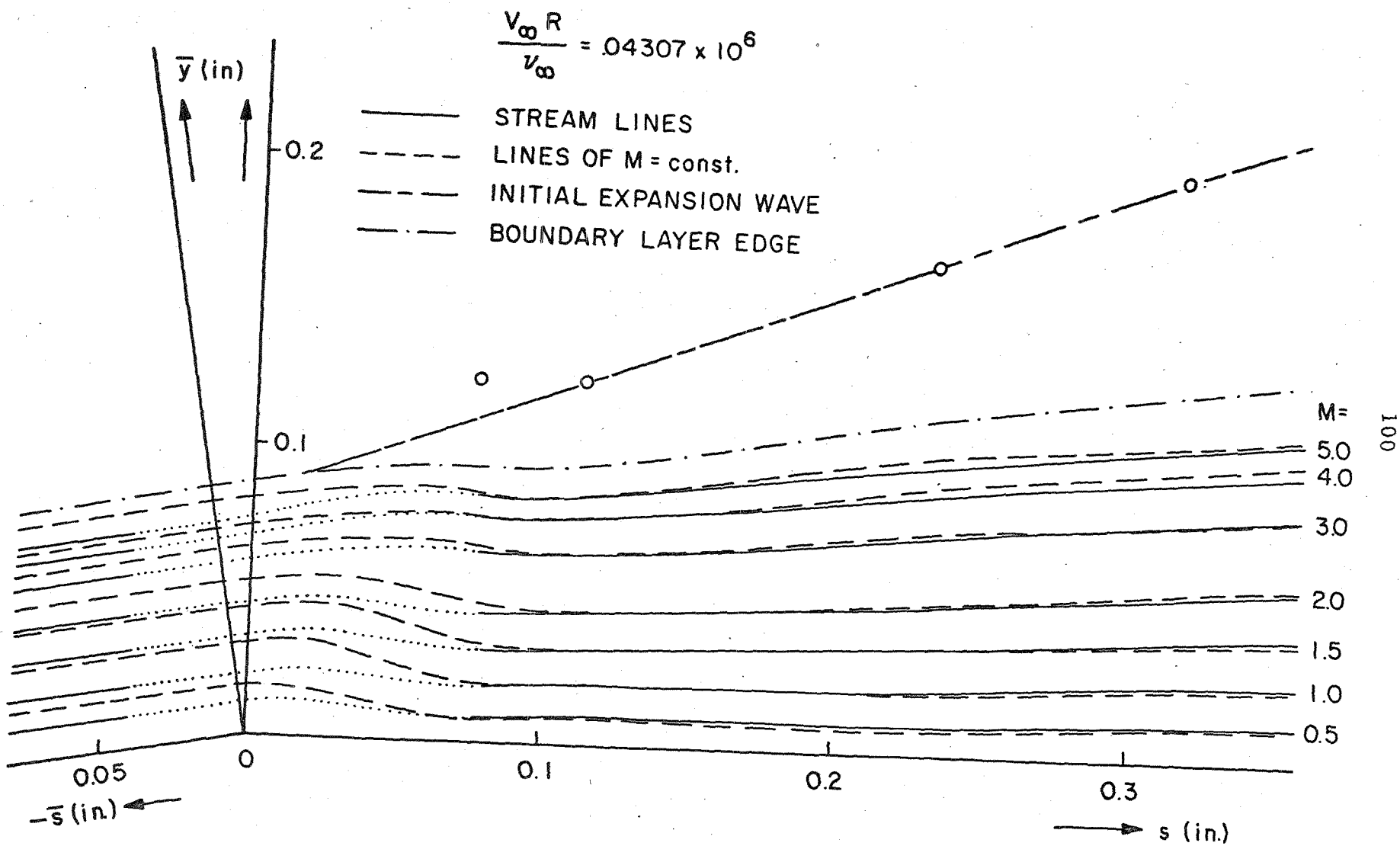

FIG. 19β. FLOW NEAR A SHARP CONE-CYLINDER JUNCTURE AT $M_\infty = 7.87$

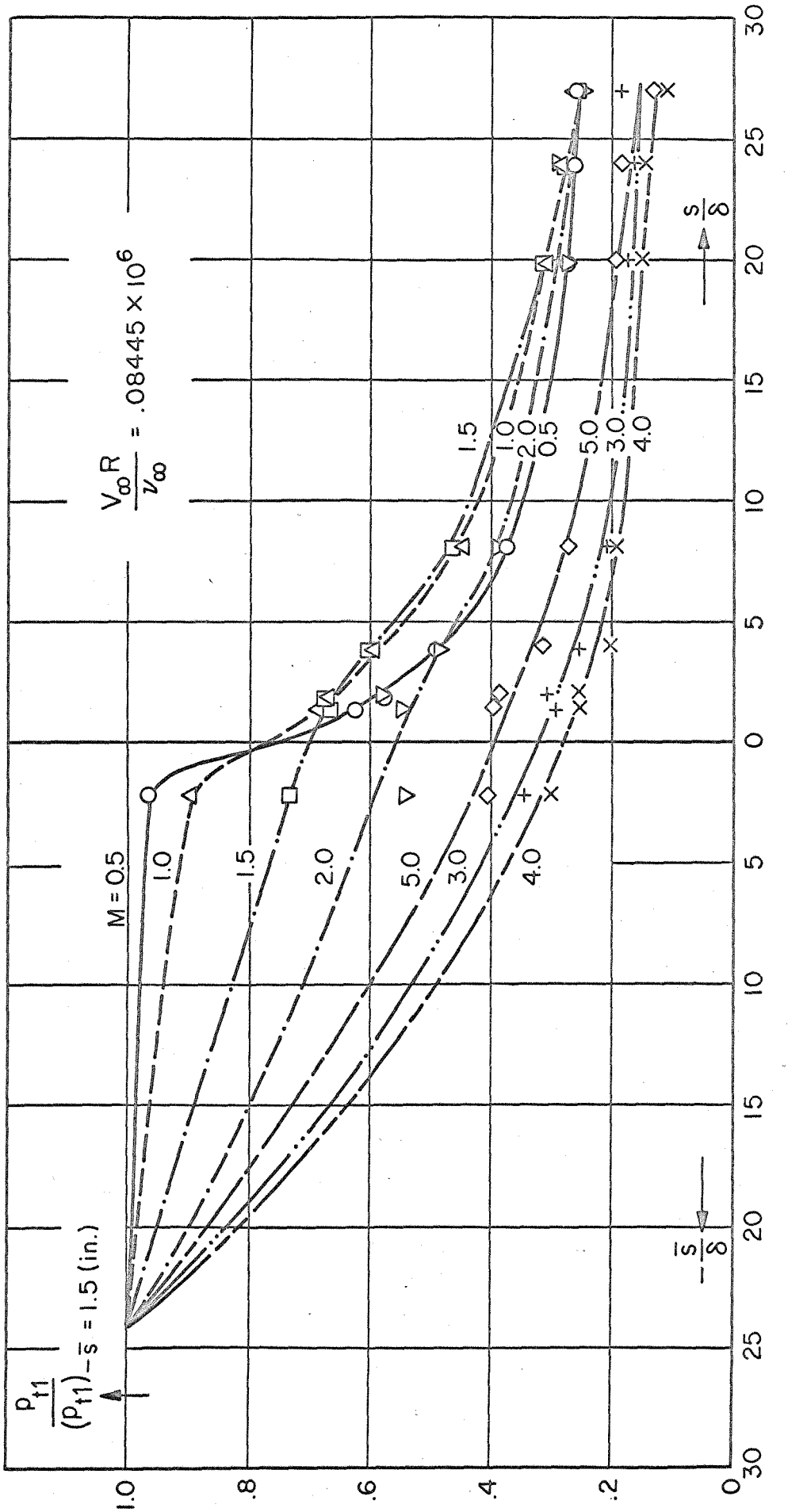

FIG. 20a. TOTAL PRESSURE VARIATION ALONG STREAM LINES IN VISCOUS LAYER NEAR CONE–CYLINDER JUNCTURE AT $M_\infty = 7.87$

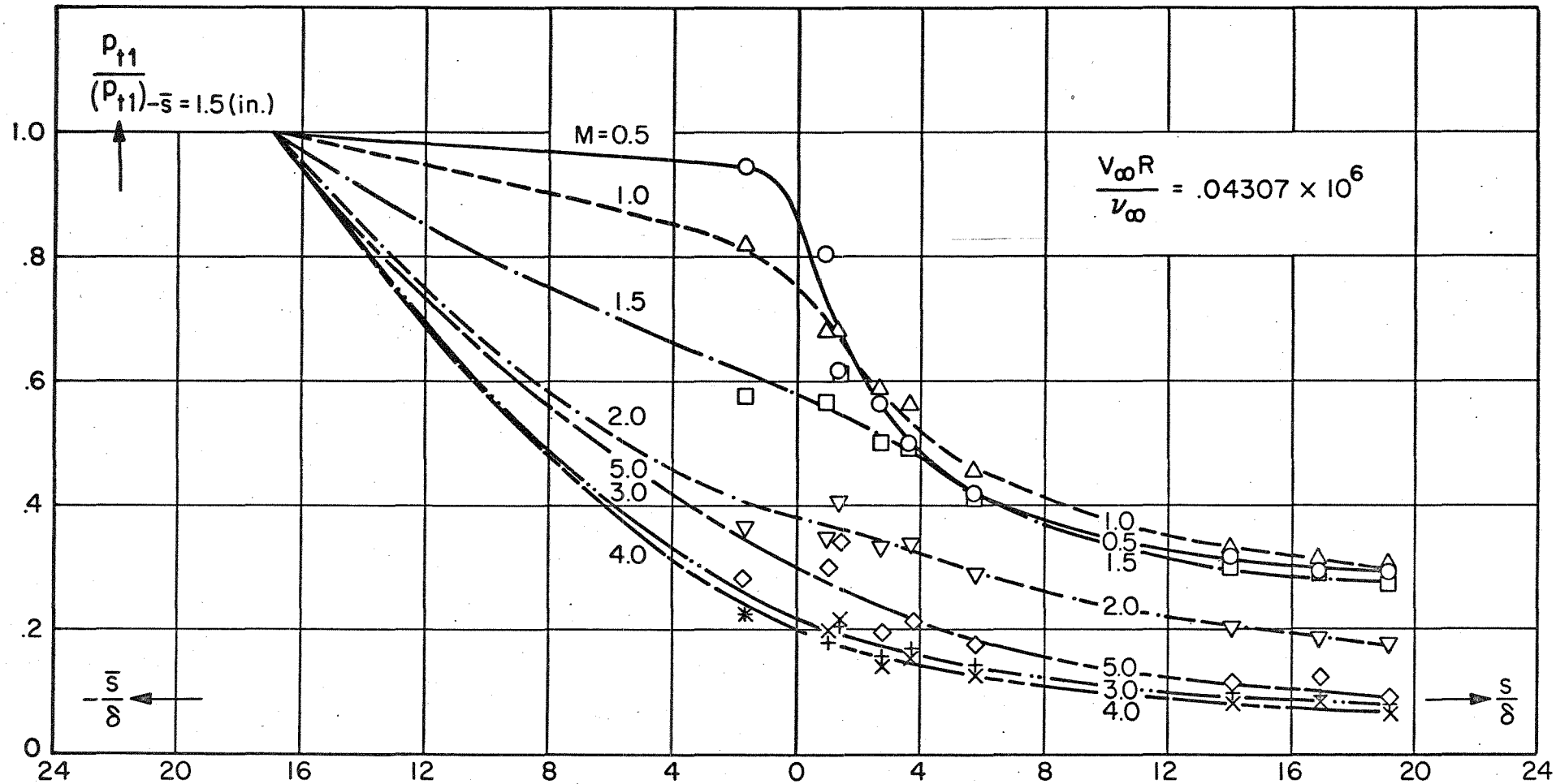

FIG. 20β. TOTAL PRESSURE VARIATION ALONG STREAM LINES IN VISCOUS LAYER NEAR CONE–CYLINDER JUNCTURE AT $M_\infty = 7.81$

Figure 21. Schlieren Photograph of Flow Around Sharp Cone-Cylinder Juncture for $Re_{R\infty} = .08445 \times 10^6$ and $M_\infty = 7.87$